ELSEVIER

Review

Effective interactions and the nuclear shell-model

D.J. Dean[a,b,*], T. Engeland[b,c], M. Hjorth-Jensen[b,c],
M.P. Kartamyshev[b,c], E. Osnes[b,c]

[a]*Physics Division, Oak Ridge National Laboratory, P.O. Box 2008, Oak Ridge, TN 37831-6373, USA*
[b]*Center of Mathematics for Applications, University of Oslo, Norway*
[c]*Department of Physics, University of Oslo, Norway*

Abstract

This review aims at a critical discussion of the interplay between effective interactions derived from various many-body approaches and spectroscopic data extracted from large scale shell-model studies. To achieve this, our many-body scheme starts with the free nucleon–nucleon (NN) interaction, typically modeled on various meson exchanges. The NN interaction is in turn renormalized in order to derive an effective medium dependent interaction. The latter is in turn used in shell-model calculations of selected nuclei. We also describe how to sum up the parquet class of diagrams and present initial uses of the effective interactions in coupled cluster many-body theory.
© 2004 Elsevier B.V. All rights reserved.

Contents

* Corresponding address: Physics Division, Oak Ridge National Laboratory, P.O. Box 2008 Oak Ridge, TN 37831-6373, USA.
E-mail address: dean@orph01.phy.ornl.gov (D.J. Dean).

1. Introduction

Traditional shell-model studies have recently received a renewed interest through large scale shell-model calculations in both no-core calculations [1–4] for light nuclei, the 1s0d shell [5], the 1p0f shell and the $2s1d0g_{7/2}$ shell with the inclusion of the $0h_{11/2}$ intruder state as well. It is now therefore fully possible to perform large-scale shell-model investigations and study the excitation spectra for systems with many basis states. With recent advances in Monte Carlo methods, see for example [6–12], one is also able to enlarge the dimensionality of the systems under study considerably, and important information on e.g., ground-state properties has thereby been obtained.

An important feature of such large-scale calculations is that it allows one to probe the underlying many-body physics in a hitherto unprecedented way. The crucial starting point in all such shell-model calculations is the derivation of an effective interaction, be it either an approach based on a microscopic theory starting from the free nucleon–nucleon (NN) interaction or a more phenomenologically determined interaction. In shell-model studies of e.g., the Sn isotopes, one may have up to 31 valence particles or holes interacting via e.g., an effective two-body interaction. The results of such calculations can therefore yield, when compared with the available body of experimental data, critical inputs to the underlying theory of the effective interaction.

Clearly, although the NN interaction is of short but finite range, with typical interparticle distances of the order of 1–2 fm, there are indications from both studies of few-body systems and infinite nuclear matter, that at least three-body interactions, both real and effective ones, may be of importance. Thus, with many valence nucleons present, such large-scale shell-model calculations may tell us how well e.g., an effective interaction

which only includes two-body terms does in reproducing properties such as excitation spectra and binding energies.

This work deals therefore with various ways of deriving the effective interaction or effective operator needed in shell-model calculations, starting from the free NN interaction. Normally, the problems of deriving such effective operators and interactions are solved in a limited space, the so-called model space, which is a subspace of the full Hilbert space. The effective operator and interaction theory is then introduced in order to systematically take into account contributions from the complement (the excluded space) of the chosen model space. Several formulations for such expansions of effective operators and interactions exist in the literature, following time-dependent or time-independent perturbation theory [13–18]. The so-called $\hat{Q}$-box method with the folded-diagram formulation of Kuo and co-workers [15, 16] has been extensively applied to systems in nuclear physics, especially for the derivation of effective interactions for the nuclear shell-model. This method is however limited by the fact that the $\hat{Q}$-box includes diagrams to a certain order in perturbation only. To go beyond third order in perturbation theory is very hard and there is no indication that the expansion converges. Thus, formulations like the coupled-cluster method or exponential ansatz [17, 19–22, 24–36], which is much favored in quantum chemistry, the summation of the parquet class of diagrams [37–44], although with few applications, and FHNC theory [41, 45, 46], offer the possibility of summing much larger classes of many-body terms.

Ab initio methods like variational and diffusional Monte Carlo approaches [8–12] and no-core shell-model calculations [1–4] for light nuclei have also been much favored in nuclear theory.

In this work we will focus on the above-mentioned $\hat{Q}$-box approach combined with the nuclear shell-model, the summation of the so-called parquet diagrams and coupled-cluster theory as three possible ways of studying the nuclear many-body problem. The $\hat{Q}$-box has been introduced in Rayleigh–Schrödinger perturbation theory as the definition of all non-folded diagrams to a given order in the expansion parameter, in nuclear physics the so-called G-matrix. The G-matrix renders the free NN interaction V, which is repulsive at small internucleon distances, tractable for a perturbative analysis through the summation of ladders diagrams to infinite order. Stated differently, the G-matrix, through the solution of the Bethe–Brueckner–Goldstone equation, accounts for the short-range correlations involving high-lying states. Folded diagrams are a class of diagrams which arise due to the removal of the dependence of the exact model-space energy in the Brillouin–Wigner perturbation expansion. Through the $\hat{Q}$-box formulation and its derivatives, this set of diagrams can easily be summed up.

In addition to the evaluation of folded diagrams and the inclusion of ladder diagrams to infinite order included in the G-matrix, there are other classes of diagrams which can be summed up. These take into account the effect of long-range correlations involving low-energy excitations. A frequently applied formalism is the Tamm–Dancoff (TDA) or the random-phase (RPA) approximations. In their traditional formulation one allows for the summation of all particle–hole excitations, both forward-going and backward-going insertions. This set of diagrams, as formulated by Kirson [47] and reviewed in [48], should account for correlations arising from collective particle–hole correlations. Another possibility is to include any number of particle–particle and hole–hole correlations

in the screening of particle–hole correlations. The inclusion of these correlations is conventionally labeled particle–particle (pp) RPA. It has been used both in nuclear matter studies [49–52] and in evaluations of ground-state properties of closed-shell nuclei [53–55]. Ellis, Mavromatis and Müther [54, 55] have extended the pp RPA to include the particle–hole (ph) RPA, though screening of two-particle–one-hole (2p1h) and two-hole–one-particle (2h1p) vertices was not included. The latter works can be viewed as a step towards the full summation of the parquet class of diagrams. The summation of the parquet diagrams entails a self-consistent summation of both particle–particle and hole–hole ladder diagrams and particle–hole diagrams. Practical solutions to this many-body scheme for finite nuclei will be discussed here.

The coupled-cluster method originated in nuclear physics over forty years ago when Coester and Kümmel proposed an exponential ansatz to describe correlations within a nucleus [19, 20]. This ansatz has been well justified for many-body problems using a formalism in which the cluster functions are constructed by cluster operators acting on a reference determinant [24]. Early applications to finite nuclei were described in [31]. From that time to this, a systematic development and implementation of this interesting many-body theory in nuclear physics applications has been only sporadic. The view from computational quantum chemistry is quite different. In fact, coupled-cluster methods applied to computational chemistry enjoy tremendous success [21, 22, 25–27] over a broad class of chemistry problems related to chemical and molecular structure and chemical reactions. The method is fully microscopic and is capable of systematic and hierarchical improvements. Indeed, when one expands the cluster operator in coupled-cluster theory to all *A* particles in the system, one exactly produces the fully-correlated many-body wave function of the system. The only input that the method requires is the nucleon–nucleon interaction. The method may also be extended to higher-order interactions such as the three-nucleon interaction. Second, the method is size extensive which means that only linked diagrams appear in the computation of the energy (the expectation value of the Hamiltonian) and amplitude equations. Third, coupled-cluster theory is also size consistent which means that the energy of two non-interacting fragments computed separately is the same as that computed for both fragments simultaneously. In chemistry, where the study of reactions is quite important, this is a crucial property not available in the interacting shell model (named configuration interaction in chemistry).

A fourth interesting point involves a comparison of coupled-cluster theory and many-body theory. The computed energy using the coupled-cluster formalism includes a very large class of many-body perturbation theory diagrams. In standard many-body perturbation theory, one typically sums all diagrams order by order. The coupled-cluster approach essentially iterates diagrams so that one may discuss it in terms of an infinite summation of particular classes of diagrams. The infinite resummation means that the coupled-cluster theory is non-perturbative. In fact, the coupled-cluster energy at the single and double excitation level contains contributions identical to those of second-order and third-order many-body perturbation theory, but lacks triple excitation contributions necessary to complete fourth-order many-body perturbation theory; see e.g., the review article of Bartlett [21]. Later in this review, we will compare second and third-order many-body perturbation theory to coupled-cluster calculations.

This work falls into eight sections. In the next section we present various definitions pertinent to the determination of effective interactions, with an emphasis on perturbative methods. The resummation of the ladder type of diagrams is then presented in Section 3. In that section we also discuss the summation of so-called folded diagrams which arise in the evaluation of valence space effective interactions. Further perturbative corrections are also discussed. Selected results for light nuclei in the 1s0d and 1p0f shells and for several medium-heavy nuclei in the mass region $A = 100$ to $A = 132$ are presented in the subsequent section.

The summation of the TDA and RPA class of diagrams and the so-called parquet diagrams is discussed in Section 5 whereas Section 6 is devoted to a discussion of the coupled-cluster method. Section 7 presents a critical discussion of three-body effects in nuclear structure.

We conclude in Section 8 with a discussion on the extension of the methods discussed in Sections 5 and 6 to weakly bound nuclei.

2. Many-body perturbation theory

In order to derive a microscopic approach to the effective interaction and/or operator within the framework of perturbation theory, we need to introduce various notations and definitions pertinent to the methods exposed. In this section we review how to calculate an effective operator within the framework of degenerate Rayleigh–Schrödinger (RS) perturbation theory [15, 17].

It is common practice in perturbation theory to reduce the infinitely many degrees of freedom of the Hilbert space to those represented by a physically motivated subspace, the model space. In such truncations of the Hilbert space, the notions of a projection operator P onto the model space and its complement Q are introduced. The projection operators defining the model and excluded spaces are defined by

$$P = \sum_{i=1}^{D} |\Phi_i\rangle\langle\Phi_i|, \tag{1}$$

and

$$Q = \sum_{i=D+1}^{\infty} |\Phi_i\rangle\langle\Phi_i|, \tag{2}$$

with D being the dimension of the model space, and $PQ = 0$, $P^2 = P$, $Q^2 = Q$ and $P + Q = I$. The wave functions $|\Phi_i\rangle$ are eigenfunctions of the unperturbed Hamiltonian $H_0 = T + U$, where T is the kinetic energy and U an appropriately chosen one-body potential, that of the harmonic oscillator (h.o.) in most calculations. The full Hamiltonian is then rewritten as $H = H_0 + H_1$ with $H_1 = V - U$, V being e.g. the NN interaction. The eigenvalues and eigenfunctions of the full Hamiltonian are denoted by $|\Psi_\alpha\rangle$ and E_α,

$$H|\Psi_\alpha\rangle = E_\alpha|\Psi_\alpha\rangle. \tag{3}$$

Rather than solving the full Schrödinger equation above, we define an effective Hamiltonian acting within the model space such that

$$P H_{\text{eff}} P | \Psi_\alpha \rangle = E_\alpha P | \Psi_\alpha \rangle = E_\alpha | \Phi_\alpha \rangle \tag{4}$$

where $| \Phi_\alpha \rangle = P | \Psi_\alpha \rangle$ is the projection of the full wave function onto the model space, the model space wave function. In RS perturbation theory, the effective interaction H_{eff} can be written out order by order in the interaction H_1 as

$$P H_{\text{eff}} P = P H_1 P + P H_1 \frac{Q}{e} H_1 P + P H_1 \frac{Q}{e} H_1 \frac{Q}{e} H_1 P + \cdots, \tag{5}$$

where terms of third and higher order also include the aforementioned folded diagrams. Further, $e = \omega - H_0$, where ω is the so-called starting energy, defined as the unperturbed energy of the interacting particles. Similarly, the exact wave function $| \Psi_\alpha \rangle$ can now be written in terms of the model space wave function as

$$| \Psi_\alpha \rangle = | \Phi_\alpha \rangle + \frac{Q}{e} H_1 | \Phi_\alpha \rangle + \frac{Q}{e} H_1 \frac{Q}{e} H_1 | \Phi_\alpha \rangle + \cdots. \tag{6}$$

The wave operator is often expressed as

$$\Omega = 1 + \chi, \tag{7}$$

where χ is known as the correlation operator. The correlation operator generates the component of the wave function in the Q-space and must therefore contain at least one perturbation. Observing that $P \Omega P = P$, we see that the correlation operator χ has the properties

$$P \chi P = 0, \qquad Q \Omega P = Q \chi P = \chi P. \tag{8}$$

Since $| \Psi_i \rangle = \Omega | \Psi_i^M \rangle$ determines the wave operator only when it operates to the right on the model space, i.e., only the ΩP part is defined, the term ΩQ never appears in the theory, and we could therefore add the conditions $Q \chi Q = 0$ and $P \chi Q = 0$ to Eq. (8). This leads to the following choice for χ

$$\chi = Q \chi P. \tag{9}$$

This has been the traditional choice in perturbation theory [13, 17].

The wave operator Ω can then be ordered in terms of the number of interactions with the perturbation H_1

$$\Omega = 1 + \Omega^{(1)} + \Omega^{(2)} + \cdots, \tag{10}$$

where $\Omega^{(n)}$ means that we have n H_1 terms. Explicitly, the above equation reads

$$\begin{aligned}
\Omega | \Phi_i \rangle = {} & | \Phi_i \rangle + \sum_\alpha \frac{| \alpha \rangle \langle \alpha | V | \Phi_i \rangle}{\varepsilon_i - \varepsilon_\alpha} + \sum_{\alpha\beta} \frac{| \alpha \rangle \langle \alpha | V | \beta \rangle \langle \beta | V | \Phi_i \rangle}{(\varepsilon_i - \varepsilon_\alpha)(\varepsilon_i - \varepsilon_\beta)} \\
& - \sum_{\alpha j} \frac{| \alpha \rangle \langle \alpha | V | \Phi_j \rangle \langle \Phi_j | V | \Phi_i \rangle}{(\varepsilon_i - \varepsilon_\alpha)(\varepsilon_i - \varepsilon_j)} + \cdots,
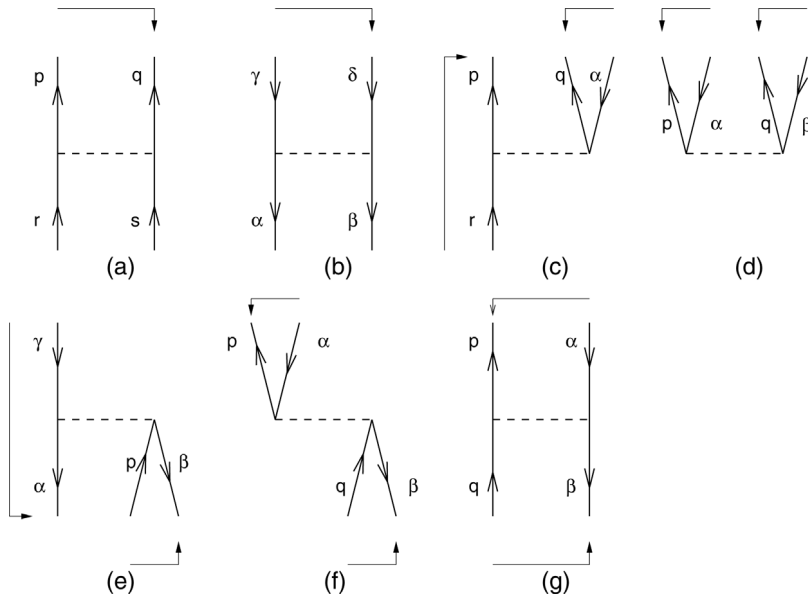\end{aligned} \tag{11}$$

Fig. 1. The various vertices to first order in the interaction V which contribute to the wave operator $\Omega = 1 + \chi$. Hartree–Fock terms are not included. Possible Hermitian conjugate diagrams are not shown. Indicated are also possible angular momentum coupling orders.

where ε are the unperturbed energies of the P-space and Q-space states defined by H_0. The Greek letters refer to Q-space states, whereas a Latin letter refers to model-space states. The second term in the above equation corresponds to $\Omega^{(1)}$ while the third and fourth define $\Omega^{(2)}$. Note that the fourth term diverges in case we have a degenerate or nearly degenerate model space. It is actually divergencies like these which are to be removed by the folded diagram procedure to be discussed in the next section. Terms like these arise due to the introduction of an energy independent perturbative expansion. Conventionally, the various contributions to the perturbative expansion are represented by Feynman–Goldstone diagrams. In Fig. 1 we display the topologically distinct contributions to first order in the interaction V to the wave operator Eq. (11). These diagrams all define the correlation operator χ to first order in V. Diagrams with Hartree–Fock contributions and single-particle potential terms are not included. The possible renormalizations of these diagrams will be discussed in the next four sections.

The linked-diagram theorem [17, 41] can be used to obtain a perturbative expansion for the energy in terms of the perturbation V or $V = H - H_0$ where H_0 represents the unperturbed part of the Hamiltonian. The expression for the energy E reads

$$E = \sum_{k=0}^{\infty} \langle \Psi_0 | H [(\omega - H_0)^{-1} H]^k | \Psi_0 \rangle_L, \tag{12}$$

where Ψ_0 is the uncorrelated Slater determinant for the ground state, ω is the corresponding unperturbed energy and the subscript L stands for linked diagrams only. In Fig. 2 we
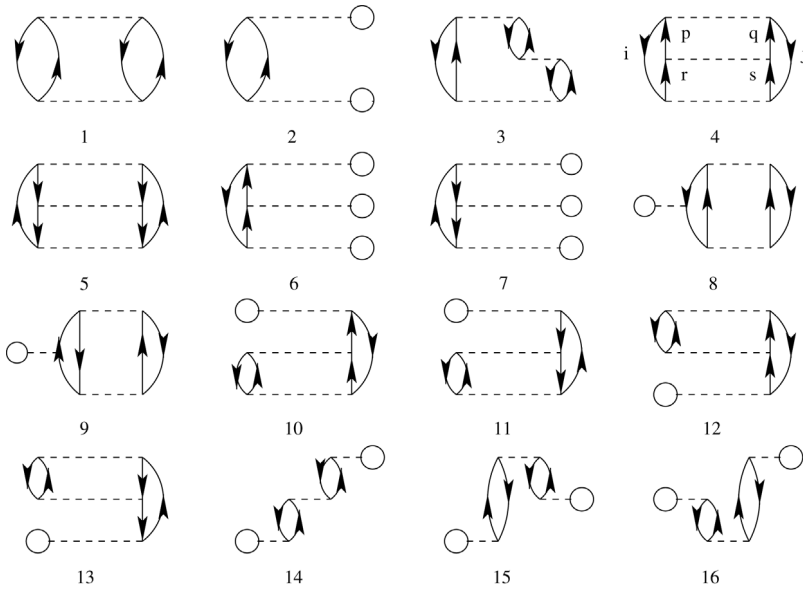
Fig. 2. Antisymmetrized Goldstone diagrams through third order in perturbation theory included in the evaluation of the binding energy. The dashed lines represent the interaction. Particle and hole states are represented by upward and downward arrows, respectively. The first order diagram is omitted. All closed circles stand for a summation over hole states.

show all antisymmetrized Goldstone diagrams for closed-shell systems through third order in perturbation theory (we omit the first-order diagram). All closed circles stand for a summation over hole states. The expression for e.g., diagram (4) ΔE_4 in Fig. 2 reads in an angular momentum coupled basis (with J being the total two-body angular momentum)

$$\Delta E_4 = \frac{1}{8} \sum_{\substack{ij \leq F \\ pqrs > F \\ J}} (2J+1)\langle (ij)J|V|(pq)J\rangle \frac{1}{\varepsilon_i + \varepsilon_j - \varepsilon_p - \varepsilon_q}$$

$$\times \langle (pq)J|V|(rs)J\rangle \frac{1}{\varepsilon_i + \varepsilon_j - \varepsilon_r - \varepsilon_s} \langle (rs)J|V|(ij)J\rangle. \tag{13}$$

The symbol F represents the last hole, or Fermi surface. In the next section we will replace the bare interaction with the so-called G-matrix.

We end this section with the equations for the diagrams in Fig. 1 representing χ to first order in V. Moreover, in order to introduce the various channels needed to sum the parquet class of diagrams, we will find it convenient here to classify these channels in terms of angular momentum recouplings. Later on, we will also introduce the pertinent definitions of energy and momentum variables in the various channels. The nomenclature we will follow in our labeling is that of Blaizot and Ripka, see [41, Chapter 15]. All matrix elements in the definitions below are antisymmetrized and unnormalized. The first channel is the [12] channel, or the s-channel in field theory, and its angular momentum coupling order is depicted in Fig. 3. In this figure we do not distinguish between particles and holes,
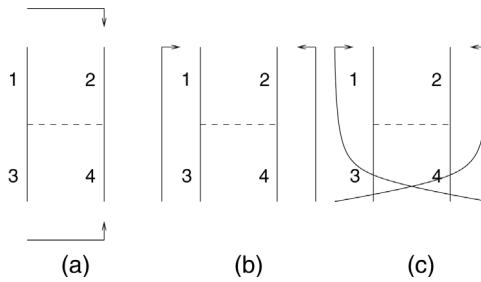
Fig. 3. Coupling order for the [12] (a), [13] (b) and [14] (c) channels.

all single-particle labels 1, 2, 3, 4 can represent either a hole or particle single-particle state. It is the coupling order which is of interest here. The matrix element $V^{[12]}$ in the [12] channel is then

$$V^{[12]}_{1234J} = \langle (12)J|V|(34)J \rangle, \tag{14}$$

meaning that the single-particle state 1(3) couples to the state 2(4) to yield a total angular momentum J. This channel is commonly denoted as the particle–particle (pp) or particle–particle–hole–hole (pphh) channel, meaning that when we sum classes of diagrams to infinite order in this channel, the only intermediate states which are allowed are those of a pphh character, coupled to a final J in the above order. In the next section we will explicitly discuss ways to evaluate the equations for the [12] channel. This coupling order is also the standard way of representing effective interactions for shell-model calculations. If we now specialize to particles and holes (these matrix elements were shown in Fig. 1) we obtain for the case with particle states only,[1] diagram (a),

$$V_{2p} = V^{[12]}_{pqrsJ} = \langle (pq)J|V|(rs)J \rangle. \tag{15}$$

The corresponding one for holes only, diagram (b), is

$$V_{2h} = V^{[12]}_{\alpha\beta\gamma\delta J} = \langle (\alpha\beta)J|V|(\gamma\delta)J \rangle. \tag{16}$$

Thus, in the forthcoming discussion, we will always employ as our basic notation for a matrix element that of the [12] channel, meaning that matrix elements of the other two channels can always be rewritten in terms of those in the [12] channel We see this immediately by looking at the expression for the matrix element in the [13] channel, the t-channel in field theory, see Fig. 3(b). Here the single-particle state 3(4) couples to the single-particle state 1(2).[2] Through simple angular momentum algebra we have

$$V^{[13]}_{1234J} = \sum_{J'}(-)^{j_1+j_4+J+J'} \hat{j}'^2 \begin{Bmatrix} j_3 & j_1 & J \\ j_2 & j_4 & J' \end{Bmatrix} V^{[12]}_{1234J'}, \tag{17}$$

---

[1] Note that we only include angular momentum factors, other factors coming from the diagram rules [58], like number of hole lines, number of closed loops, energy denominators etc. are omitted here.

[2] In a Goldstone–Feynman diagram in an angular momentum representation, the coupling direction will always be from incoming single-particle states to outgoing single-particle states.

where the symbol with curly brackets represents a $6j$-symbol and $\hat{J}' = \sqrt{2J' + 1}$. In a similar way we can also express the matrix element in the [14] channel, the u-channel in field theory, through

$$V^{[14]}_{1234J} = \sum_{J'}(-)^{j_1+j_4+J+2j_3}\hat{J}'^2 \begin{Bmatrix} j_4 & j_1 & J \\ j_2 & j_3 & J' \end{Bmatrix} V^{[12]}_{1234J}. \tag{18}$$

It is also possible to have the inverse relations or to express e.g., the [14] channel through the [13] channel as

$$V^{[14]}_{1234J} = \sum_{J'}(-)^{2j_1+2j_2+2j_3}\hat{J}'^2 \begin{Bmatrix} j_4 & j_1 & J \\ j_3 & j_2 & J' \end{Bmatrix} V^{[13]}_{1234J}. \tag{19}$$

The matrix elements defined in Eqs. (14)–(19) and the inverse relations are the starting points for various resummation of diagrams. In the next section we will detail ways of solving equations in the [12] channel, whereas various approximations for the [13] channel and [14] channel such as the TDA and RPA and vertex and propagator renormalization schemes will be discussed in Section 5. Finally, how to merge self-consistently all three channels will also be discussed in Section 5.

We end this section by giving the expressions in an angular momentum basis for the remaining diagrams of Fig. 1. The coupling order is indicated in the same figure.

The 2p1h vertex V_{2p1h}, diagram (c) in Fig. 1, is coupled following the prescription of the [13] channel and reads

$$V_{\text{2p1h}} = V^{[13]}_{pqr\alpha J} = \sum_{J'}(-)^{j_\alpha+j_p+J+J'}\hat{J}'^2 \begin{Bmatrix} j_r & j_p & J \\ j_q & j_\alpha & J' \end{Bmatrix} V^{[12]}_{pqr\alpha J'}. \tag{20}$$

The 2p2h ground-state correlation V_{2p2h}, diagram (d), which will enter in the RPA summation discussed in Section 5 is given by, the coupling order is that of the [13] channel,

$$V_{\text{2p2h}} = V^{[13]}_{pq\alpha\beta J} = \sum_{J'}(-)^{j_\beta+j_p+J+J'}\hat{J}'^2 \begin{Bmatrix} j_\alpha & j_p & J \\ j_q & j_\beta & J' \end{Bmatrix} V^{[12]}_{pq\alpha\beta J'}. \tag{21}$$

The 2h1p vertex V_{2h1p}, diagram (e), still in the representation of the [13] channel, is defined as

$$V_{\text{2h1p}} = V^{[13]}_{\alpha\beta\gamma pJ} = \sum_{J'}(-)^{j_\alpha+j_p+J+J'}\hat{J}'^2 \begin{Bmatrix} j_\gamma & j_\alpha & J \\ j_\beta & j_p & J' \end{Bmatrix} V^{[12]}_{\alpha\beta\gamma pJ'}. \tag{22}$$

Note well that the vertices of Eqs. (20)–(22) and their respective Hermitian conjugates can all be expressed in the [14] channel or [12] channel as well. However, it is important to note that the expressions in the various channels are different, and when solving the equations for the various channels, the renormalizations will be different. As an example, consider the two particle–hole vertices V_{ph} of Fig. 1, i.e., diagrams (f) and (g). Diagram (g) is just the exchange diagram of (f) when seen in the [12] channel. However, if (f) is coupled as in the [13] channel, recoupling this diagram to the [14] channel will not give two particle–hole two-body states coupled to a final J but rather a particle–particle two-body state and a hole–hole two-body state. But why bother at all about such petty details?

The problem arises when we are to sum diagrams in the [13] channel and [14] channel. In the [12] channel we allow only particle–particle and hole–hole intermediate states, whereas in the [13] channel and [14] channel we allow only particle–hole intermediate states, else we may risk to double-count various contributions. If we therefore recouple diagram (f) to the [14] representation, this contribution does not yield an intermediate particle–hole state in the [14] channel. Thus, diagram (f), whose expression is

$$V_{\text{ph}} = V^{[13]}_{p\beta\alpha qJ} = \sum_{J'} (-)^{j_p+j_q+J+J'} \hat{j}'^2 \begin{Bmatrix} j_\alpha & j_p & J \\ j_\beta & j_q & J' \end{Bmatrix} V^{[12]}_{p\beta\alpha qJ'}, \tag{23}$$

yields a particle–hole contribution only in the [13] channel, whereas the exchange diagram (g), which reads

$$V_{\text{ph}} = V^{[14]}_{p\beta q\alpha J} = \sum_{J'} (-)^{2j_q+j_\alpha+j_p+J} \hat{j}'^2 \begin{Bmatrix} j_\alpha & j_p & J \\ j_\beta & j_q & J' \end{Bmatrix} V^{[12]}_{p\beta q\alpha J'}, \tag{24}$$

results in the corresponding particle–hole contribution in the [14] channel. In electron gas theory, the latter expression is often identified as the starting point for the self-screening of the exchange term. In the discussion of the TDA series in Section 4 we will give the expressions for the screening corrections based on Eqs. (23) and (24).

An important aspect to notice in connection with the latter equations and the discussions in Section 5 is that

$$V^{[14]}_{p\beta q\alpha J} = -V^{[13]}_{p\beta\alpha qJ}, \tag{25}$$

i.e., just the exchange diagram, as it should be. This is however important to keep in mind, since we later on will sum explicitly sets of diagrams in the [13] channel and the [14] channel, implying thereby that we will obtain screening and vertex corrections for both direct and exchange diagrams.

3. Diagrams in the [12] channel

In order to write down the equation for the renormalized interaction $\Gamma^{[12]}$ in the [12] channel we need first to present some further definitions. We will also assume that the reader has some familiarity with the theory of Green's function. In our presentation below we will borrow from the monograph of Blaizot and Ripka [41], see also the recent review articles of Dickhoff and Barbieri [56] and Müther and Polls [57]. The vertex $\Gamma^{[12]}$ is in lowest order identical with the interaction $V^{[12]}$ and obeys also the same symmetry relations as V, i.e.,

$$\Gamma^{[12]}_{1234J} = \Gamma^{[12]}_{2143J} = -\Gamma^{[12]}_{2134J} = \Gamma^{[12]}_{1243J}. \tag{26}$$

We also need to define energy variables. Since we are going to replace the interaction V with the G-matrix, or certain approximations to it, defined below in all of our practical calculations, the momentum variables are already accounted for in G. The basis will be that of harmonic oscillator wave functions, and the labels 1234 will hence refer to oscillator quantum numbers, which in turn can be related to the momentum variables. The labels 1234, in addition to representing single-particle quantum numbers, define also the energy
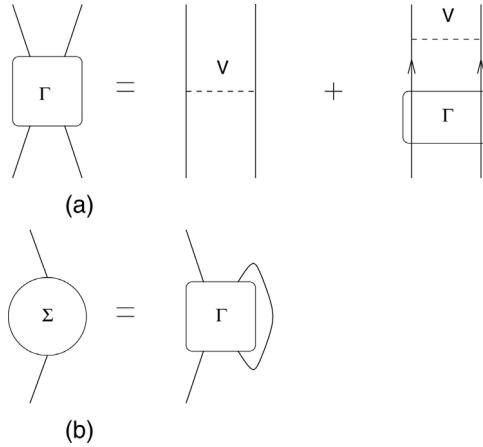
Fig. 4. (a) represents the two-body vertex Γ function while (b) represents the self-energy Σ.

of the single-particle states. With a harmonic oscillator basis, the starting point for the single-particle energies $\varepsilon_{1,2,3,4}$ are the unperturbed oscillator energies. When iterating the equations for $\Gamma^{[12]}$, self-consistent single-particle energies can be introduced. The total energy in the [12] channel s is

$$s = \varepsilon_1 + \varepsilon_2 = \varepsilon_3 + \varepsilon_4. \tag{27}$$

The equation for the vertex $\Gamma^{[12]}$ is, in a compact matrix notation, given by [41]

$$\Gamma^{[12]} = V^{[12]} + V^{[12]}(gg)\Gamma^{[12]}, \tag{28}$$

where g is the one-body Green's function representing the intermediate states. The diagrammatic expression for this equation is given in Fig. 4. The expression of Eq. (28) is known as the Feynman–Galitskii equation. This equation is normally solved iteratively. In the first iteration the irreducible vertex $V^{[12]}$ is then often chosen as the bare NN interaction. This interaction is then typically assumed to be energy independent and we can drop the s dependence of $V^{[12]}$. Moreover, the single-particle propagators are chosen as the unperturbed ones. The first iteration of Eq. (28) can then be rewritten as

$$\Gamma^{[12]}_{1234J}(s) = V^{[12]}_{1234J} + \tfrac{1}{2} \sum_{56} V^{[12]}_{1256J} \hat{\mathcal{G}}^{[12]} \Gamma^{[12]}_{5634J}(s). \tag{29}$$

We have defined the unperturbed particle–particle and hole–hole propagators

$$\hat{\mathcal{G}}^{[12]} = \frac{Q^{[12]}_{\text{pp}}}{s - \varepsilon_5 - \varepsilon_6 + \imath\eta} - \frac{Q^{[12]}_{\text{hh}}}{s - \varepsilon_5 - \varepsilon_6 - \imath\eta}, \tag{30}$$

which results from the integration over the energy variable in the product of the two single-particle propagators in Eq. (28). In our discussions we will not deal with dressed propagators, neither for the one-particle nor the two-particle propagators. For this and related topics such as the spreading of single-particle strength we refer to the work of Dickhoff and Barbieri [56]. In our discussion of the coupled-cluster method however,

such features can be extracted at the end of the calculations through various expectation values. These expectation values will however depend on the actual size of the model space used. In our case this applies to the number of harmonic oscillator shells.

The factor $1/2$ in Eq. (29) follows from one of the standard Goldstone–Feynman diagram rules [58], which state that a factor $1/2$ should be associated with each pair of lines which starts at the same interaction vertex and ends at the same interaction vertex. This rule follows from the fact that we sum freely over the intermediate single-particle states 56. The reader should note that the intermediate states 56 can represent a two-particle state or a two-hole state. In Eq. (30) we have assumed unperturbed single-particle energies. In our iterations we will approximate the single-particle energies with their real part only. Thus, the two-particle propagator $\hat{\mathcal{G}}^{[12]}$ with renormalized single-particle energies has the same form as the unperturbed one. The operators $Q_{\mathrm{pp}}^{[12]}$ and $Q_{\mathrm{hh}}^{[12]}$ ensure that the intermediate states are of two-particle or two-hole character. In order to obtain a self-consistent scheme, Eq. (29) has also to be accompanied with the equation for the single-particle propagators g given by Dyson's equation

$$g = g_0 + g_0 \Sigma g, \tag{31}$$

with g_0 being the unperturbed single-particle propagator and Σ the self-energy. We will however defer a discussion of these quantities to Section 5. Here it will suffice to state that the self-energy is related to the vertex $\Gamma^{[12]}$ as

$$\Sigma \sim g\Gamma. \tag{32}$$

The similarity sign is meant to indicate that, although being formally correct, great care has to be exercised in order not to double-count contributions to the self-energy [40]. The set of equations for the vertex function and the self-energy is shown pictorially in Fig. 4. Assume now that we have performed the first iteration. The question which now arises is whether the obtained vertex $\Gamma^{[12]}$ from the solution of Eq. (29) should replace the bare vertex $V^{[12]}$ in the next iteration. Before answering this question, let us give some examples of diagrams which can be generated from the first iteration. These contributions are given by e.g., diagrams (a)–(d) in Fig. 5. Diagrams (a) and (b) are examples of contributions to second order in perturbation theory, while diagrams (c) and (d) are higher-order terms. Diagrams (e) and (f) are higher-order core-polarization terms, which can e.g., be generated through the solution of the equations for the [13] and [14] channels discussed in the next section. If we were to include diagrams (a)–(d) in the definition of the bare vertex in our next iteration, we are prone to double-count, since such contributions are generated once again. Diagrams which contain the particle–hole intermediate state are however not generated by the solution of Eq. (29). We need therefore to define the vertex $V^{[12]}$ used in every iteration to be the sum of diagrams which are irreducible in the [12] channel. By irreducible we will mean all diagrams which cannot be reduced to a piece containing the particle states 12 entering or leaving the same interaction vertex and another part containing the states 34 at the same interaction vertex by cutting two internal lines. Clearly, if we cut diagrams (a) and (b) we are just left with two bare interaction vertices. Similarly, cutting two lines of an intermediate state in diagrams (c) and (d) leaves us with two second-order terms of the type (a) and (b) and one bare interaction. Diagrams (e) and (f) are however examples of
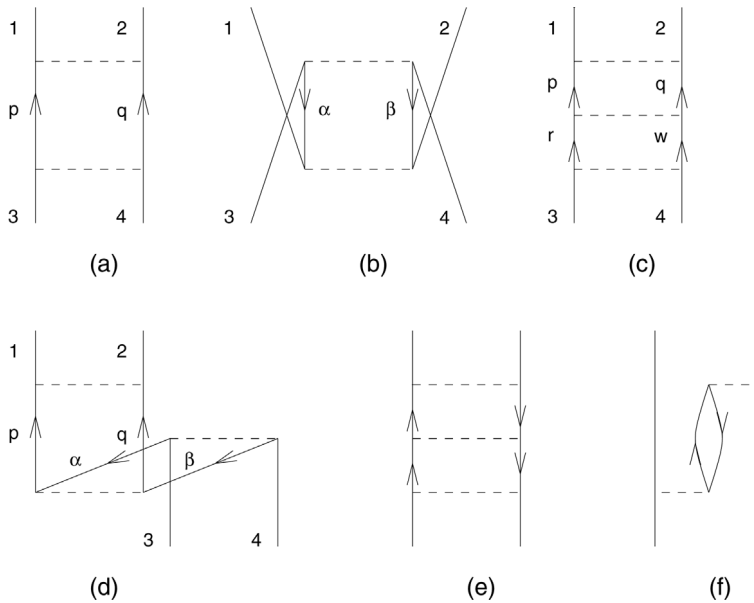
Fig. 5. Diagrams (a)–(d) give examples of diagrams which are summed up by the use of Eq. (28). Diagrams (e) and (f) are examples of core-polarization terms which are not generated by the [12] channel.

diagrams which are irreducible in the [12] channel. Diagram (e) is irreducible in the [13] channel, but not in the [14] channel. Similarly, diagram (g) is reducible in the [13] channel and irreducible in the [14] channel. This means that, unless we solve equations similar to Eq. (29) in the [13] channel and [14] channel as well, changes from further iterations of Eq. (29) will only come from the single-particle terms defined by Dyson's equation in Eq. (31).

In the remaining part of this section, we will try to delineate ways of solving the above equations, and discuss possible approximations, their merits and faults. First of all, we will reduce the propagator of Eq. (30) to only include particle–particle intermediate states. This will lead us to the familiar G-matrix in nuclear many-body theory. Based on the G-matrix, we will construct effective interactions through perturbative summations. Applications of such effective interactions to selected nuclei will then be discussed. Thereafter, we will try to account for hole–hole contributions and self-consistent determinations of the single-particle energies through the solution of Dyson's equation.

3.1. The G-matrix

In nuclear structure and nuclear matter calculations one has to face the problem that any realistic NN interaction V exhibits a strong short-range repulsion, which in turn makes a perturbative treatment of the nuclear many-body problem prohibitive. If the interaction has a so-called hard core, the matrix elements of such an interaction $\langle \psi | V | \psi \rangle$ evaluated for an uncorrelated two-body wave function $\psi(r)$ diverge, since the uncorrelated wave function is different from zero also for relative distances r smaller than the hard-core radius.

Similarly, even if one uses interactions with softer cores, the matrix elements of the interaction become very large at short distances. The above problem was however overcome by introducing the reaction matrix $G^{[12]}$ (displayed by the summation of ladder type of diagrams in Fig. 5 with particle–particle intermediate states only), accounting thereby for short-range two-nucleon correlations. The $G^{[12]}$-matrix represents just a subset to the solution of the equations for the interaction $\Gamma^{[12]}$ in the [12] channel, we have clearly neglected the possibility of having intermediate states which are of the hole–hole type. The matrix elements of the interaction $V^{[12]}$ then become

$$\langle \psi | G^{[12]} | \psi \rangle = \langle \psi | V^{[12]} | \Psi \rangle \tag{33}$$

where Ψ is now the correlated wave function containing selected correlation from the excluded space. By accounting for these correlations in the two-body wave function Ψ, the matrix elements of the interaction become finite, even for a hard-core interaction V. Moreover, as will be discussed below, compared with the uncorrelated wave function, the correlated wave function enhances the matrix elements of V at distances for which the interaction is attractive. The type of correlations which typically are included in the evaluation of the $G^{[12]}$-matrix are those of the two-particle type. If we label the operator Q in this case by $Q_{pp}^{[12]}$, we can write the integral equation for the G-matrix as

$$G^{[12]}(s) = V^{[12]} + V^{[12]} \frac{Q_{pp}^{[12]}}{s - H_0 + \iota\eta} G^{[12]}(s), \tag{34}$$

implicitly assuming that $\lim \eta \to \infty$. The variable s represents normally the unperturbed energy of the incoming two-particle state. We will suppress $\iota\eta$ in the following equations. Moreover, since one is often interested only in the $G^{[12]}$-matrix for negative starting energies, the $G^{[12]}$-matrix commonly used in studies of effective interactions has no divergencies. Note also, that compared with Eq. (29), we express the G-matrix in terms of operators. The explicit form, with e.g., the sum over intermediate states is implicitly included here. We can also write

$$G^{[12]}(s) = V^{[12]} + V^{[12]} Q_{pp}^{[12]} \frac{1}{s - Q_{pp}^{[12]} H_0 Q_{pp}^{[12]}} Q_{pp}^{[12]} G^{[12]}(s). \tag{35}$$

The former equation applies if the Pauli operator $Q_{pp}^{[12]}$ commutes with the unperturbed Hamiltonian H_0, whereas the latter is needed if $[H_0, Q_{pp}^{[12]}] \neq 0$. Similarly, the correlated wave function Ψ is given as

$$|\Psi\rangle = |\psi\rangle + \frac{Q_{pp}^{[12]}}{s - H_0} G^{[12]} |\psi\rangle, \tag{36}$$

or

$$|\Psi\rangle = |\psi\rangle + Q_{pp}^{[12]} \frac{1}{s - Q_{pp}^{[12]} H_0 Q_{pp}^{[12]}} Q_{pp}^{[12]} G^{[12]} |\psi\rangle. \tag{37}$$

In order to evaluate the $G^{[12]}$-matrix for finite nuclei, we define first a useful identity following Bethe et al. [59]. Suppose we have two different G-matrices,[3] defined by

$$G_1 = V_1 + V_1 \frac{Q_1}{e_1} G_1, \tag{38}$$

and

$$G_2 = V_2 + V_2 \frac{Q_2}{e_2} G_2, \tag{39}$$

where Q_1/e_1 and Q_2/e_2 are the propagators of either Eq. (34) or (35). G_1 and G_2 are two different G-matrices having two different interactions and/or different propagators. We aim at an identity which will enable us to calculate G_1 in terms of G_2, or vice versa. Defining the wave operators

$$\Omega_1 = 1 + \frac{Q_1}{e_1} G_1, \tag{40}$$

and

$$\Omega_2 = 1 + \frac{Q_2}{e_2} G_2, \tag{41}$$

we can rewrite the above G-matrices as

$$G_1 = V_1 \Omega_1, \tag{42}$$

and

$$G_2 = V_2 \Omega_2. \tag{43}$$

Using these relations, we rewrite G_1 as

$$\begin{aligned} G_1 &= G_1 - G_2^\dagger \left(\Omega_1 - 1 - \frac{Q_1}{e_1} G_1 \right) + \left(\Omega_2^\dagger - 1 - G_2^\dagger \frac{Q_2}{e_2} \right) G_1 \\ &= G_2^\dagger + G_2^\dagger \left(\frac{Q_1}{e_1} - \frac{Q_2}{e_2} \right) G_1 + \Omega_2^\dagger G_1 - G_2^\dagger \Omega_1, \end{aligned} \tag{44}$$

and using Eqs. (42) and (43) we obtain the identity

$$G_1 = G_2^\dagger + G_2^\dagger \left(\frac{Q_1}{e_1} - \frac{Q_2}{e_2} \right) G_1 + \Omega_2^\dagger (V_1 - V_2) \Omega_1. \tag{45}$$

The second term on the rhs. is called the propagator-correction term; it vanishes if G_1 and G_2 have the same propagators. The third term is often referred to as the potential-correction term, and it disappears if G_1 and G_2 have the same potentials. The reader may now ask what is the advantage of the above identity. If we assume that by some physical reasoning we are able to calculate G_2 and that the expression for G_2 can be calculated easily, and

---

[3] For notational economy, we drop the superscript $[12]$. Furthermore, in the subsequent discussion in this subsection it is understood that all operators Q refer to particle–particle intermediate states only. The subscript pp is also dropped.

		Orbit number
⋮		
————	4s-3d-2g-1i-0k	37-45
————	3p-2f-1h-0j	29-36
————	3s-2d-1g-0i	22-28
————	2p-1f-0h	16-21
————	2s-1d-0g	11-15
————	1p-0f	7-10
————	1s-0d	4-6
————	0p	2-3
————	0s	1

Fig. 6. Classification of harmonic oscillator single-particle orbits.

further that G_2 is a good approximation to the original G-matrix, then we can use the above identity to perform a perturbative calculation of G_1 in terms of G_2.

Before we proceed in detailing the calculation of the G-matrix appropriate for finite nuclei, certain approximations need to be explained.

As discussed above, the philosophy behind perturbation theory is to reduce the intractable full Hilbert space problem to one which can be solved within a physically motivated model space, defined by the operator P. The excluded degrees of freedom are represented by the projection operator Q. The definition of these operators is connected with the nuclear system and the perturbative expansions discussed in Section 2. Consider the evaluation of the effective interaction needed in calculations of the low-lying states of ^{18}O. From experimental data and theoretical calculations the belief is that several properties of this nucleus can be described by a model space consisting of a closed ^{16}O core (consisting of the filled 0s- and 0p-shells) and two valence neutrons in the 1s0d-shell. In Fig. 6 we exhibit this division in terms of h.o. sp orbits. The active sp states in the 1s0d-shell are then given by the $0d_{5/2}$, $0d_{3/2}$ and $1s_{1/2}$ orbits, labels 4–6 in Fig. 6. The remaining states enter the definition of Q. Once we have defined P and Q we proceed in constructing the G-matrix and the corresponding perturbative expansion in terms of the G-matrix. There are however several ways of choosing Q. A common procedure is to specify the boundaries of Q by three numbers, n_1, n_2 and n_3, explained in Fig. 7. For ^{18}O we would choose $(n_1 = 3, n_2 = 6, n_3 = \infty)$. Our choice of P-space implies that the single-particle states outside the model space start from the 1p0f-shell (numbers 7–10 in Fig. 6), and orbits 1, 2 and 3 are hole states. Stated differently, this means that Q is constructed so as to prevent scattering into intermediate two-particle states with one particle in the 0s- or 0p-shells or both particles in the 1s0d-shell. This definition of the Q-space influences the determination of the effective shell-model interaction. Consider the diagrams displayed in Fig. 8. Diagram (a) of this figure is just the G-matrix and is allowed in the definition of the $\hat{Q}$-box. With our choice $(n_1 = 3, n_2 = 6, n_3 = \infty)$, diagram (b) is not allowed since the intermediate state consists of passive particle states and is already included in the evaluation of the G-matrix. Similarly, diagram (c) is also not allowed whereas diagram (d) is allowed. Now an important subtlety arises. If we evaluate the G-matrix with the
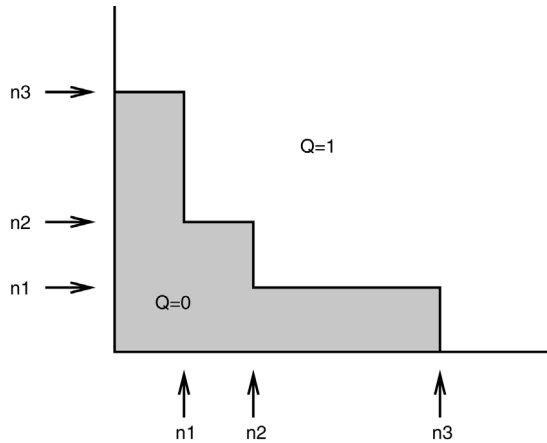
Fig. 7. Definition of the P (shaded area) and Q operators appropriate for the definition of the G-matrix and the effective interaction. Outside the shaded area limited by the boundaries n_1, n_2 and n_3 $P = 0$ and $Q = 1$.
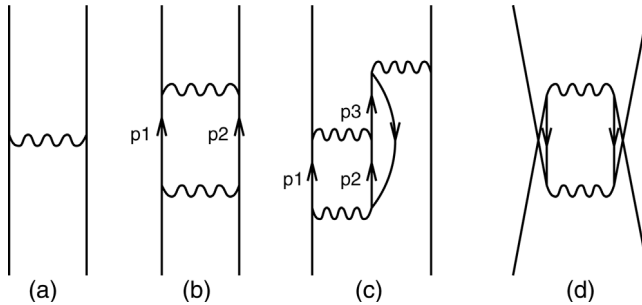
Fig. 8. Examples of diagrams which may define the effective valence space interaction. The wavy line is the G-matrix.

boundaries ($n_1 = 3$, $n_2 = 10$, $n_3 = \infty$), and define the P-space of *the effective interaction* by including orbits 4 to 6 only, then diagrams (b) and (c) are allowed if $7 \leq p_1, p_2 \leq 10$. In this way we allow for intermediate two-particle states as well with orbits outside the model-space of the effective interaction. The reader should notice the above differences, i.e. that the Q-space defining the G-matrix and H_{eff} may differ. In order to calculate the G-matrix we will henceforth employ a so-called double-partitioned scheme. Let us be more specific and detail this double-partitioned procedure. We define first a reference G-matrix $\tilde{G}$ in terms of plane wave intermediate states only, meaning that H_0 is replaced by the kinetic energy operator T only while G has harmonic oscillator intermediate states (this is one possible choice for U). We divide the exclusion operator into two parts, one which represents the low-lying states Q_l and one which accounts for high-lying states Q_h, viz.

$$Q = Q_l + Q_h = Q_l + \tilde{Q}.$$

If we consider ^{18}O as our pilot nucleus, we may define Q_l to consist of the sp orbits of the 1p0f-shell, orbits 7–10 in Fig. 6, described by h.o. states. Q_h represents then the remaining orthogonalized intermediate states. Using the identity of Bethe et al. [59] of Eq. (45) we can first set up $\tilde{G}$ as

$$\tilde{G} = V + V \frac{\tilde{Q}}{s - T} \tilde{G}, \tag{46}$$

and express G in terms of $\tilde{G}$ as

$$G = \tilde{G} + \tilde{G} \left(\frac{Q_l}{s - H_0} \right) G, \tag{47}$$

and we have assumed that $\tilde{G}$ is Hermitian and that $[Q_l, H_0] = 0$. Thus, we first calculate a "reference" G-matrix ($\tilde{G}$ in our case), and then insert this in the expression for the full G-matrix. The novelty here is that we are able to calculate $\tilde{G}$ exactly through operator relations to be discussed below. In passing we note that G depends significantly on the choice of H_0, though the low-lying intermediate states are believed to be fairly well represented by h.o. states. Also, the authors of [60] demonstrate that low-lying intermediate states are not so important in G-matrix calculations, being consistent with the short-range nature of the NN interaction. Since we let Q_l be defined by the orbits of the 1p0f-shell, and the energy difference between two particles in the sd-shell and pf-shell is of the order -14 MeV, we can treat G as a perturbation expansion in $\tilde{G}$. Eq. (47) can then be written as

$$G = \tilde{G} + \tilde{G} \left(\frac{Q_l}{s - H_0} \right) \tilde{G} + \tilde{G} \left(\frac{Q_l}{s - H_0} \right) \tilde{G} \left(\frac{Q_l}{s - H_0} \right) \tilde{G} + \cdots. \tag{48}$$

The only intermediate states are those defined by the 1p0f-shell. The second term on the rhs. is nothing but the second-order particle–particle ladder. The third term is then the third-order ladder diagram in terms of $\tilde{G}$. As shown by the authors of [60], the inclusion of the second-order particle–particle diagram in the evaluation of the $\hat{Q}$-box, represents a good approximation. The unsettled problem is however how to define the boundary between Q_l and Q_h.

Now we will discuss how to compute $\tilde{G}$. One can solve the equation for the G-matrix for finite nuclei by employing a formally exact technique for handling $\tilde{Q}$ discussed in e.g., [60]. Using the matrix identity

$$\tilde{Q} \frac{1}{\tilde{Q} A \tilde{Q}} \tilde{Q} = \frac{1}{A} - \frac{1}{A} \tilde{P} \frac{1}{\tilde{P} A^{-1} \tilde{P}} \tilde{P} \frac{1}{A}, \tag{49}$$

with $A = s - T$, to rewrite Eq. (46) as[4]

$$G = G_F + \Delta G, \tag{50}$$

---

[4] We will omit the label $\tilde{G}$ for the G-matrix for finite nuclei, however it is understood that the G-matrix for finite nuclei is calculated according to Eq. (46) This means that we have to include the particle–particle ladder diagrams in the $\hat{Q}$-box.

where G_F is the free G-matrix defined as

$$G_F = V + V \frac{1}{s - T} G_F. \tag{51}$$

The term ΔG is a correction term defined entirely within the model space $\tilde{P}$ and given by

$$\Delta G = -V \frac{1}{A} \tilde{P} \frac{1}{\tilde{P} A^{-1} \tilde{P}} \tilde{P} \frac{1}{A} V. \tag{52}$$

Employing the definition for the free G-matrix of Eq. (51), one can rewrite the latter equation as

$$\Delta G = -G_F \frac{1}{e} \tilde{P} \frac{1}{\tilde{P}(e^{-1} + e^{-1} G_F e^{-1}) \tilde{P}} \tilde{P} \frac{1}{e} G_F, \tag{53}$$

with $e = s - T$. We see then that the G-matrix for finite nuclei is expressed as the sum of two terms; the first term is the free G-matrix with no Pauli corrections included, while the second term accounts for medium modifications due to the Pauli principle. The second term can easily be obtained by some simple matrix operations involving the model-space matrix $\tilde{P}$ only. However, the second term is a function of the variable n_3. The convergence in terms of n_3 was discussed ad extenso in [16] and we refer the reader to that work. The equation for the free matrix G_F is solved in momentum space in the relative and center-of-mass system and thereafter transformed to the relevant expression in terms of harmonic oscillator single-particle wave functions in the laboratory system. This yields final matrix elements of the type

$$\langle (ab) J | G | (cd) J \rangle \tag{54}$$

where G is given by the sum $G = G_F + \Delta G$. The label a represents here all the single particle quantum numbers $n_a l_a j_a$.

3.2. Modified Hilbert space for resummation of large sets of diagrams

In Fig. 7 the numbers n_1, n_2 and n_3 were used to define hole and particle states with respect to a given nucleus. We could also define a huge model space which does not reflect a particular core and thereby nucleus. One possible way of defining such a no-core model space is obtained by setting $n_1 = n_2 = n_3$, with n_3 representing a large number, at least some eight-ten major oscillator shells. The single-particle states labeled by n_3 represent then the last orbit of the model space $\tilde{P}$, following the numbering indicated in Fig. 6. This so-called no-core model space is indicated in Fig. 9 and will be used in our definitions of model spaces for the resummations of parquet diagrams and many-body terms in coupled-cluster theory. In Fig. 9 the two-body state $|(pq) J T_Z\rangle$ does not belong to the model space and is included in the computation of the G-matrix. Similarly, $|(p\gamma) J T_Z\rangle$ and $|(\delta q) J T_Z\rangle$ also enter the definition of $\tilde{Q}$ whereas $|(\delta\gamma) J T_Z\rangle$ is not included in the computation of G. This means that correlations not defined in the G-matrix need to be computed by other non-perturbative resummations or many-body schemes. This is where the coupled-cluster scheme and the parquet approaches enter.

With the G-matrix model space $\tilde{P}$ of Fig. 9 we can now define an appropriate space for many-body perturbation theory, parquet diagrams or coupled-cluster calculations where
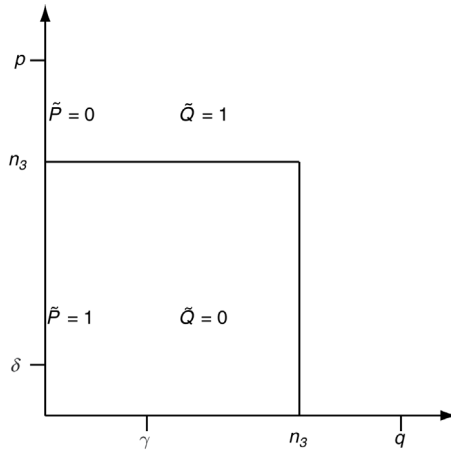
Fig. 9. Definition of the exclusion operator used to compute the G-matrix for large spaces.
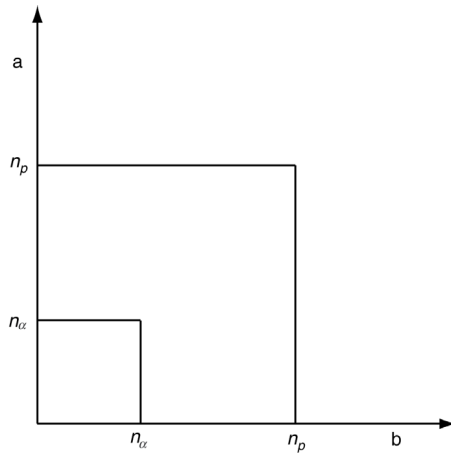
Fig. 10. Definition of particle and hole states for coupled-cluster, parquet diagrams and perturbative many-body calculations in large spaces. The orbit represented by n_α stands for the last hole state whereas n_p represents the last particle orbit included in the G-matrix model space. The hole states define the Fermi energy.

correlations not included in the G-matrix are to be generated. This model space is defined in Fig. 10, where the label n_p represents the same single-particle orbit as n_3 in Fig. 9.

The G-matrix computed according to Fig. 9 does not reflect a specific nucleus and thereby single-particle orbits which define the uncorrelated Slater determinant. For a nucleus like ^{4}He the $0s_{1/2}$ orbit is fully occupied and defines thereby single-hole states. These are labeled by n_α in Fig. 10. For ^{16}O the corresponding hole states are represented by the orbits $0s_{1/2}$, $0p_{3/2}$ and $0p_{1/2}$. With this caveat we can then generate correlations not included in the G-matrix and hopefully perform resummations of larger classes of diagrams.

Fig. 11. Binding energy per particle E/A from third-order perturbation theory for ^{16}O as function of the number of major harmonic oscillator shells N and the oscillator energy $\hbar\omega$. For $N = 8$ we have the optimal value of $E/A = -7.12$ MeV at $\hbar\omega = 13.6$ MeV. The experimental value is $E/A = -7.98$ MeV.
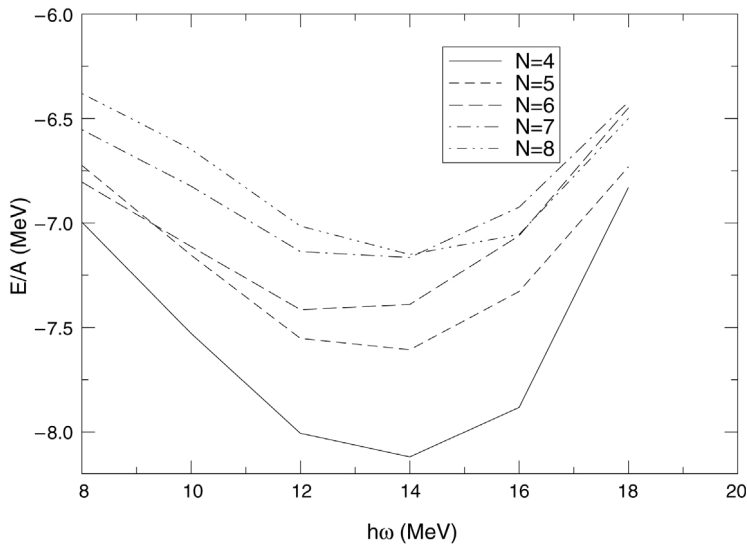
To demonstrate the dependence upon the size of the enlarged model-space defined by n_p, We present here results from third order in perturbation theory for the binding energy of ^{16}O as a function of the size of the model space and the chosen oscillator energy $\hbar\omega$. These results are shown in Fig. 11.

There are several features to be noted. First of all one notices that the results seem to stabilize between seven and eight major shells. The fact that the energies seem to converge at this level of truncation is a welcome feature which can be exploited in the coupled-cluster and parquet diagram calculations. These calculations, see below, are much more challenging from a computational point of view since we in principle generate a much larger class of coupled-cluster calculations.

Secondly, although the minimum shifts a little as a function of the oscillator energy as we increase the oscillator space, we notice that as the number of major shells is increased, the dependence of the binding energy upon the oscillator parameter weakens. A similar feature is seen in the coupled-cluster calculations below. For ^{16}O the minimum for seven shells takes place at $E/A = -7.16$ MeV for $\hbar\omega = 12.9$ MeV and for eight shells we have $E/A = -7.12$ MeV at $\hbar\omega = 13.6$ MeV. For six shells we obtain $E/A = -7.42$ MeV at $\hbar\omega = 12.6$ MeV. The curvature for larger values of $\hbar\omega$ decreases with increasing number of shells N. At $\hbar\omega = 18$ MeV we have for ^{16}O and $N = 8$ that $d(E/A)/d\omega = 0.22$, for $N = 7$ we obtain $d(E/A)/d\omega = 0.28$ and $N = 6$ we have $d(E/A)/d\omega = 0.35$. The reader should also note that in the limit $\hbar\omega \to 0$ we have $E \to 0$.

We do not expect to reproduce the experimental binding energies. This calculation does not include the Coulomb interaction or realistic three-body interactions. The latter will be discussed in Section 7.

3.3. Folded diagrams and the effective valence space interaction

Here we discuss further classes of diagrams which can be included in the evaluation of effective interactions for the shell model. Here we will focus on the summations of so-called folded diagrams.

One way of obtaining the wave operator Ω is through the generalized Bloch equation given by Lindgren and Morrison [17]

$$[\Omega, H_0]P = QH_1\Omega P - \chi P H_1 \Omega P, \tag{55}$$

which offers a suitable way of generating the RS perturbation expansion. Writing Eq. (55) in terms of $\Omega^{(n)}$ we have

$$[\Omega^{(1)}, H_0]P = QH_1P, \tag{56}$$
$$[\Omega^{(2)}, H_0]P = QH_1\Omega^{(1)}P - \Omega^{(1)}PH_1P, \tag{57}$$

and so forth, which can be generalized to

$$[\Omega^{(n)}, H_0]P = QH_1\Omega^{(n-1)}P - \sum_{m=1}^{n-1} \Omega^{(n-m)} P H_1 \Omega^{(m-1)} P. \tag{58}$$

The effective interaction to a given order can then be obtained from $\Omega^{(n)}$, see [17]. Another possibility is obviously the coupled-cluster method discussed below.

Here we will assume that we can start with a given approximation to Ω, and through an iterative scheme generate higher-order terms. Such schemes will in general differ from the order-by-order scheme of Eq. (55). Two such iterative schemes were derived by Lee and Suzuki [61]. We will focus on the folded diagram method of Kuo and co-workers [15].

Having defined the wave operator $\Omega = 1 + \chi$ (note that $\Omega^{-1} = 1 - \chi$) with χ given by Eq. (9) we can obtain

$$QHP - \chi HP + QH\chi - \chi H\chi = 0. \tag{59}$$

This is the basic equation to which a solution to χ is to be sought. If we choose to work with a degenerate model space we define

$$PH_0P = sP,$$

where s is the unperturbed model space eigenvalue (or starting energy) in the degenerate case, such that Eq. (59) reads in a slightly modified form ($H = H_0 + H_1$)

$$(s - QH_0Q - QH_1Q)\chi = QH_1P - \chi PH_1P - \chi PH_1Q\chi,$$

which yields the following equation for χ

$$\chi = \frac{1}{s - QHQ}QH_1P - \frac{1}{s - QHQ}\chi(PH_1P + PH_1Q\chi P). \tag{60}$$

Observing that the P-space effective Hamiltonian is given as

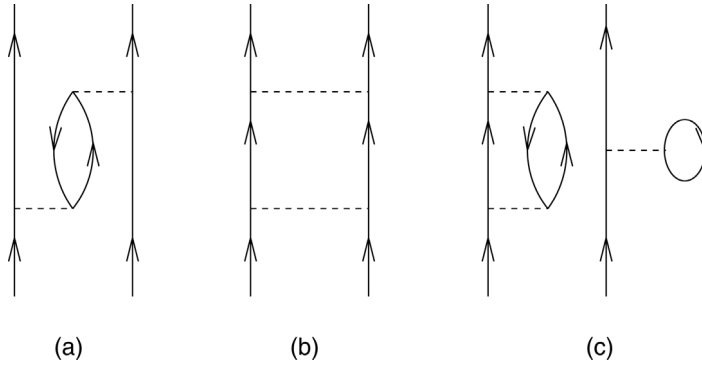$$H_{\text{eff}} = PHP + PH\chi = PH_0P + V_{\text{eff}}(\chi),$$

Fig. 12. Different types of valence-linked diagrams. Diagram (a) is irreducible and connected, (b) is reducible, while (c) is irreducible and disconnected.

with $V_{\text{eff}}(\chi) = P H_1 P + P H_1 Q \chi P$, Eq. (60) becomes

$$\chi = \frac{1}{s - Q H Q} Q H_1 P - \frac{1}{s - Q H Q} \chi V_{\text{eff}}(\chi). \tag{61}$$

Now we find it convenient to introduce the so-called $\hat{Q}$-box, defined as

$$\hat{Q}(s) = P H_1 P + P H_1 Q \frac{1}{s - Q H Q} Q H_1 P. \tag{62}$$

The $\hat{Q}$-box is made up of non-folded diagrams which are irreducible and valence linked. A diagram is said to be irreducible if between each pair of vertices there is at least one hole state or a particle state outside the model space. In a valence-linked diagram the interactions are linked (via fermion lines) to at least one valence line. Note that a valence-linked diagram can be either connected (consisting of a single piece) or disconnected. In the final expansion including folded diagrams as well, the disconnected diagrams are found to cancel out [15]. This corresponds to the cancellation of unlinked diagrams of the Goldstone expansion. We illustrate these definitions by the diagrams shown in Fig. 12. Diagram (a) is irreducible, valence linked and connected, while (b) is reducible since the intermediate particle states belong to the model space. Diagram (c) is irreducible, valence linked and disconnected. It is worth noting that the general form of the $\hat{Q}$-box is the same as that of the G-matrix, or the equations of the [12] channel or those of the [13] and [14] channels to be discussed in Section 4. In [16], the $\hat{Q}$-box was defined to be the sum of all diagrams to third order in the G-matrix.

Multiplying both sides of Eq. (61) with $P H_1$ and adding $P H_1 P$ to both sides we get

$$P H_1 P + P H_1 \chi = P H_1 P + P H_1 Q \frac{1}{s - Q H Q} Q H_1 P - P H_1 \frac{1}{s - Q H Q} \chi V_{\text{eff}}(\chi),$$

which gives

$$V_{\text{eff}}(\chi) = \hat{Q}(s) - P H_1 \frac{1}{s - Q H Q} \chi V_{\text{eff}}(\chi). \tag{63}$$

There are several ways to solve Eq. (63). The idea is to set up an iteration scheme where we determine χ_n and thus $V_{\text{eff}}(\chi_n)$ from χ_{n-1} and $V_{\text{eff}}(\chi_{n-1})$. For the mere sake of simplicity we write $V_{\text{eff}}^{(n)} = V_{\text{eff}}(\chi_n)$.

Let us write Eq. (63) as

$$V_{\text{eff}}^{(n)} = \hat{Q}(s) - PH_1 \frac{1}{s - QHQ} \chi_n V_{\text{eff}}^{(n-1)}.$$

The solution to this equation can be shown to be [61]

$$V_{\text{eff}}^{(n)} = \hat{Q} + \sum_{m=1}^{\infty} \frac{1}{m!} \frac{\mathrm{d}^m \hat{Q}}{\mathrm{d}s^m} \{V_{\text{eff}}^{(n-1)}\}^m. \tag{64}$$

Observe also that the effective interaction is $V_{\text{eff}}^{(n)}$ is evaluated at a given model space energy s. If $V_{\text{eff}}^{(n)} = V_{\text{eff}}^{(n-1)}$, the iteration is said to converge. In the limiting case $n \to \infty$, the solution $V_{\text{eff}}^{(\infty)}$ agrees with the formal solution of Brandow [14] and Des Cloizeaux [62]

$$V_{\text{eff}}^{(\infty)} = \sum_{m=0}^{\infty} \frac{1}{m!} \frac{\mathrm{d}^m \hat{Q}}{\mathrm{d}s^m} \{V_{\text{eff}}^{(\infty)}\}^m. \tag{65}$$

Alternatively, we can generate the contribution from n folds by the following way. In an n-folded $\hat{Q}$-box there are of course $n+1$ $\hat{Q}$-boxes. The general expression for an n-folded $\hat{Q}$-box is then

$$\hat{Q} - \hat{Q} \int \hat{Q} + \hat{Q} \int \hat{Q} \int \hat{Q} - \cdots = \sum_{m_1 m_2 \dots m_n} \frac{1}{m_1!} \frac{\mathrm{d}^{m_1} \hat{Q}}{\mathrm{d}s^{m_1}} P \frac{1}{m_2!} \frac{\mathrm{d}^{m_2} \hat{Q}}{\mathrm{d}s^{m_2}} P$$
$$\cdots \frac{1}{m_n!} \frac{\mathrm{d}^{m_n} \hat{Q}}{\mathrm{d}s^{m_n}} P \hat{Q}, \tag{66}$$

where we have the constraints

$$m_1 + m_2 + \cdots + m_n = n,$$
$$m_1 \geq 1,$$
$$m_2, m_3, \ldots, m_n \geq 0,$$

and

$$m_k \leq n - k + 1.$$

The last restriction follows from the fact that there are only $n - k + 1$ $\hat{Q}$-boxes to the right of the kth $\hat{Q}$-box. Thus, it can at most be differentiated $n - k + 1$ times. We have inserted the model-space projection operator in the above expression, in order to emphasize that folded diagrams have as intermediate states between successive $\hat{Q}$-boxes only model-space states. Therefore, the sum in Eq. (66) includes a sum over all model-space states with the same quantum numbers such as isospin and total angular momentum. It is understood that the $\hat{Q}$-box and its derivatives are evaluated at the same starting energy, which should correspond to the unperturbed energy of the model-space state. It is then straightforward to recast Eq. (66) into the form of Eq. (64).

Note that although $\hat{Q}$ and its derivatives contain disconnected diagrams, such diagrams cancel exactly in each order [15], thus yielding a fully connected expansion in Eq. (64). However, in order to achieve this, disconnected diagrams have to be included in the definition of the $\hat{Q}$-box. An example is given by diagram (c) Fig. 12. Such a diagram will generate a contribution to the first fold $\frac{d\hat{Q}}{ds}\hat{Q} = -\hat{Q}\int\hat{Q}$ which cancels exactly diagram (c) when all time-ordered contributions to this diagram are accounted for, see [15] for more details. It is moreover important to note in connection with the above expansion, that a term like $F_1 = \hat{Q}_1\hat{Q}$ actually means $P\hat{Q}_1P\hat{Q}P$ since the $\hat{Q}$-box is defined in the model space only. Here we have defined $\hat{Q}_m = \frac{1}{m!}\frac{d^m\hat{Q}}{ds^m}$. Due to this structure, only so-called folded diagrams contain P-space intermediate states.

The folded diagram expansion discussed above yields however a non-Hermitian effective interaction. This happens even at the level of the G-matrix. A Hermitian effective interaction has recently been derived by Suzuki and co-workers [13, 18, 63] through the following steps.[5] To obtain a Hermitian effective interaction, let us define a model-space eigenstate $|b_\lambda\rangle$ with eigenvalue λ as

$$|b_\lambda\rangle = \sum_{\alpha=1}^{D} b_\alpha^{(\lambda)}|\psi_\alpha\rangle \tag{67}$$

and the biorthogonal wave function

$$|\overline{b}_\lambda\rangle = \sum_{\alpha=1}^{D} \overline{b}_\alpha^{(\lambda)}|\overline{\psi}_\alpha\rangle, \tag{68}$$

such that

$$\langle\overline{b}_\lambda|b_\mu\rangle = \delta_{\lambda\mu}. \tag{69}$$

The model-space eigenvalue problem can be written in terms of the above non-Hermitian effective interaction unperturbed wave functions

$$\sum_{\gamma=1}^{D} b_l^{(\lambda)}\langle\psi_\sigma|H_0 + V + VQ\chi|\psi_\gamma\rangle = E_\lambda b_\sigma^{(\lambda)}. \tag{70}$$

The exact wave function expressed in terms of the correlation operator is

$$|\Psi_\lambda\rangle = (\mathbf{1} + \chi)|\psi_\lambda\rangle. \tag{71}$$

The part $\chi|\psi_\lambda\rangle$ can be expressed in terms of the time-development operator or using the time-independent formalism as

$$\chi|\psi_\lambda\rangle = \frac{Q}{E_\lambda - QHQ}QVP|\psi_\lambda\rangle, \tag{72}$$

where Q is the exclusion operator. Note that this equation is given in terms of the Brillouin–Wigner perturbation expansion, since we have the exact energy E_λ in the denominator.

---

[5] The reader who wishes more details can consult [13, 63].

Using the normalization condition for the true wave function we obtain

$$\langle \Psi_\gamma | \Psi_\lambda \rangle N_\lambda \delta_{\lambda\gamma} = \langle \psi_\gamma | (\mathbf{1} + \chi^\dagger \chi) | \psi_\lambda \rangle, \tag{73}$$

where we have used the fact that $\langle \psi_\gamma | \chi | \psi_\lambda \rangle = 0$. Recalling that the time-development operator is Hermitian we have that $\chi^\dagger \chi$ is also Hermitian. We can then define an orthogonal basis d whose eigenvalue relation is

$$\sum_\alpha \langle \psi_\beta | \chi^\dagger \chi | \psi_\alpha \rangle d_\alpha^\lambda = \mu_\lambda^2 d_\beta^\lambda, \tag{74}$$

with eigenvalues greater than 0. Using the definition in Eq. (72), we note that the diagonal element of

$$\langle \psi_\lambda | \chi^\dagger \chi | \psi_\lambda \rangle = \langle \psi_\lambda | P V Q \frac{1}{(E_\lambda - QHQ)^2} QVP | \psi_\lambda \rangle, \tag{75}$$

which is nothing but the derivative of the $\hat{Q}$-box, with an additional minus sign. Thus, noting that if $\gamma \neq \lambda$

$$\langle \Psi_\gamma | \Psi_\lambda \rangle = 0 = \langle \psi_\gamma | \psi_\lambda \rangle + \langle \psi_\gamma | \chi^\dagger \chi | \psi_\lambda \rangle, \tag{76}$$

we can write $\chi^\dagger \chi$ in operator form as

$$\chi^\dagger \chi = - \sum_\alpha | \overline{\psi}_\alpha \rangle \langle \psi_\alpha | \hat{Q}_1(E_\alpha) | \psi_\alpha \rangle \langle \overline{\psi}_\alpha | - \sum_{\alpha \neq \beta} | \overline{\psi}_\alpha \rangle \langle \psi_\alpha | \psi_\beta \rangle | \overline{\psi}_\beta \rangle. \tag{77}$$

Using the new basis in Eq. (74), we see that Eq. (73) allows us to define another orthogonal basis h

$$h_\alpha^\lambda = \sqrt{\mu_\alpha^2 + 1} \sum_\beta d_\beta^\alpha b_\beta^\lambda \frac{1}{\sqrt{N_\lambda}} = \frac{1}{\sqrt{\mu_\alpha^2 + 1}} \sum_\beta d_\beta^\alpha \overline{b}_\beta^\lambda \sqrt{N_\lambda}, \tag{78}$$

where we have used the orthogonality properties of the vectors involved. The vector h was used by the authors of [63] to obtain a Hermitian effective interaction as

$$\langle \psi_\alpha | V_{\text{eff}}^{(\text{her})} | \psi_\beta \rangle = \frac{\sqrt{\mu_\alpha^2 + 1} \langle \psi_\alpha | V_{\text{eff}}^{(\text{nher})} | \psi_\beta \rangle + \sqrt{\mu_\beta^2 + 1} \langle \psi_\alpha | V_{\text{eff}}^{\dagger(\text{nher})} | \psi_\beta \rangle}{\sqrt{\mu_\alpha^2 + 1} + \sqrt{\mu_\beta^2 + 1}}, \tag{79}$$

where (her) and (nher) stand for Hermitian and non-Hermitian respectively. This equation is rather simple to compute, since we can use the folded-diagram method to obtain the non-Hermitian part. To obtain the total Hermitian effective interaction, we have to add the H_0 term. The above equation is manifestly Hermitian. Other discussions of the hermiticity problem can be found in [17, 27]. The remaining question is how to evaluate the $\hat{Q}$-box. Obviously, we are not in the position where we can evaluate it exactly, i.e., to include all possible many-body terms. Rather, we have to truncate somewhere. Several possible approaches exist, but all have in common that there is no clear way which tells us where to stop. However, as argued by the authors of [40], there is a minimal class of diagrams which need to be included in order to fulfil necessary conditions. This class of diagrams includes both diagrams which account for short-range correlations such as the *G*-matrix

and long-range correlations such as those accounted for by various core-polarization terms. The importance of such diagrams has been extensively documented in the literature and examples can be found in [16, 48]. In [16] we included all core-polarization contributions to third-order in the G-matrix, in addition to including other diagrams which account for short-range correlations as well.

In all our results presented in Section 4 we employ a third-order $\hat{Q}$-box using the CD-Bonn interaction model described in [64, 65]. Moreover, the procedure for obtaining a Hermitian procedure discussed in Eq. (79) is employed in Section 4.9. In our coupled-cluster calculations we employ the recent chiral model Idaho-A of Entem and Machleidt, see for example [66].

3.4. Center-of-mass corrections

Momentum conservation requires that a many-body wave function must factorize as $\Psi(\mathbf{r}) = \phi(R)\Psi(\mathbf{r}_{rel})$ where R is the center-of-mass (CoM) coordinate and $\mathbf{r}_{rel}$ the relative coordinates. If we choose to expand our wave functions in the harmonic oscillator basis, then we are able to exactly separate the center-of-mass motion from the problem provided that we work in a model space that includes all $n\hbar\Omega$ excitations. In our coupled-cluster calculations we have a Q operator that allows for all possible two-particle interactions within a given set of oscillator shells. This means that we are $n\hbar\Omega$ incomplete in a given calculation so that our method of separation of the center-of-mass motion becomes approximate. For example, for ^{4}He in four major oscillator shells, we can excite all particles to $n = 12\hbar\Omega$ excitations, but we can only excite one particle to $n = 3\hbar\Omega$ excitations. Thus, care must be taken when correcting for center-of-mass contamination in our calculations. We have taken a variational approach based on the the work of Whitehead et al. [67]. The idea is to add $\beta_{CoM}H_{CoM}$ to the Hamiltonian, but with β_{CoM} remaining fairly small. This minimizes the effects of the center-of-mass contamination on low-lying state properties, and partially pushes unwanted states out of the spectrum. If we were to use a large β_{CoM}, we would find spurious states entering into the calculated low-lying spectrum due to the incompleteness of our model space.

The CoM Hamiltonian is then

$$H_{CoM} = \frac{\mathbf{P}^2}{2MA} + \frac{1}{2}mA\Omega^2\mathbf{R}^2 - \frac{3}{2}\hbar\Omega, \tag{80}$$

where $\mathbf{P} = \sum_{i=1,A}\mathbf{p}_i$ and $R = (\sum_{i=1,A}\mathbf{r}_i)/A$. The term H_{CoM} can be rewritten as a one-body harmonic potential, and a two-body term that depends on both the relative and center-of-mass coordinates of the two interacting particles. The matrix elements for the two-body terms may be found in [68]. Operationally, we add H_{CoM} to our Hamiltonian

$$H' = H + \beta_{CoM}H_{CoM}, \tag{81}$$

where we choose β_{CoM} so that the expectation value of H_{CoM} is zero [69]. This insures that our center-of-mass contamination within the many-body wave function is minimized. We also find that this procedure yields reasonable spectra (in a space of four major

oscillator shells) for ^{4}He [70]. This approach is used in our coupled-cluster calculations in Section 6 and in the shell-model Monte Carlo calculations of properties of 1s0d–1p0f-shell nuclei, see Section 4 and [69]. In our shell-model calculations we employ the standard procedure of Lawson, see [68].

There are at least two other widely used ways of dealing with the CoM corrections. The philosophy is

- One starts with a *translationally* invariant Hamiltonian, kinetic energy plus e.g., two-body interaction. From that one the harmonic oscillator field is introduced. This is then split up into a pure CoM term and a two-body term which depends on the radial distance.
- One starts with the harmonic oscillator as the one-body piece plus a two-body interaction. The one-body piece can be rewritten in terms of a pure CoM term and a two-body term which now depends on the relative distance and momentum.

In deriving the CoM corrections, the following expressions are helpful. The CoM momentum is

$$P = \sum_{i=1}^{A} \vec{p}_i, \tag{82}$$

and we have that

$$\sum_{i=1}^{A} \vec{p}_i^2 = \frac{1}{A}\left[\vec{P}^2 + \sum_{i<j}(\vec{p}_i - \vec{p}_j)^2 \right] \tag{83}$$

meaning that

$$\left[\sum_{i=1}^{A} \frac{\vec{p}_i^2}{2m} - \frac{\vec{P}^2}{2mA} \right] = \frac{1}{2mA}\sum_{i<j}(\vec{p}_i - \vec{p}_j)^2. \tag{84}$$

The last expression is explicitly translationally invariant.

In a similar fashion we can define the CoM coordinate

$$\vec{R} = \frac{1}{A}\sum_{i=1}^{A} \vec{r}_i, \tag{85}$$

which yields

$$\sum_{i=1}^{A} \vec{r}_i^2 = \frac{1}{A}\left[\vec{R}^2 + \sum_{i<j}(\vec{r}_i - \vec{r}_j)^2 \right]. \tag{86}$$

If we then introduce the harmonic oscillator one-body Hamiltonian

$$H_0 = \sum_{i=1}^{A}\left(\frac{\vec{p}_i^2}{2m} + \frac{1}{2}m\Omega^2\vec{r}_i^2 \right), \tag{87}$$

with Ω the oscillator frequency, we can rewrite the latter as

$$H_{\text{HO}} = \frac{\vec{P}^2}{2mA} + \frac{mA\Omega^2\vec{R}^2}{2} + \frac{1}{2mA}\sum_{i<j}(\vec{p}_i - \vec{p}_j)^2 + \frac{m\Omega^2}{2A}\sum_{i<j}(\vec{r}_i - \vec{r}_j)^2, \qquad (88)$$

or just

$$H_{\text{HO}} = H_{\text{CoM}} + \frac{1}{2mA}\sum_{i<j}(\vec{p}_i - \vec{p}_j)^2 + \frac{m\Omega^2}{2A}\sum_{i<j}(\vec{r}_i - \vec{r}_j)^2, \qquad (89)$$

with

$$H_{\text{CoM}} = \frac{\vec{P}^2}{2mA} + \frac{mA\Omega^2\vec{R}^2}{2}. \qquad (90)$$

In shell-model studies the translationally invariant one- and two-body Hamiltonian reads for an A-nucleon system,

$$H = \left[\sum_{i=1}^{A}\frac{\vec{p}_i^2}{2m} - \frac{\vec{P}^2}{2mA}\right] + \sum_{i<j}^{A}V_{ij}, \qquad (91)$$

where m is the nucleon mass and V_{ij} the nucleon–nucleon interaction, is modified by including the harmonic oscillator potential through the following

$$\sum_{i=1}^{A}\frac{1}{2}m\Omega^2\vec{r}_i^2 - \frac{m\Omega^2}{2A}\left[\vec{R}^2 + \sum_{i<j}(\vec{r}_i - \vec{r}_j)^2\right] = 0. \qquad (92)$$

We can rewrite the Hamiltonian of Eq. (91) as

$$H^{\Omega} = \sum_{i=1}^{A}\left[\frac{\vec{p}_i^2}{2m} + \frac{1}{2}m\Omega^2\vec{r}_i^2\right] + \sum_{i<j}^{A}\left[V_{ij} - \frac{m\Omega^2}{2A}(\vec{r}_i - \vec{r}_j)^2\right] - H_{\text{CoM}}. \qquad (93)$$

Shell-model calculations are carried out in a model space defined by a projector P. The complementary space to the model space is defined by the projector $Q = 1 - P$. Consequently, for the P-space part of the shell-model Hamiltonian we get

$$H_P^{\Omega} = \sum_{i=1}^{A}P\left[\frac{\vec{p}_i^2}{2m} + \frac{1}{2}m\Omega^2\vec{r}_i^2\right]P + \sum_{i<j}^{A}P\left[V_{ij} - \frac{m\Omega^2}{2A}(\vec{r}_i - \vec{r}_j)^2\right]_{\text{eff}}P$$
$$- PH_{\text{CoM}}P. \qquad (94)$$

The effective interaction appearing in Eq. (94) is in general an A-body interaction and if it is determined without any approximations, the model-space Hamiltonian provides an identical description of a subset of states as the full-space Hamiltonian (93). The intrinsic properties of the many-body system still do not depend on Ω. From among the eigenstates of the Hamiltonian (94), it is necessary to choose only those corresponding to the same CoM energy. This can be achieved by projecting the CoM eigenstates with energies greater than $(3/2)\hbar\Omega$ upwards in the energy spectrum.

The effective interaction should be determined from H^{Ω} (93). Calculation of the exact A-body effective interaction is, however, as difficult as finding the full space solution. Usually, the effective interaction is approximated by a two-body effective interaction determined from a two-nucleon problem. The relevant two-nucleon Hamiltonian obtained from (93) is then

$$H_2^{\Omega} \equiv H_{02}^{\Omega} + V_2^{\Omega} = \frac{\vec{p}_1^2 + \vec{p}_2^2}{2m} + \frac{1}{2}m\Omega^2(\vec{r}_1^2 + \vec{r}_2^2) + V(\vec{r}_1 - \vec{r}_2)$$
$$- \frac{m\Omega^2}{2A}(\vec{r}_1 - \vec{r}_2)^2. \tag{95}$$

With this Hamiltonian we can then compute a starting-energy-dependent effective interaction or G-matrix corresponding to a two-nucleon model space defined by the projector P_2. This G-matrix reads

$$G(\omega) = V_2^{\Omega} + V_2^{\Omega} Q_2 \frac{1}{\omega - Q_2 H_2^{\Omega} Q_2} Q_2 V_2^{\Omega}, \tag{96}$$

where $Q_2 = 1 - P_2$ and V_2^{Ω} is the interaction given by the last two terms on the rhs. of Eq. (95). Using a similarity transformation introduced by Suzuki and Okamoto [13], Navrátil et al. used the above Hamiltonian to define an effective two-body interaction for no-core calculations, see for example [74]. The CoM corrections can easily be implemented within such a scheme. For a standard G-matrix this is more difficult since such calculations are typically done in momentum space. We have however applied the CoM correction to the bare potential in a perturbative way in [71].

If we however start with a harmonic oscillator basis we have

$$H^{\Omega} = \sum_{i=1}^{A} \left[\frac{\vec{p}_i^2}{2m} + \frac{1}{2}m\Omega^2\vec{r}_i^2 \right] + \sum_{i<j}^{A} V_{ij}. \tag{97}$$

If we then use Eq. (88), we obtain the following expression for our Hamiltonian

$$H^{\omega} = \frac{\vec{P}^2}{2mA} + \frac{mA\Omega^2\vec{R}^2}{2} + \frac{1}{2mA}\sum_{i<j}(\vec{p}_i - \vec{p}_j)^2 + \frac{m\Omega^2}{2A}\sum_{i<j}(\vec{r}_i - \vec{r}_j)^2$$
$$+ \sum_{i<j}^{A} V_{ij}, \tag{98}$$

or

$$H^{\omega} = H_{\mathrm{CoM}} + \frac{1}{2mA}\sum_{i<j}(\vec{p}_i - \vec{p}_j)^2 + \frac{m\Omega^2}{2A}\sum_{i<j}(\vec{r}_i - \vec{r}_j)^2 + \sum_{i<j}^{A} V_{ij}, \tag{99}$$

which differs from Eq. (94) by the sign of the CoM contribution and the two-body part which now reads

$$V_2^{\omega} = V(\vec{r}_1 - \vec{r}_2) - \frac{m\Omega^2}{2A}(\vec{r}_1 - \vec{r}_2)^2 - \frac{1}{2mA}(\vec{p}_i - \vec{p}_j)^2, \tag{100}$$

Table 1
Shell-model dimensionalities for selected nuclei around $A \sim 100$

System	Dimension	System	Dimension
^{104}Sn	$\approx 1.5 \times 10^3$	^{112}Sn	$\approx 6.2 \times 10^6$
^{108}Sn	$\approx 3.2 \times 10^5$	^{116}Sn	$\approx 1.6 \times 10^7$
^{104}Sb	$\approx 6.5 \times 10^3$	^{112}Sb	$\approx 1.1 \times 10^8$
^{108}Sb	$\approx 3.2 \times 10^6$	^{116}Sb	$\approx 1.9 \times 10^9$

which should be contrasted to

$$V_2^{\Omega} = V(\vec{r}_1 - \vec{r}_2) - \frac{m\Omega^2}{2A}(\vec{r}_1 - \vec{r}_2)^2.$$

A thorough discussion of various approaches to the CoM problem within the context of the coupled-cluster method and summation of parquet diagrams will be presented in future works [72].

4. Shell-model studies of selected nuclei

The shell-model problem requires the solution of a real symmetric $n \times n$ matrix eigenvalue equation

$$H|vec_k\rangle = E_k|vec_k\rangle, \tag{101}$$

with $k = 1, \ldots, K$. The eigenvalues E_k are understood to be numbered in increasing order. In a typical shell-model problem we are interested in only the lowest eigenstates of Eq. (101), so K may be of the order of 10 to 50. The total dimension n of the eigenvalue matrix H is large, for the Sn isotopes of interest up to $n \approx 2 \times 10^7$. Consider for example the case of a shell-model calculation outside the $Z = 50$ $N = 50$ core with the single-particle orbits $1d_{5/2}$, $0g_{7/2}$, $1d_{3/2}$, $2s_{1/2}$ and $0h_{11/2}$ defining the shell-model space. Table 1 shows examples of dimensionalities encountered for different nuclei. Such large matrix problems are increasingly used in science and engineering and practical numerical algorithms for determining their properties are continually being developed. These methods are closely related to the development of modern computer technology, both hardware and software. What was impossible to solve a few years ago may now be within reach and we should also be prepared for an increased future development. To indicate the present possibility, in a work by Olsen et al. [73] in a quantum chemistry configuration interaction calculation, Eq. (101) was solved in a basis with $n = 10^9$. In nuclear physics there are presently several groups dedicated to the development of shell-model codes which can deal with systems with similar large dimensionalities. Notable are the Iowa–Livermore–Tucson group [74], the Michigan group with e.g., the OXBASH code [5, 75, 76], the Oak Ridge group [77], the Oslo group [78] and the Strasbourg group [79], just to mention a few. All these codes are nowadays capable of dealing with nuclear systems with dimensionalities of $n \sim 10^9$ basic states. Extensive full fp-shell model and partial sd–fp calculations have been carried out by the Strasbourg group [80–83]. Similarly, the Iowa–Livermore–Tucson group

has dealt with no-core shell-model calculations of light nuclei [1–4], with a very good agreement with the ab initio Green's function Monte Carlo calculations of the Argonne group [10–12].

Even larger shell-model dimensionalities can be dealt with e.g., Monte Carlo shell-model approaches developed by Otsuka and collaborators [6, 84, 85] and the shell-model Monte Carlo approach of Koonin et al. [7].

Below we will focus on results for medium heavy nuclei in the mass regions from $A = 100$ to $A = 140$ based on the Oslo shell-model code [78].

Different computational approaches to solve Eq. (101) can be distinguished based on the size of n. For n small, i.e. $10^2 < n < 10^3$ and with the number of matrix elements of H less than 10^6 such problems can be accommodated within the direct access memory of a modern work station and can be diagonalized by standard matrix routines. In a second domain with $n > 10^3$ but small enough that H has no more than 10^8 elements. This will require ≈ 1.5 GB of storage. Then all matrix elements may be stored in the memory or alternatively on a standard disk. In these cases the complete diagonalization of H will not be of physical interest and efficient iteration procedures have been developed to find the lowest energy eigenvalues and eigenvectors.

Based on the present computer methods we have developed a code which is under continuous improvement to solve the eigenvalue problem given in Eq. (101). The basic requirement is to be able to handle problems with $n > 10^6$. In the following we discuss some of the important elements which enter the algorithm.

We separate the discussion into three parts:

- The m-scheme representation of the basic states.
- The Lanczos iteration algorithm.
- The Davidson–Liu iteration technique.

4.1. The m-scheme representation

We write the eigenstates in Eq. (101) as linear combinations of Slater determinants. In a second quantization representation a Slater determinant (SD) is given by

$$|SD_\nu(N)\rangle = \prod_{(jm) \in \nu} a_{jm}^\dagger |0\rangle, \tag{102}$$

and the complete set is generated by distributing the N particles in all possible ways throughout the basic one-particle states constituting the P-space. This is a very efficient representation. A single $|SD\rangle$ requires only one computer word (32 or 64 bits) and in memory a $|SD\rangle$ with N particles is given by

$$|SD\rangle \longrightarrow (\underbrace{00111101010\cdots}_{N1's}), \tag{103}$$

where each 0 and 1 corresponds to an m-orbit in the valence P-space. Occupied orbits have a 1 and empty orbits a 0. Furthermore, all important calculations can be handled in Boolean algebra which is very efficient on modern computers. The action of operators of the form $a_\alpha^\dagger a_\beta$ or $a_\alpha^\dagger a_\beta^\dagger a_\gamma a_\delta$ acting on a $|SD\rangle$ is easy to perform.

The *m*-scheme allows also for a straightforward definition of many-body operators such as one-, two- and three-particle operators

$$a_\alpha^\dagger a_\beta, \tag{104}$$

$$a_{\alpha_1}^\dagger a_{\alpha_2}^\dagger a_{\beta_1} a_{\beta_2}, \tag{105}$$

$$a_{\alpha_1}^\dagger a_{\alpha_2}^\dagger a_{\alpha_3}^\dagger a_{\beta_1} a_{\beta_2} a_{\beta_3}, \tag{106}$$

respectively, or generalized seniority operators. The seniority operators can be very useful in preparing a starting vector for the Lanczos iteration process. This option is fully implemented in our codes.

The generalized seniority operators [86] can then be written as

$$S^\dagger = \sum_j \frac{1}{\sqrt{2j+1}} C_j \sum_{m \geq 0} (-1)^{j-m} a_{jm}^\dagger a_{j-m}^\dagger \tag{107}$$

for seniority zero,

$$D_{JM}^\dagger = \sum_{j \leq j', m, m'} (1 + \delta_{j,j'})^{-1/2} \beta_{j,j'} \langle jmj'm' | JM \rangle a_{jm}^\dagger a_{j'm'}^\dagger \tag{108}$$

for seniority two. The coefficients C_j and $\beta_{jj'}$ can be obtained from the chosen two-particle system such as the ^{130}Sn ground state and the excited states, respectively. We can also define a seniority four operator

$$G(n_1, j_1, n_2, j_2; J, M) = \{D_{n_1,j_1}^\dagger D_{n_2,j_2}^\dagger\}_{J.M=0}$$
$$= \sum_{\nu_1...\nu_4} g_{\nu_1...\nu_4}^{JM} a_{\nu_1}^\dagger a_{\nu_2}^\dagger a_{\nu_3}^\dagger a_{\nu_4}^\dagger \tag{109}$$

and a seniority six operator

$$I(n_1, j_1, (n_2, j_2, n_3, j_3)j_{23}; J, M) = \{D_{n_1,j_1} G(n_2, j_2, n_3, j_3; j_{23})\}_{J,M=0}$$
$$= \sum_{\nu_1...\nu_6} g_{\nu_1...\nu_6}^{JM} a_{\nu_1}^\dagger a_{\nu_2}^\dagger a_{\nu_3}^\dagger a_{\nu_4}^\dagger a_{\nu_5}^\dagger a_{\nu_6}^\dagger. \tag{110}$$

Finally, our shell-model code allows also for the inclusion of effective and real three-body interactions. Results from such calculations will be discussed in Section 7.

4.2. The Lanczos iteration process

At present our basic approach to finding solutions to Eq. (101) is the Lanczos algorithm. This method was already applied to nuclear physics problems by Whitehead et al. in 1977. In a review article [67] they describe the technique in detail. For the present discussion we outline the basic elements of the method.

1. We choose an initial Lanczos vector $|lanc_0\rangle$ as the 0th order approximation to the lowest eigenvector in Eq. (101). Our experience is that any reasonable choice is acceptable as long as the vector does not have special properties such as good angular momentum. That would usually terminate the iteration process at too early a stage.

2. The next step involves generating a new vector through the process $|\text{new}_{p+1}\rangle = H|\text{lanc}_p\rangle$. Throughout this process we construct the energy matrix elements of H in this Lanczos basis. First, the diagonal matrix elements of H are then obtained by

$$\langle \text{lanc}_p|H|\text{lanc}_p\rangle = \langle \text{lanc}_p|\text{new}_{p+1}\rangle. \tag{111}$$

3. The new vector $|\text{new}_{p+1}\rangle$ is then orthogonalized to all previously calculated Lanczos vectors

$$|\text{new}'_{p+1}\rangle = |\text{new}_{p+1}\rangle - |\text{lanc}_p\rangle \cdot \langle \text{lanc}_p|\text{new}_{p+1}\rangle$$

$$- \sum_{q=0}^{p-1} |\text{lanc}_q\rangle \cdot \langle \text{lanc}_q|\text{new}_{p+1}\rangle, \tag{112}$$

and finally normalized

$$|\text{lanc}_{p+1}\rangle = \frac{1}{\sqrt{\langle \text{new}'_{p+1}|\text{new}'_{p+1}\rangle}}|\text{new}'_{p+1}\rangle, \tag{113}$$

to produce a new Lanczos vector.

4. The off-diagonal matrix elements of H are calculated by

$$\langle \text{lanc}_{p+1}|H|\text{lanc}_p\rangle = \langle \text{new}'_{p+1}|\text{new}'_{p+1}\rangle, \tag{114}$$

and all others are zero.

5. After n iterations we have an energy matrix of the form

$$\begin{Bmatrix} H_{0,0} & H_{0,1} & 0 & \cdots & 0 \\ H_{0,1} & H_{1,1} & H_{1,2} & \cdots & 0 \\ 0 & H_{2,1} & H_{2,2} & \cdots & 0 \\ \vdots & \vdots & \vdots & \vdots & H_{p-1,p} \\ 0 & 0 & 0 & H_{p,p-1} & H_{p,p} \end{Bmatrix} \tag{115}$$

as the pth approximation to the eigenvalue problem in Eq. (101). The number p is a reasonably small number and we can diagonalize the matrix by standard methods to obtain eigenvalues and eigenvectors which are linear combinations of the Lanczos vectors.

6. This process is repeated until a suitable convergence criterium has been reached.

In this method each Lanczos vector is a linear combination of the basic $|SD\rangle$ with dimension n. For $n \approx 10^6$–10^8, as in our case of interest. Here is one of the important difficulties associated with the Lanczos method. Large disk storage is needed when the number of Lanczos vector exceeds ≈ 100. Another difficulty is found in the calculation of $|\text{new}_{p+1}\rangle = H|\text{lanc}_p\rangle$ when $n > 10^6$.

One important objection found in the computer literature [87] to the Lanczos method is its slow convergence. This is also our experience so far and means that a large number of Lanczos vectors have to be calculated and stored in order to obtain convergence. One improvement which we have implemented is to terminate the Lanczos process earlier, diagonalize the energy matrix and choose some of the lowest thus obtained eigenvectors

as a starting point for a new Lanczos iteration. This modifies the energy matrix in Eq. (115) slightly, since the matrix will not be tri-diagonal any more. It reduces the disk storage requirement, but the convergence problem is left. A possible way out here is the Davidson–Liu method.

4.3. The Davidson–Liu method

We outline the basic elements of this technique and refer to the literature [87] for details. The first important improvement to the Lanczos process given in Eqs. (111) and (115) is to start with several orthogonalized and normalized initial vectors and the second difference is the way new additional vectors are chosen. The method can be viewed as an improvement of the Lanczos technique and can be described in the following steps:

1. Choose a (small) set of start vectors $|x_k^{(0)}\rangle$, $k = 1, \ldots, K$.
2. K new vectors are generated through the process $|\mathrm{new}_k^{(0)}\rangle = H|x_k^{(0)}\rangle$.
3. The matrix elements of H are again obtained by

$$\langle x_p^{(0)}|H|x_q^{(0)}\rangle = \langle x_p^{(0)}|\mathrm{new}_q^{(0)}\rangle, \tag{116}$$

   and the matrix H is no longer tri-diagonal. H is diagonalized within the set of states $|x_k^{(0)}\rangle$, $k = 1, \ldots, K$ and K eigenvalues and corresponding eigenstates are obtained as the 0th approximation to the lowest true eigenstates of Eq. (101) in the form

$$|x_p^{(1)}\rangle = \sum_{q=1}^{K} a_{q,p}|x_q^{(0)}\rangle = \sum_{\nu=1}^{n} C_{\nu,p}^{(1)}|\mathrm{SD}_\nu\rangle. \tag{117}$$

   The vectors $|x_p^{(1)}\rangle$ now constitute the basis for a new iteration.
4. New correction vectors are calculated through the steps

$$\begin{aligned}|r_p\rangle &= (H - \varepsilon_p^{(n)})|x_p^{(n)}\rangle = |h_p^{(n)}\rangle - \varepsilon_p^{(n)}|x_p^{(n)}\rangle,\\ |\delta_p\rangle &= (H_{\mathrm{diag}} - \varepsilon_p^{(n)})^{-1}|r_p\rangle.\end{aligned} \tag{118}$$

   Then new additional vectors are obtained by orthogonalizing to all previous vectors, and finally normalized

$$\begin{aligned}|x_{k'+p}^{(n)}\rangle = \sqrt{\frac{1}{\mathrm{norm}}}\Bigg\{&|\delta_p\rangle - \sum_{q=1}^{K}|x_q^{(n)}\rangle \cdot \langle x_q^{(n)}|\delta_p\rangle \\ &- \sum_{q<p}^{K}|x_{k'+q}^{(n)}\rangle \cdot \langle x_{K+q}^{(n)}|\delta_p\rangle\Bigg\},\end{aligned} \tag{119}$$

   witk $k' = 1, \ldots, K' \leq K$. Thus up to K new vectors may be generated through one iteration. Then the diagonalization process in Eqs. (116) and (117) is repeated and a new iteration to the true eigenvectors is obtained.
5. Again this process may be repeated until some convergence criterium has been reached.

4.4. Break-up of the doubly-magic ^{100}Sn core

Doubly-magic nuclei and their immediate neighbors are of great interest as they provide direct information on the basic shell structure that is ultimately responsible for most nuclear properties. Lying at the proton drip line and being the heaviest particle-stable, self-conjugate nucleus, ^{100}Sn is particularly relevant in this context. An important property of this nucleus is the degree of rigidity of its spherical shape which is reflected in the excitation energy of the lowest 2^+ state and in the associated $B(E2; 2^+ \rightarrow 0^+)$ transition rate. The main component of the wave function of this level in a microscopic description is presumably an isoscalar mixture of proton and neutron $2d_{5/2}1g_{9/2}^{-1}$ excitations across the $N = Z = 50$ shell gaps. This state is at present not known experimentally and its observation may well require the availability of intense exotic beams. Some guidance about its excitation energy can perhaps come from other doubly-magic nuclei. In the $N = Z = 28$ doubly-magic nucleus, the first 2^+ state is located rather low, at 2.7 MeV. In contrast, the 2^+ levels in ^{132}Sn and ^{208}Pb are much higher in excitation energy, 4.0 and 4.1 MeV, respectively, and in the latter nucleus the size of the shell gaps can also be appreciated from the fact that this state is not even the lowest excitation, but instead lies above a 3^- (octupole) vibrational state.

In order to estimate the position of the 2^+ state in ^{100}Sn, both proton and neutron shell gaps have to be known. The energy splittings of the relevant single-particle orbitals in the other heavy doubly-magic nuclei are comparable. The neutron $2p_{3/2}$ and $1f_{7/2}$ orbitals are 6.4 MeV apart in ^{56}Ni, while the splittings between the $2f_{7/2}$ and $1h_{11/2}$ levels in ^{132}Sn and $2g_{9/2}$ and $1i_{13/2}$ states in ^{208}Pb are 4.9 and 5.1 MeV, respectively. Here, the splitting between the $2d_{5/2}$ and $1g_{9/2}$ neutron orbits will be shown to be of the order of 6 MeV as in the ^{56}Ni case. However, a sizable proton–neutron interaction could, as in ^{56}Ni, decrease the excitation energy and increase the transition rate for the lowest 2^+ state in ^{100}Sn. Such an interaction is expected to be especially strong in $N = Z$ nuclei, where protons and neutrons occupy the same single-particle orbitals, which results in a large spatial overlap of their wave functions. Nuclei near ^{100}Sn were studied using the ^{58}Ni + ^{50}Cr reaction. A ^{58}Ni beam of 225 MeV was provided by the ATLAS superconducting linear accelerator at Argonne National Laboratory. The effective two-body interactions were applied in a shell-model space spanning $2s_{1/2}$, $1d_{5/2}$, $1d_{3/2}$, $0g_{7/2}$ and $0h_{11/2}$ neutron, and $0g_{9/2}$ and $1p_{1/2}$ proton single-particle orbitals [88]. The model space is shown in Fig. 13. In this model space, ^{99}Cd has one neutron and 10 protons outside the core. The results of the calculation, denoted as SMH, are compared with the experimental levels in Fig. 14. The calculation favors a $J^\pi = 5/2^+$ assignment for the ground state, in agreement with the systematics of odd-A, $N = 51$ isotones. The wave functions of the states with $J^\pi = 5/2^+$, $9/2^+$, $13/2^+$, $17/2^+$, $19/2_1^+$ and $21/2_1^+$ all have main configurations where the valence neutron is in the $d_{5/2}$ orbit, while the $7/2^+$, $11/2^+$, $15/2^+$, $19/2_2^+$, $21/2_2^+$ and $23/2^+$ levels are associated with the predominant occupation of the $g_{7/2}$ orbit. For all these states, the two proton holes always remain assigned to the $g_{9/2}$ orbit. The lowest $7/2^+$ states in $N = 51$ isotones from ^{91}Zr to ^{97}Pd are well reproduced by using the experimental $g_{7/2}$ single-particle energy from zirconium [88], but in ^{99}Cd this state was calculated 250 keV too low. Therefore, the single-particle energy of the neutron $g_{7/2}$ orbit, relative to the ^{88}Sr, core was increased from 2.63 to 2.89 MeV in order to reproduce the experimental excitation energy of the
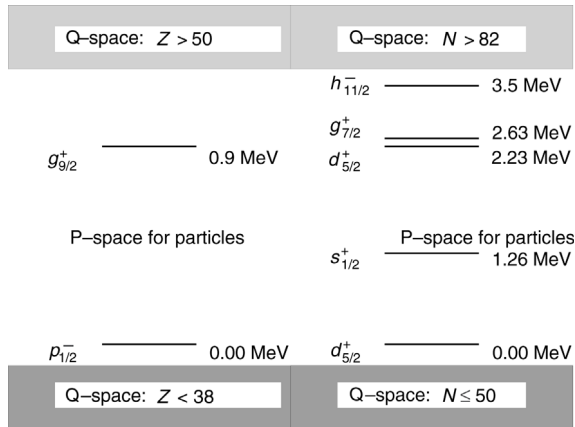
Fig. 13. Possible shell-model space for nuclei around $A \sim 100$ using ^{88}Sr as closed-shell core with the neutron orbitals $2s_{1/2}$, $1d_{5/2}$, $1d_{3/2}$, $0g_{7/2}$ and $0h_{11/2}$ and proton single-particle orbitals $0g_{9/2}$ and $1p_{1/2}$ defining the model space. Their respective single-particle energies are displayed as well.

$7/2^+$ state. This yielded excellent agreement between calculations and experiment up to the $J^\pi = 23/2^+$ state, see for example Fig. 14, the highest spin that can be generated in this model space for positive-parity states in ^{99}Cd. The description of higher-spin states requires the excitation of one or more $g_{9/2}$ particles across the $N, Z = 50$ shell gaps, an excitation similar to that responsible for the first 2^+ and higher-lying states in ^{100}Sn.

To study the high-spin states, another shell-model calculation was performed using this time ^{78}Sr as a closed shell core. The results are denoted as SMG in Fig. 14. The same model space as in the previous calculation was employed except for the $h_{11/2}$ neutron orbit which was replaced by the $g_{9/2}$ one. (Since this $h_{11/2}$ state lies at a relatively high excitation energy, its contribution to the positive-parity states is small.) Due to limitations in computing time, only up to two neutrons were allowed to leave the $g_{9/2}$ orbit. (Note that the $g_{9/2}$ orbit lies below the $N = 50$ shell gap, while all other neutron orbitals in this model space lie above this gap.) Opening of the $N = 50$ shell only is justified since a neutron hole in the $g_{9/2}$ orbit, together with an existing proton hole, produces a very attractive 9^+ proton–neutron coupling. Similarly, the excited neutron, together with the one already occupying the same orbit, produces a 0^+ neutron pair with a strong attractive interaction. Opening the $Z = 50$ shell would not result in such a strong attraction. Single-particle energies with respect to the ^{78}Sr core are not known and were kept the same as in [88] for the ^{88}Sr core. The energy of the $g_{9/2}$ orbit was placed 5.0 MeV below that of the $d_{5/2}$ one. The wave functions of the states below the $25/2^+$ level are very similar to those obtained in the SMH calculation (which assumed that the $g_{9/2}$ neutron orbit is completely filled), except for the two $19/2^+$ levels, where the occupation numbers are reversed for the $d_{5/2}$ and $g_{7/2}$ orbits. The $25/2^+$ level and the higher-lying states have 9 neutrons in the $g_{9/2}$ orbit with the remaining neutron pair almost evenly distributed over the $d_{5/2}$ and $g_{7/2}$ orbits. These states represent the break-up of the doubly-magic ^{100}Sn core. Thus, the excitation energy of the states with $J^\pi \geq 25/2^+$ is sensitive to the position of the $g_{9/2}$ orbit.

Fig. 14. Experimental (EXP) and calculated (SMH, SMG) level schemes for ^{99}Cd. The widths of the arrows are proportional to the intensities of the γ rays observed in the experiment. As discussed in the text, the $J = 25/2^+$ and higher-lying states require excitations across the ^{100}Sn core.

By fitting this single particle energy to 5.0 MeV we, therefore, indirectly deduced the size of the $N = 50$ shell gap to be 6.5 MeV as defined by $2BE(^{100}Sn)-BE(^{99}Sn)-BE(^{101}Sn)$, where BE stands for binding energy. This value agrees well with earlier predictions from

Hartree–Fock calculations by Leander et al. [89], as well as a single-particle energy parametrization by Duflo and Zuker [90] and an extrapolation by Grawe et al. [91]. To investigate the effect of the truncation of the model space on the deduced size of the $N = 50$ shell gap we calculated the excitation energy of the $J^\pi = 25/2^+$ state in ^{99}Cd using two different model spaces. In the first one, we allowed up to four neutrons to leave the $g_{9/2}$ orbit and the second truncation scheme restricted the valence particles to only two in each active orbit. Different truncations of the model space required adjustments of the $g_{9/2}$ single-particle energy to reproduce the experimental excitation energy of the $25/2^+$ level, but when this was achieved the size of the $N = 50$ shell gap remained within 0.5 MeV of the above value. This illustrates a relative insensitivity of our inferred result to the truncation procedure used in the shell-model calculation.

Calculations using the same single-particle energies and matrix elements were also performed for ^{101}In, which has one proton hole and two neutrons outside the $N = Z = 50$ doubly-closed shells. Again, the results, labeled as SMH and SMG, are in very good agreement with the experimental level scheme in Fig. 15. In these calculations, the proton hole remains in the $g_{9/2}$ orbital and a $J^\pi = 9/2^+$ assignment follows for the ground state. This is in agreement with the systematics of odd-A In isotopes. The valence neutron pair is distributed over the $d_{5/2}$ and $g_{7/2}$ orbits for the ground state, while it occupies predominantly the $d_{5/2}$ state for the $13/2^+$ level. One neutron is promoted to the $g_{7/2}$ and $h_{11/2}$ orbitals to generate the $17/2^+$, $19/2^+$, $21/2^+$ positive-parity, and $23/2^-$, $25/2^-$ negative-parity states, respectively. The large separation between the $19/2^+$ and $21/2^+$ states, which are associated with the same dominant configuration, is attributed to the strong repulsion between the aligned $g_{9/2}$ proton hole and the $g_{7/2}$ neutron. Note that the $\pi g_{9/2} \nu h_{11/2}$ matrix elements used to calculate the negative-parity states in ^{102}In described in [92] were adopted here as well. The maximum spin that can be reached with the $\pi g_{9/2} \nu d_{5/2} g_{7/2}$ configuration is 21/2. Excitation of one or more particles across the $N, Z = 50$ shell gaps is again needed to account for the positive-parity states of higher spin. Thus, the $23/2^+$ level is the lowest-lying core-excited state in ^{101}In. The calculated energy gap of 2941 keV between the $23/2^+$ and $19/2^+$ states is in excellent agreement with the experimental value of 2924 keV. Experimentally known lowest lying core excited states were also calculated in the nuclei ^{98}Ag [93] and ^{96}Pd [94] using the SMG model space. Their excitation energies were reproduced to better than 100 keV. It is more difficult to identify core excited states in nuclei near ^{90}Zr, because in those nuclei high-spin states can be easily reached by promoting a pair of protons from the low-spin $p_{1/2}$ orbit into the empty $g_{9/2}$ orbit.

The interactions used in these SMH and SMG calculations were also applied to a shell-model calculation of the lowest-lying levels in ^{101}Sn. Both SMH and SMG calculations favor $J^\pi = 5/2^+$ quantum numbers for the ground state, while the $7/2^+$ state lies only ~100 keV above. This is in excellent agreement with the extrapolated energy deduced from the systematics of odd-A Sn isotopes down to ^{103}Sn [95].

It is also worth pointing out that the level schemes of ^{99}Cd and ^{101}In closely mirror those of their analogs in the ^{56}Ni region, i.e., ^{55}Fe [96] and ^{57}Co [97]. In particular, the lowest-lying core-excited states have almost identical excitation energies. This observation, together with the deduced $N = 50$ shell gap, again points to a large similarity between the two heaviest self-conjugated doubly-magic nuclei and one may conclude that the lowest
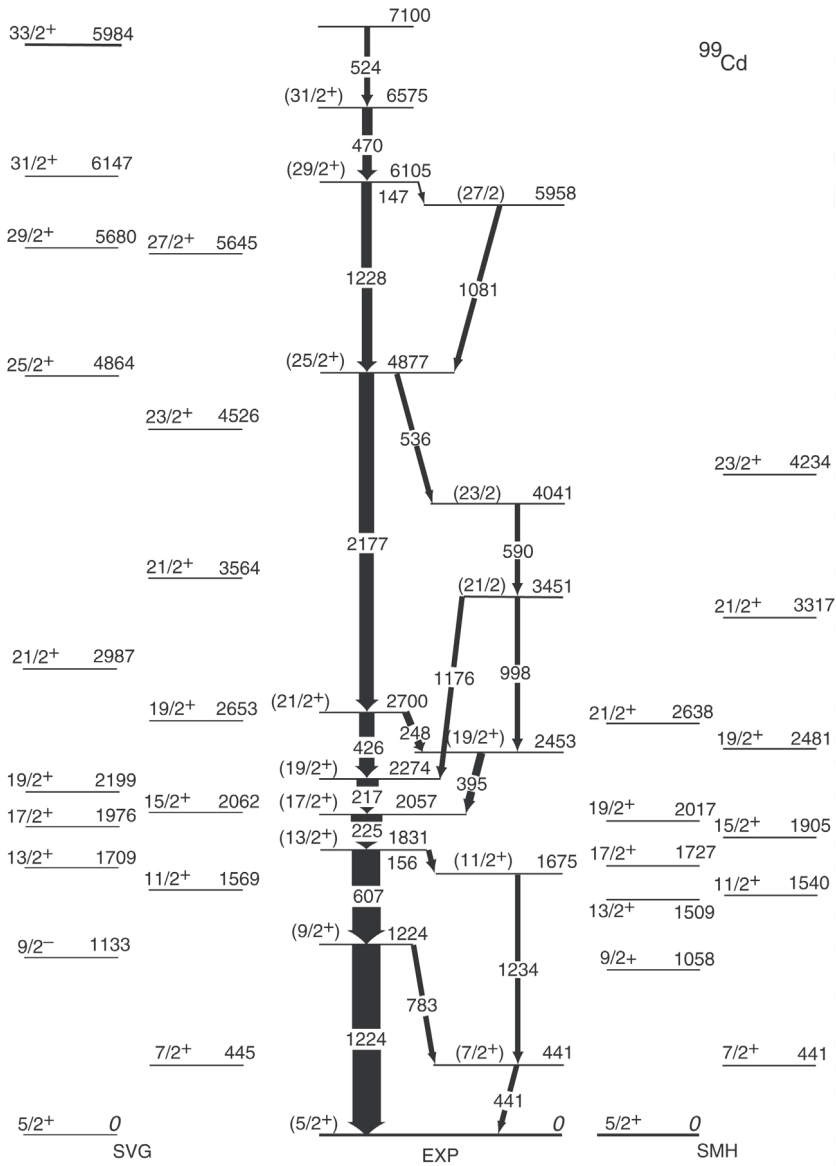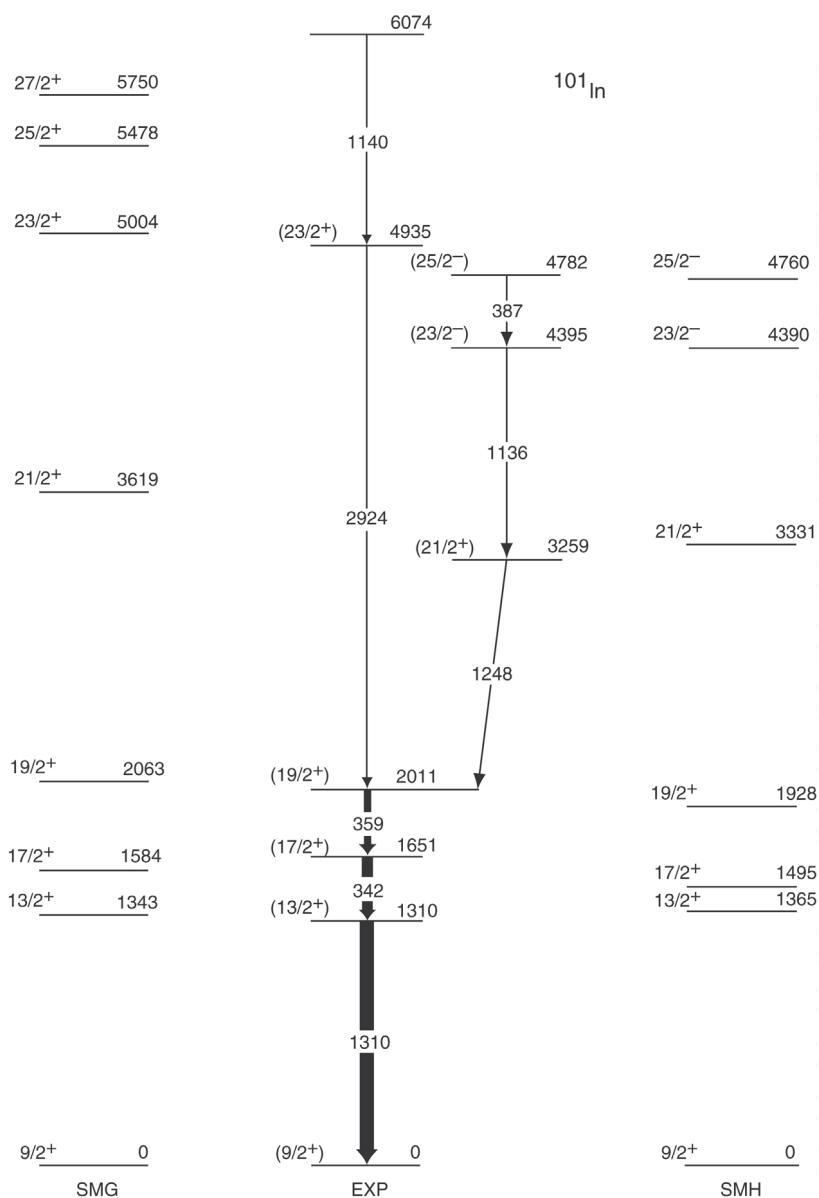
Fig. 15. Experimental (EXP) and calculated (SMH, SMG) level schemes for ^{101}In. The widths of the arrows are proportional to the intensities of the γ rays observed in the experiment. The $(J = 23/2^+)$ state requires excitations across the ^{100}Sn core.

2^+ states in ^{56}Ni and ^{100}Sn would have closely related excitation energies if the sizes of the $Z = 28$ and $Z = 50$ shell gaps were also similar.
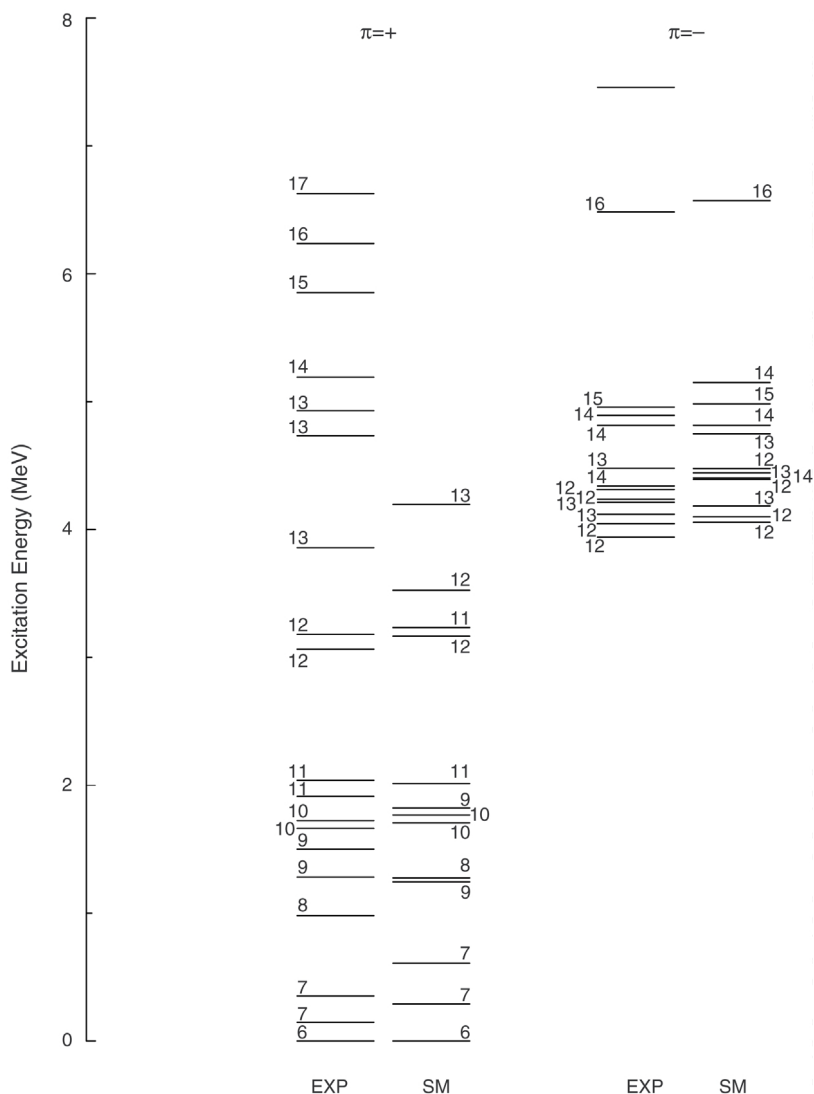
Fig. 16. Comparison of experimental and calculated levels in ^{102}In.

4.5. ^{100}Sn core excitations in ^{102}In

In the above model space ^{102}In has three valence neutrons and 11 valence protons, which is equivalent to one proton hole in the doubly magic ^{100}Sn core. In all calculated levels shown in Fig. 16 this proton hole remains in the $g_{9/2}$ orbit. Therefore, the only proton contribution to the calculated level scheme of ^{102}In is through proton–neutron pairing. The calculation favors $J^\pi = 6^+$ for the ground state. The three valence neutrons are mainly in

the $d_{5/2}$ orbit in this state, while about 40% of the wave function amplitude comes from the contribution of the $g_{7/2}$ orbit. All other orbits have an insignificant contribution to the wave function of the ground state. Surprisingly, all levels up to the $J^\pi = 10_2^+$ level have a very similar wave function configuration in the calculation. The 10_2^+ level is the lowest observed level for which the $d_{5/2}$ and $g_{7/2}$ orbits switch their occupation numbers. The larger wave function difference results in lower mixing between the 10_1^+ and 10_2^+ levels. This in turn leads to two close lying 10^+ states, correctly predicted by the calculation. However, all other non-yrast states are calculated too high and we expect that the $g_{7/2}$ orbit has a larger than calculated contribution to their wave functions. This is especially true for the 11_2^+ state that is calculated more than 1 MeV too high. We may conclude that the interaction used in the calculation gives a too strong attraction between the $g_{9/2}$ protons and the $g_{7/2}$ neutrons.

The very nice one-to-one correspondence between experimental and calculated positive parity states ends with the 13_1^+ state, which is the highest spin that can be reached by coupling one proton hole in the $g_{9/2}$ orbit with three neutrons in $d_{5/2}$ and $g_{7/2}$ orbits. The wave function of this state is therefore $\pi(g_{9/2})^{-1}\nu d_{5/2}(g_{7/2})^2$.

The experimental positive parity levels above the 3858 keV level do not have calculated counterparts. The only possibility to reach such spins and parities within the model space used in the calculation is to promote a neutron pair to the $h_{11/2}$ orbit. However, even after changing the $\pi g_{9/2}\nu h_{11/2}$ effective interaction to reproduce the negative parity states the $J^\pi = 13_2^+$ to 17^+ levels were calculated much higher in energy than the experimental ones. These states must, therefore, be due to excitations across the doubly closed $N = Z = 50$ shell. Most likely they are due to the excitation of a neutron from the $g_{9/2}$ orbit just below the $N = 50$ shell gap to the $d_{5/2}$ orbit just above the gap, since this produces the very attractive $(\pi g_{9/2}^{-1}\nu g_{9/2}^{-1})^{9+}$ coupling combined with four neutron particle states like the $J^\pi = 6^+$ to 8^+ and 10^+ states in ^{104}Sn.

4.6. Tin isotopes for $100 \leq A \leq 132$

In Fig. 17 we present the model space and pertinent single-particle energies for a shell-model space for neutron valence holes using ^{132}Sn as closed shell core. In Table 2 we display selected states. As can be seen, the well-known near constant 0^+–2^+ spacing is well reproduced. all the way down to ^{116}Sn. Also the additional calculated states are in very good agreement with experiment. However more detailed analysis of the results close to ^{116}Sn indicates that our effective two-particle interaction has difficulties in reproducing the shell closure which is believed to occur in this region. The increase of the 0^+–2^+ splitting is not as sharp as that found experimentally, even if the phenomenon is rather weak in the case of Sn. We have observed a similar feature around ^{48}Ca [16] which is generally agreed to be a good closed shell nucleus. There the deviation between theory and experiment is severe. Preliminary analysis indicates that our effective interaction may be slightly too attractive when the two particles occupy different single-particle orbits. This may be related to the radial wave functions which in our calculation are chosen to be harmonic oscillator functions. Further analysis of these spectra can be found in [98, 99].
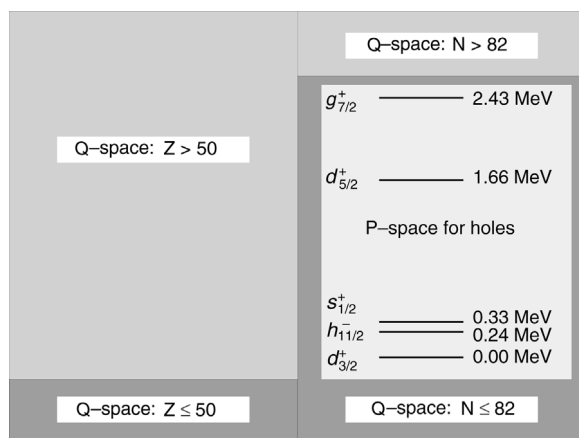
Fig. 17. Shell-model space for tin isotopes for $100 \leq A \leq 132$. The valence neutrons are hole states.

Table 2
Exitation spectra for the heavy Sn isotopes

^{130}Sn				^{128}Sn			
J^π	Exp.	J^π	Theory	J^π	Exp.	J^π	Theory
(2^+)	1.22	2^+	1.46	(2^+)	1.17	2^+	1.28
(4^+)	2.00	4^+	2.39	(4^+)	2.00	4^+	2.18
(6^+)	2.26	6^+	2.64	(6^+)	2.38	6^+	2.53
^{126}Sn				^{124}Sn			
J^π	Exp.	J^π	Theory	J^π	Exp.	J^π	Theory
2^+	1.14	2^+	1.21	2^+	1.13	2^+	1.17
4^+	2.05	4^+	2.21	4^+	2.10	4^+	2.26
		6^+	2.61			6^+	2.70
^{122}Sn				^{120}Sn			
J^π	Exp.	J^π	Theory	J^π	Exp.	J^π	Theory
2^+	1.14	2^+	1.15	2^+	1.17	2^+	1.14
4^+	2.14	4^+	2.30	4^+	2.19	4^+	2.30
6^+	2.56	6^+	2.78			6^+	2.86
^{118}Sn				^{116}Sn			
J^π	Exp.	J^π	Theory	J^π	Exp.	J^π	Theory
2^+	1.22	2^+	1.15	2^+	1.30	2^+	1.17

It is also instructive to study the degree of pairing in these systems. We calculate the squared overlaps between the constructed generalized seniority states in Eqs. (107) and (108) and our shell model states through

$$\left| \begin{array}{ll} (v=0) & |\langle ^A\mathrm{Sn(SM)}; 0^+ | (S^\dagger)^{\frac{n}{2}} |\tilde{0}\rangle|^2, \\ (v=2) & |\langle ^A\mathrm{Sn(SM)}; J_i | D_{JM}^\dagger (S^\dagger)^{\frac{n}{2}-1} |\tilde{0}\rangle|^2 \end{array} \right| . \tag{120}$$

Table 3
Seniority $v = 0$ overlap $|\langle^A \text{Sn}; 0^+|(S^\dagger)^{\frac{n}{2}}|\tilde{0}\rangle|^2$ and the seniority $v = 2$ overlaps $|\langle^A \text{Sn}; J_f|D_{JM}^\dagger(S^\dagger)^{\frac{n}{2}-1}|\tilde{0}\rangle|^2$ for the lowest-lying eigenstates of $^{128-120}$Sn

	$A = 128$	$A = 126$	$A = 124$	$A = 122$	$A = 120$
0_1^+	0.96	0.92	0.87	0.83	0.79
2_1^+	0.92	0.89	0.84	0.79	0.74
4_1^+	0.73	0.66	0.44	0.13	0.00
4_2^+	0.13	0.18	0.39	0.66	0.74
6_1^+	0.81	0.85	0.83	0.79	0.64

The vacuum state $|\tilde{0}\rangle$ is the ^{132}Sn-core and n is the number of valence particles. These quantities tell to what extent the shell model states satisfy the pairing picture, or in other words, how well generalized seniority is conserved as a quantum number.

The squared overlaps are tabulated in Table 3, and vary generally from 0.95 to 0.75. As the number of valence particles increases the squared overlaps are gradually decreasing. The overlaps involving the 4^+ states show a fragmentation. In ^{128}Sn, the 4_1^+ (SM) state is mainly a seniority $v = 2$ state. As approaching the middle of the shell, the next state, 4_2^+, more and more takes over the structure of a seniority $v = 2$ state. The fragmentation of seniority over these two states can be understood from the fact that they are rather close in energy and therefore may have mixed structure.

4.7. Tin isotopes above $A = 132$

For tin isotopes above $A = 132$ calculations were performed for isotopes with $134 \leq A \leq 139$ taking $Z = 50, N = 82$ as core. The active P-space for particles includes the 1f$_{7/2}$, 1p$_{3/2}$, 2p$_{1/2}$, 0h$_{9/2}$, 1f$_{5/2}$ and 0i$_{13/2}$ particle orbits, The single-particle energies $\varepsilon(f_{7/2}^-) = 0.00$ MeV, $\varepsilon(p_{3/2}^-) = 0.8537$ MeV, $\varepsilon(p_{1/2}^-) = 1.5609$ MeV, $\varepsilon(f_{5/2}^-) = 1.6557$ MeV $\varepsilon(h_{9/2}^-) = 2.0046$ MeV and $\varepsilon(i_{13/2}^+) = 2.81$ MeV are extracted from [100]. The obtained results are presented in Table 4 for isotopes with even values of A and in Table 5 for isotopes with odd A.

There are however no experimental data for the $A > 134$ tin isotopes available at the present time. We therefore cannot make conclusions on how good our effective interaction is for this mass region. A more detailed analysis of these results can be found in [101].

4.8. Light antimony isotopes

The nucleus ^{105}Sb was produced in the reaction ^{50}Cr(^{58}Ni, 1p2n) at a beam energy of 225 MeV with a 2.1 mg/cm^2 thick target. The experiment was performed with the GAMMASPHERE Ge-detector array [102] at the ATLAS accelerator at Argonne National Laboratory. The experimental setup consisted of 78 Ge detectors, 95 CsI scintillators known as Microball [103] for light charged particle detection, and the newly developed neutron shell.

The calculation favors a $J^\pi = 5/2^+$ assignment (see Fig. 18) for the ground state in agreement with the suggestion from the proton decay data. In this state the valence proton is mainly in the d$_{5/2}$ orbit and the two neutron pairs are almost evenly distributed

Table 4
Low-lying states for ^{134}Sn, ^{136}Sn and ^{138}Sn. The energy eigenvalues are sorted according to the angular momentum assignment

^{134}Sn		^{136}Sn		^{138}Sn	
J_i^π	Theory	J_i^π	Theory	J_i^π	Theory
0_1^+	0.00	0_1^+	0.00	0_1^+	0.00
0_2^+	2.28	0_2^+	1.86	0_2^+	1.52
0_3^+	2.97	0_3^+	1.92	0_3^+	1.78
		0_4^+	2.34	0_4^+	1.89
2_1^+	0.77	2_1^+	0.73	2_1^+	0.75
2_2^+	1.65	2_2^+	1.45	2_2^+	1.27
2_3^+	2.64	2_3^+	1.52	2_3^+	1.71
2_4^+	2.73	2_4^+	1.87	2_4^+	1.87
2_5^+	3.13	2_5^+	2.23	2_5^+	2.02
2_6^+	3.51	2_6^+	2.29	2_6^+	2.07
				2_6^+	2.15
4_1^+	1.11	4_1^+	1.15	4_1^+	1.34
4_2^+	1.94	4_2^+	1.32	4_2^+	1.50
4_3^+	2.67	4_3^+	1.76	4_3^+	1.80
4_4^+	2.88	4_4^+	1.98	4_4^+	1.87
4_5^+	3.25	4_5^+	2.07	4_5^+	2.02
4_6^+	3.74	4_6^+	2.37	4_6^+	2.07
				4_6^+	2.15
6_1^+	1.25	6_1^+	1.37	6_1^+	1.52
6_2^+	2.61	6_2^+	2.15	6_2^+	2.12
6_3^+	2.97	6_3^+	2.37		
6_4^+	3.63				
8_1^+	2.46	8_1^+	2.11		
3_1^-	3.56	3_1^-	3.49	3_1^-	3.42
5_1^-	3.91	5_1^-	3.76	5_1^-	3.53
7_1^-	4.00	7_1^-	3.85	9_1^-	3.68
9_1^-	4.04	9_1^-	3.89	7_1^-	3.68

over the $d_{5/2}$ and $g_{7/2}$ neutron orbits. The situation is very similar in the $9/2^+$ and $13/2^+$ states, while the $\nu d_{5/2}^3 g_{7/2}^1$ configuration exhausts the largest parts of the wave functions of the $15/2^+$ and $17/2^+$ states. The neutron part of the wave function of the $19/2^+$ state is almost identical to the $17/2^+$ state. However, since $17/2^+$ is the maximum spin for the $\pi d_{5/2}^1 \nu d_{5/2}^1 g_{7/2}^1$ configuration, the odd proton resides almost exclusively in the $g_{7/2}$ orbit in the $19/2^+$ state. The $19/2^+$ state is therefore the lowest lying of the observed states, in which the $\pi g_{7/2}$ orbit has a significant contribution to the wave function. This pattern

Table 5
Low-lying states for ^{135}Sn and ^{137}Sn

^{135}Sn		^{137}Sn	
J_i^{π}	Theory	J_i^{π}	Theory
$7/2_1^-$	0.00	$7/2_1^-$	0.00
$5/2_1^-$	0.30	$5/2_1^-$	0.29
$3/2_1^-$	0.41	$3/2_1^-$	0.37
$3/2_2^-$	0.64	$3/2_2^-$	0.60
$11/2_1^-$	0.74	$1/2_1^-$	0.72
$9/2_1^-$	0.86	$11/2_1^-$	0.75
$15/2_1^-$	1.09	$9/2_1^-$	0.77
$9/2_2^-$	1.16	$5/2_2^-$	0.81
$9/2_3^-$	1.19	$9/2_2^-$	0.88
$1/2_1^-$	1.21	$7/2_2^-$	0.95
$7/2_2^-$	1.27	$5/2_3^-$	1.04
$5/2_2^-$	1.37	$1/2_2^-$	1.05
$3/2_3^-$	1.40	$9/2_3^-$	1.09
$7/2_3^-$	1.40	$3/2_3^-$	1.10
$5/2_3^-$	1.52	$7/2_3^-$	1.11
$5/2_4^-$	1.59	$15/2_1^-$	1.26
$13/2_1^-$	1.70	$5/2_4^-$	1.29
$1/2_2^-$	1.72	$7/2_4^-$	1.30
$11/2_2^-$	1.73	$9/2_4^-$	1.37
$11/2_3^-$	1.77	$13/2_1^-$	1.38

repeats itself for the states with spins $21/2^+$, $23/2^+$, $25/2^+$ and $27/2^+$ in an alternating fashion with the state $21/2^+$ having a proton in the single-particle orbit $\pi d_{5/2}$. For proton degrees of freedom the $s_{1/2}$, $d_{3/2}$ and $h_{11/2}$ single-particle orbits give essentially negligible contributions to the wave functions and the energies of the excited states, as expected. For neutrons, although the single-particle distribution for a given state is also negligible, these orbits are important for a good description of the energy spectrum, as also demonstrated in large-scale shell-model calculations of tin isotopes [98]. The effective interaction employed here is the same as that employed in [98], with an in general good reproduction of the data.

We note here as well that the agreement with the experimentally proposed spin assignments is very good. The reason for such a good agreement is most likely that the wave functions of the states are dominated by neutronic degrees of freedom. The unbound proton is only a spectator while the well bound neutrons change orbits and alignment in transitions from high spin states.

The recently described spectra of ^{107}Sb show also low-lying $7/2^+$ and $11/2^+$ states, at approximately the same excitation energies as those shown in the theoretical calculation here. The γ-ray transitions feeding these two states in ^{105}Sb are as in ^{107}Sb expected to be much weaker than the main γ-ray cascade, which explains why these two states were not identified in the experiment. They are interesting since their wave functions contain mainly contributions from the $\pi g_{7/2}$ orbit that is poorly known near ^{100}Sn, but a more sensitive experiment is needed for their identification.
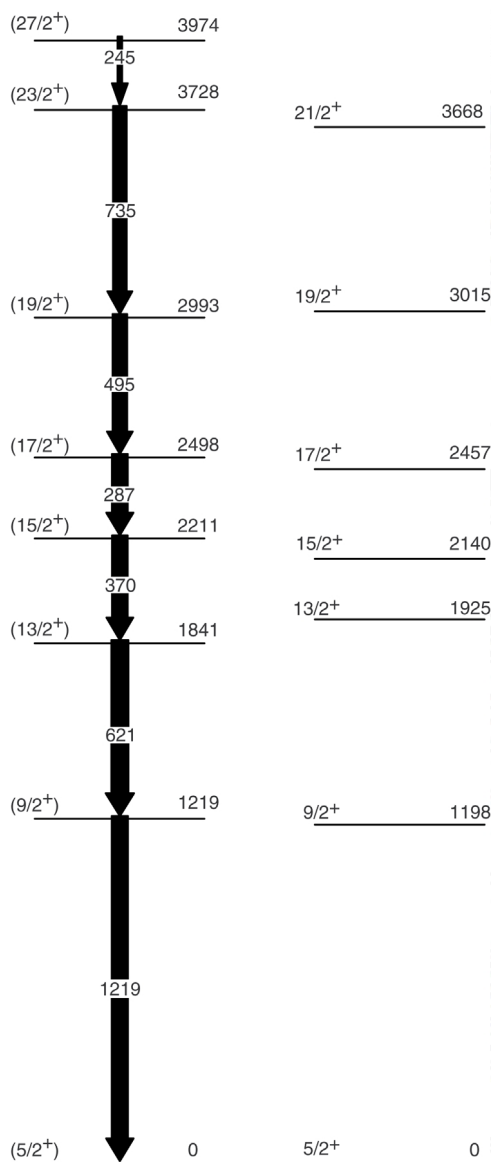
Fig. 18. Proposed level scheme for ^{105}Sb. Shell-model calculations are shown on the right hand side. The widths of the arrows are proportional to the intensity of the transitions.

4.9. Neutron-rich nuclei in the 1s0d–1p0f shells

Studies of extremely neutron-rich nuclei have revealed a number of intriguing new phenomena. Two sets of these nuclei that have received particular attention are those with

neutron number N in the vicinity of the 1s0d and $0f_{7/2}$ shell closures ($N \approx 20$ and $N \approx 28$). Experimental studies of neutron-rich Mg and Na isotopes indicate the onset of deformation, as well as the modification of the $N = 20$ shell gap for ^{32}Mg and nearby nuclei [104]. Inspired by the rich set of phenomena occurring near the $N = 20$ shell closure when $N \gg Z$, attention has been directed to nuclei near the $N = 28$ (sub)shell closure for a number of S and Ar isotopes [105, 106] where similar, but less dramatic, effects have been seen as well. In parallel with the experimental efforts, there have been several theoretical studies seeking to understand and, in some cases, predict properties of these unstable nuclei. Both mean-field [107, 108] and shell-model calculations [105, 106, 109–113] have been proposed. The latter require a severe truncation to achieve tractable model spaces, since the successful description of these nuclei involves active nucleons in both the 1s0d- and the 1p0f-shells. The natural basis for the problem is therefore the full 1s0d–1p0f space, which puts it out of reach of exact diagonalization on current hardware.[6]

Shell-model Monte Carlo (SMMC) methods [7, 114, 115] offer an alternative to direct diagonalization when the bases become very large. Though SMMC provides limited detailed spectroscopic information, it can predict, with good accuracy, overall nuclear properties such as masses, total strengths, strength distributions, and deformation, precisely those quantities probed by the recent experiments.

There is limited experimental information about the highly unstable, neutron-rich nuclei under consideration. In many cases only the mass, excitation energy of the first excited state, the $B(E2)$ to that state, and the β-decay rate is known, and not even all of this information is available in some cases. From the measured $B(E2)$, an estimate of the nuclear deformation parameter, β_2, has been obtained via the usual relation

$$\beta_2 = 4\pi \sqrt{B(E2; 0_{gs}^+ \rightarrow 2_1^+)/3ZR_0^2 e} \tag{121}$$

with $R_0 = 1.2A^{1/3}$ fm and $B(E2)$ given in e^2 fm^4.

Much of the interest in the region stems from the unexpectedly large values of the deduced β_2, results which suggest the onset of deformation and have led to speculations about the vanishing of the $N = 20$ and $N = 28$ shell gaps. The lowering in energy of the 2_1^+ state supports this interpretation. The most thoroughly studied case, and the one which most convincingly demonstrates these phenomena, is ^{32}Mg with its extremely large $B(E2) = 454 \pm 78$ e^2 fm^4 and corresponding $\beta_2 = 0.513$ [104]; however, a word of caution is necessary when deciding on the basis of this limited information that we are in the presence of well-deformed rotors: for ^{22}Mg, we would obtain $\beta_2 = 0.67$, even more spectacular, and for ^{12}C, $\beta_2 = 0.8$, well above the superdeformed bands.

Most of the measured observables can be calculated within the SMMC framework. It is well known that in *deformed* nuclei the total $B(E2)$ strength is almost saturated by the $0_{gs}^+ \rightarrow 2_1^+$ transition (typically 80% to 90% of the strength lies in this transition). Thus the total strength calculated by SMMC should only slightly overestimate the strength of the measured transition. In Table 6 the SMMC computed values of $B(E2, \text{total})$ are compared both to the experimental $B(E2; 0_{gs}^+ \rightarrow 2_1^+)$ values and to the values found in various

---

[6] For a treatment of the CoM problem, see [69].

Table 6
The computed and measured values of $B(E2)$ for the nuclei in this study using $e_p = 1.5$ and $e_n = 0.5$

	$B(E2; 0^+_{gs} \rightarrow 2^+_1)_{\text{Expt}}$	$B(E2, \text{total})_{\text{SMMC}}$	$B(E2; 0^+_{gs} \rightarrow 2^+_1)$
^{22}Mg	458 ± 183	334 ± 27	
^{30}Ne		303 ± 32	342 [111], 171 [118]
^{32}Mg	454 ± 78 [104]	494 ± 44	448 [111], 205 [118]
^{36}Ar	296.56 ± 28.3 [116]	174 ± 48	
^{40}S	334 ± 36 [105]	270 ± 66	398 [106], 390 [112]
^{42}S	397 ± 63 [105]	194 ± 64	372 [106], 465 [112]
^{42}Si		445 ± 62	260 [112]
^{44}S	314 ± 88 [106]	274 ± 68	271 [106], 390 [112]
^{44}Ti	610 ± 150 [117]	692 ± 63	
^{46}Ar	196 ± 39 [105]	369 ± 77	460 [105], 455 [112]

truncated shell-model calculations. Reasonable agreement with experimental data across the space is obtained when one chooses effective charges of $e_p = 1.5$ and $e_n = 0.5$. All of the theoretical calculations require excitations to the 1p0f-shell before reasonable values can be obtained. We note a general agreement among all calculations of the $B(E2)$ for ^{46}Ar, although they are typically larger than experimental data would suggest. We also note a somewhat lower value of the $B(E2)$ in this calculation as compared to experiment and other theoretical calculations in the case of ^{42}S. Table 7 gives selected occupation numbers for the nuclei considered. We first note a difficulty in extrapolating some of the occupations where the number of particles is nearly zero. This leads to a systematic error bar that we estimate at ± 0.2 for all occupations shown, while the statistical error bar is quoted in the table. The extrapolations for occupation numbers were principally linear. Table 7 shows that ^{22}Mg remains as an almost pure sd-shell nucleus, as expected. We also see that the protons in ^{30}Ne, ^{32}Mg, and ^{42}Si are almost entirely confined to the sd shell. This latter is a pleasing result in at least two regards. First, it shows that the interaction does not mix the two shells to an unrealistically large extent. Second, if spurious CoM contamination were a severe problem, we would expect to see a larger proton $0f_{7/2}$ population for these nuclei due to the $0d_{5/2}$–$0f_{7/2}$ "transition" mediated by the center-of-mass creation operator. The fact that there is little proton $f_{7/2}$ occupation for these nuclei confirms that the CoM contamination is under reasonable control. See [69] for further details. An interesting feature of Table 7 lies in the neutron occupations of the $N = 20$ nuclei (^{30}Ne and ^{32}Mg) and the $N = 28$ nuclei (^{42}Si, ^{44}S, and ^{46}Ar). The neutron occupations of the two $N = 20$ nuclei are quite similar, confirming the finding of Fukunishi et al. [111] and Poves and Retamosa [110] that the $N = 20$ shell gap is modified. In fact, the neutron $0f_{7/2}$ orbital contains approximately two particles before the $N = 20$ closure, thus behaving like an intruder single-particle state. Furthermore, we see that 2p–2h excitations dominate although higher excitations also play some role. We also see that the neutrons occupying the 1p0f-shell in $N = 20$ systems are principally confined to the $0f_{7/2}$ sub-shell. The conclusions that follow from looking at nuclei with $N > 20$, particularly those with $N = 28$, are that the $N = 20$ shell is nearly completely closed at this point, and that the $N = 28$ closure shell is reasonably robust, although approximately one neutron occupies

Table 7
The calculated SMMC neutron and proton occupation numbers for the sd shell, the $0f_{7/2}$ sub-shell, and the remaining orbitals of the pf shell. The statistical errors are given for linear extrapolations. A systematic error of ± 0.2 should also be included. The first row represents neutron results, while the second row represents protons

	N, Z	1s0d	$0f_{7/2}$	$1p0f_{5/2}$
^{22}Mg	10, 12	3.93 ± 0.02	0.1 ± 0.02	-0.05 ± 0.01
		2.04 ± 0.02	0.00 ± 0.01	-0.05 ± 0.01
^{30}Ne	20, 10	9.95 ± 0.03	2.32 ± 0.03	-0.26 ± 0.02
		2.03 ± 0.02	-0.01 ± 0.01	-0.02 ± 0.01
^{32}Mg	20, 12	9.84 ± 0.03	2.37 ± 0.03	-0.21 ± 0.02
		3.99 ± 0.03	0.05 ± 0.02	-0.05 ± 0.01
^{36}Ar	18, 18	9.07 ± 0.03	1.08 ± 0.02	-0.15 ± 0.02
		9.07 ± 0.03	1.08 ± 0.02	-0.15 ± 0.02
^{40}S	24, 16	11.00 ± 0.03	5.00 ± 0.03	-0.01 ± 0.02
		7.57 ± 0.04	0.54 ± 0.02	-0.12 ± 0.02
^{42}Si	28, 14	11.77 ± 0.02	7.34 ± 0.02	0.90 ± 0.03
		5.79 ± 0.03	0.25 ± 0.02	-0.07 ± 0.01
^{42}S	26, 16	11.41 ± 0.02	6.33 ± 0.02	0.25 ± 0.03
		7.49 ± 0.03	0.58 ± 0.02	-0.09 ± 0.02
^{44}S	28, 16	11.74 ± 0.02	7.18 ± 0.02	1.06 ± 0.03
		7.54 ± 0.03	0.56 ± 0.02	-0.12 ± 0.02
^{44}Ti	22, 22	10.42 ± 0.03	3.58 ± 0.02	0.00 ± 0.02
		10.42 ± 0.03	3.58 ± 0.02	0.00 ± 0.02
^{46}Ar	28, 18	11.64 ± 0.02	7.13 ± 0.02	1.23 ± 0.03
		8.74 ± 0.03	1.34 ± 0.02	-0.08 ± 0.02

Table 8
The calculated total Gamow–Teller strength, GT^-, from this study. The results of other studies, when available, are presented for comparison

Nucleus	SMMC	Other
^{22}Mg	0.578 ± 0.06	
^{30}Ne	29.41 ± 0.25	
^{32}Mg	24.00 ± 0.34	
^{36}Ar	2.13 ± 0.61	
^{40}S	22.19 ± 0.44	22.87 [112]
^{42}S	28.13 ± 0.42	28.89 [112]
^{42}Si	40.61 ± 0.34	
^{44}S	34.59 ± 0.39	34.93 [112]
^{44}Ti	4.64 ± 0.66	
^{46}Ar	29.07 ± 0.44	28.84 [112]

the upper part of the 1p0f shell. Coupling of the protons with the low-lying neutron excitations probably accounts for the relatively large $B(E2)$, without the need of invoking rotational behavior. In Table 8 we show the SMMC total Gamow–Teller (GT^-) strength. We compare our results to those of previous truncated calculations, where available.

In all cases, our results are slightly smaller than, but in good accord with, other calculations. Since we do not calculate the strength function, we do not compute β-decay lifetimes.

5. Non-perturbative resummations: parquet diagrams

5.1. Inclusion of hole–hole contributions and single-particle propagators

With the G-matrix defined according to the double-partitioned scheme we can easily solve Eq. (29) through matrix inversion. The number of hole–hole and particle–particle configurations is then rather small, typically smaller than ~ 100, and a matrix inversion is then rather trivial. Before we discuss the solution of Eq. (29), it is always instructive to consider the contributions to second order in perturbation theory, i.e., diagrams (a) and (b) of Fig. 5. The external legs can be particle states or hole states. Diagram (a) reads

$$\text{(a)} = \frac{1}{2} \sum_{pq} V^{[12]}_{12pqJ} \frac{1}{s - \varepsilon_p - \varepsilon_q} V^{[12]}_{pq34J}, \tag{122}$$

and

$$\text{(b)} = \frac{1}{2} \sum_{\alpha\beta} V^{[12]}_{12\alpha\beta J} \frac{1}{-s + \varepsilon_\alpha + \varepsilon_\beta} V^{[12]}_{\alpha\beta34J}. \tag{123}$$

We note here the minus sign in the energy denominator, since in the latter expression we are using the hole–hole term of the propagator of Eq. (30). If we use a double-partitioned G-matrix for say ^{16}O and are interested in an effective valence space interaction for the 1s0d-shell,[7] then typically the single-particle orbits of the intermediate states will be represented by states in the 1p0f major shell. Hole states are then defined by single-particle states in the 0s and 0p shells. Clearly, the number of two-body intermediate states is rather limited. To third order we have diagrams like (c) and (d) of Fig. 5. Diagram (c) is just the third-order equivalent of Eq. (122) and reads

$$\text{(c)} = \frac{1}{4} \sum_{pqrw} V^{[12]}_{12pqJ} \frac{1}{s - \varepsilon_p - \varepsilon_q} V^{[12]}_{pqrwJ} \frac{1}{s - \varepsilon_r - \varepsilon_w} V^{[12]}_{rw34J}, \tag{124}$$

while diagram (d) contains both a two-particle and a two-hole intermediate state and reads

$$\text{(d)} = \frac{1}{4} \sum_{\alpha\beta pq} V^{[12]}_{12pqJ} \frac{1}{s - \varepsilon_p - \varepsilon_q + \varepsilon_\alpha + \varepsilon_\beta} V^{[12]}_{pq\alpha\beta J} \frac{1}{s - \varepsilon_p - \varepsilon_q} V^{[12]}_{\alpha\beta34J}. \tag{125}$$

Thus, solving Eq. (29) will then yield contributions to the effective interaction such as the above expressions.

Here we have also tacitly assumed that the energy denominators do not diverge, i.e., we have chosen an energy s so that we avoid the poles. This has always been the standard approach in calculations of shell-model effective interactions. To give an example, consider

---

[7] This means that the labels 1234 will refer to particle states in the 1s0d-shell.

now diagram (b) and suppose that we are using harmonic oscillator wave functions. Let us also assume that the two-hole states are from the 0p-shell and that the valence particles are in the 1s0d-shell. If we rescale the energies of the valence space to zero, then the two-hole state would yield -28 MeV with an oscillator parameter $b = 1.72$ fm. If $s = -28$, the denominator diverges. In this case it is rather easy to obtain the imaginary part, and even if we were to choose s different from -28 MeV, the imaginary part will influence the real part of the effective interaction through dispersion relations, see e.g., [49, 50, 119]. It is therefore at best just a first approximation to neglect the imaginary term. Moreover, if we solve Dyson's equation for the self-energy, the single-particle energies may contain an imaginary part. Technically it is however not difficult to deal with imaginary contributions, one needs to invert a complex matrix rather than a real one. These technicalities will however be described elsewhere [120].

Using the double-partitioned G-matrix, we can then rewrite Eq. (29) as

$$\Gamma^{[12]}_{1234J}(s) = G^{[12]}_{1234J} + \frac{1}{2}\sum_{56} G^{[12]}_{1256J}\hat{\mathcal{G}}^{[12]}\Gamma^{[12]}_{5634J}(s), \tag{126}$$

where $G^{[12]}$ is just the double-partitioned G-matrix discussed above. It is also energy dependent, in contrast to V. In case we were to employ this equation for effective interactions in the 1s0d-shell, the intermediate two-particle states would then come from just e.g., the 1p0f-shell. This equation, which now is solved within a much smaller space than the original one spanned by the total Q_{pp}, allows clearly for computationally amenable solutions. It corresponds to the so-called *model-space approach* to the solution of the Feynman–Galitskii equations. Thus, a possible approach would consist of the following steps

1. Solve the G-matrix equation from Eq. (50) using the double-partitioning scheme.
2. The next step is then to solve Eq. (29) and Dyson's equation for the self-energy.
3. This scheme is iterated till self-consistency is achieved, see the discussion below.

We will however not employ this *model-space* scheme in our actual calculations. There are several reasons for not doing so.

Let us first assume that we omit the [13] and [14] channels in our iterative scheme for Eq. (126). The next iteration of Eq. (126) would then look like

$$\Gamma^{[12]}_{(1)} = \Gamma^{[12]}_{(0)} + \Gamma^{[12]}_{(0)}\hat{\mathcal{G}}^{[12]}\Gamma^{[12]}_{(1)}, \tag{127}$$

where the vertex function $\Gamma^{[12]}_{(0)}$ is the solution of Eq. (126). However, we cannot define the "bare" vertex $\Gamma^{[12]}_{(0)}$ to be the solution of Eq. (126) simply because then we would be double-counting contributions. Thus, $\Gamma^{[12]}_{(0)}$ has to equal the G-matrix. The only change in Eq. (127) arises from the solution of Dyson's equation and thereby new single-particle energies.

Let us then for the sake of simplicity assume that the single-particle energies are just the Hartree–Fock solutions. The problem we are aiming at arises at the Hartree–Fock level. In order to obtain Hartree–Fock solutions which are independent of the chosen harmonic oscillator parameter b, we typically need to include single-particle orbits from many major shells. Typical constraints we have found when we do so-called

Brueckner–Hartree–Fock (BHF) calculations for finite nuclei is that we need at least $2n + l \leq 10$ in order to obtain a result which is independent of the chosen b value.[8] The way we solve the BHF equations is to expand the new single-particle wave functions ψ_λ, with λ representing the quantum numbers nlj, in terms of harmonic oscillator wave functions, i.e.,

$$|\psi_\lambda\rangle = \sum_{\alpha=1}^{2n+l} C_\alpha^{(\lambda)} |\phi_\alpha\rangle \tag{128}$$

where ϕ_α are the harmonic oscillator wave functions with quantum numbers $\alpha = nlj$ and C are the coefficients to be varied in the Hartree–Fock calculations. The single-particle energies at the Hartree–Fock level are just

$$\varepsilon_\alpha = t_\alpha + \sum_h \langle \alpha h | G(\varepsilon_\alpha + \varepsilon_h) | \alpha h \rangle, \tag{129}$$

where the single-particle states are just those of the harmonic oscillator. The G-matrix used in the first iteration in the BHF calculation is the one given by the solution of Eq. (50). The coefficients C_α can then be obtained by diagonalizing a matrix of dimension $N \times N$, where N is the number of single-particle orbits with the same lj values.

5.2. Screening corrections and vertex renormalization, the equations for the [13] and [14] channels

We start as in the previous section with the definition of the interaction vertices in the [13] and [14] channels and the corresponding integral equations. Thereafter, we discuss various approximations to these equations such as the summation of TDA and RPA diagrams. Eventually, the aim is to merge the discussion in this section and the preceding one into equations for a self-consistent scheme which combines all three channels, namely the so-called set of parquet equations to be discussed in Section 5.

The equations for the renormalized vertex in the [13] and [14] channels have the same form as Eq. (28), namely

$$\Gamma^{[13]} = V^{[13]} + V^{[13]}(gg)\Gamma^{[13]}, \tag{130}$$

and

$$\Gamma^{[14]} = V^{[14]} + V^{[14]}(gg)\Gamma^{[14]}. \tag{131}$$

The matrix elements which enter are however defined differently and the irreducible diagrams of $V^{[13]}$ and $V^{[14]}$ can obviously not be the same. By irreducible in the [13] channel we will mean a diagram, which by cutting an internal particle–hole pair, cannot be separated into a piece containing the external legs 1, 3 and another piece containing 2, 4 as external legs. The definition for the irreducible vertex in the [14] channel is similar and we illustrate these differences in Fig. 19. Diagram (a) is just the lowest-order interaction in

---

[8] Throughout this work our unperturbed single-particle basis par excellence will always be that of the harmonic oscillator.
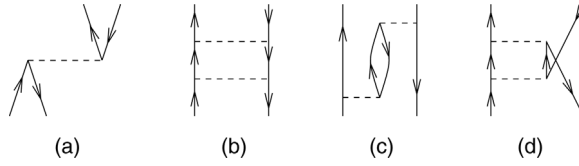
Fig. 19. Examples of irreducible and reducible diagrams in the [13] and [14] channels. See text for further details.

the [13] channel and is therefore irreducible. Diagram (b) is an irreducible diagram in the [13] channel, whereas it is reducible in the [14] channel. Diagram (c) is in turn irreducible in the [14] channel and reducible in the [13] channel. Diagram (d) is an example of a diagram which is irreducible in both channels. This diagram stems from the [12] channel.

The energy variables in these channels are, following Fig. 3 and Eqs. (17) and (18),

$$t = \varepsilon_3 - \varepsilon_1 = \varepsilon_2 - \varepsilon_4, \tag{132}$$

for the [13] channel and

$$u = \varepsilon_1 - \varepsilon_4 = \varepsilon_3 - \varepsilon_2, \tag{133}$$

for the [14] channel. Defining the unperturbed particle–hole propagators in the energy representation as

$$\hat{\mathcal{G}}^{[13]} = \frac{Q_{\mathrm{ph}}^{[13]}}{t - \varepsilon_p + \varepsilon_h + \iota\eta} - \frac{Q_{\mathrm{hp}}^{[13]}}{t + \varepsilon_p - \varepsilon_h - \iota\eta}, \tag{134}$$

and

$$\hat{\mathcal{G}}^{[14]} = \frac{Q_{\mathrm{ph}}^{[14]}}{u - \varepsilon_p + \varepsilon_h + \iota\eta} - \frac{Q_{\mathrm{hp}}^{[14]}}{u + \varepsilon_p - \varepsilon_h - \iota\eta} \tag{135}$$

we arrive at the following equations for the interaction vertex in these two channels

$$\Gamma_{1234J}^{[13]}(t) = V_{1234J}^{[13]} + \sum_{\mathrm{ph}} V_{12\mathrm{ph}J}^{[13]} \hat{\mathcal{G}}^{[13]} \Gamma_{\mathrm{ph}34J}^{[13]}(t), \tag{136}$$

and

$$\Gamma_{1234J}^{[14]}(u) = V_{1234J}^{[14]} - \sum_{\mathrm{ph}} V_{12\mathrm{ph}J}^{[14]} \hat{\mathcal{G}}^{[14]} \Gamma_{\mathrm{ph}34J}^{[14]}(u). \tag{137}$$

These equations, together with Eq. (29), can then form the basis for the first iteration in a self-consistent scheme for renormalization corrections of the parquet type. The origin of the minus sign in Eq. (137) follows from the diagram rules [58] and will be exemplified below. A graphical view of these equations is given in Fig. 20. The reader should also keep in mind the two contributions to the particle propagators of Eqs. (134) and (135).

5.3. Screened ph and 2p2h interactions

Here we study the screening of the particle–hole and the 2p2h interactions given in Fig. 1, indicated by V_{ph} and $V_{2\mathrm{p}2\mathrm{h}}$, respectively. Before we list the final expression, it is
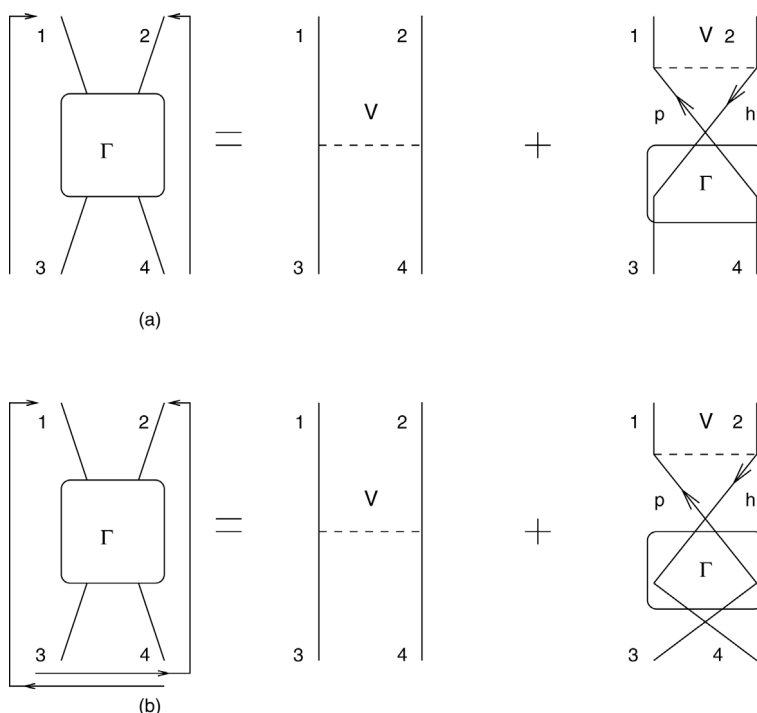
Fig. 20. (a) shows the structure of the integral equation for the interaction vertex in the [13] channel. (b) represents the integral channel for the [14] channel. The coupling order is displayed as well.
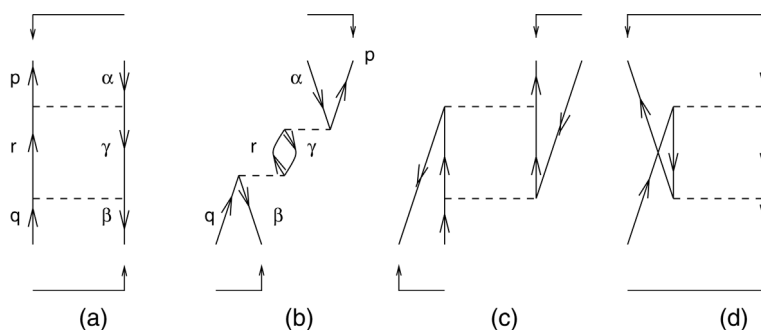

Fig. 21. Second-order perturbation theory corrections to the ph interaction vertex.

however instructive to consider the corrections to second order in the interaction V to the ph and 2p2h vertices. In Fig. 21 we display the second-order corrections to the ph diagrams of Fig. 1. Diagram (a) is the core-polarization correction term to the particle–hole interaction, and corresponds to a contribution from the [14] channel, as indicated by the coupling order. The term labeled (b) corresponds to the exchange term of (a) and is coupled

in the [13] order, see also the discussion in connection with Eqs. (23) and (24). The other corrections, like (c) and (d) include particle–particle and hole–hole intermediate states, respectively. They are irreducible in both the [13] channel and the [14] channel, and can therefore enter the irreducible vertices of these two channels in later iterations. They are however not generated by various iterations of Eqs. (136) and (137). In fact, if we replace V by G in Eqs. (136) and (137), diagram (c) is already accounted for by the G-matrix. It may however be included if the double-partitioned G-matrix of the previous section is used. Let us now look at the analytical expressions in an angular momentum coupled basis for diagrams (a) and (b) of Fig. 21. Here we just include the first term of the propagators of Eqs. (134) and (135). The second terms will give rise to the 2p2h contributions discussed below. In the following discussion we will also assume that the interaction V does not depend on the energy, although it is rather easy to generalize to an energy dependent interaction. Diagram (a) reads

$$\text{(a)} = -\sum_{r\gamma} (-)^{j_r+j_\gamma-J} (-)^{2j_\gamma} V^{[14]}_{p\gamma r\alpha J} \frac{1}{u + \varepsilon_\gamma - \varepsilon_r} V^{[14]}_{r\beta q\gamma J}. \tag{138}$$

The factor $(-)^{2j_\gamma}$ stems from the opening up and recoupling of an internal particle–hole pair [58] and the phase $(-)^{j_r+j_\gamma-J}$ is needed in order to rewrite the matrix elements in the coupling order of Eq. (17). The general structure of Eq. (138) is just of the form $-V^{[14]}_{\text{ph}} Q^{[14]}_{\text{ph}}/\epsilon^{[14]} V^{[14]}_{\text{ph}}$, with $\epsilon^{[14]} = \varepsilon_q + \varepsilon_\gamma - \varepsilon_\beta - \varepsilon_r = u + \varepsilon_\gamma - \varepsilon_r$ and we have defined

$$u = \varepsilon_q - \varepsilon_\beta = \varepsilon_p - \varepsilon_\alpha, \tag{139}$$

for the on-shell energy case. This is the equivalent of the energy variable of Eq. (27) in the [12] channel. Diagram (b) is in turn given by

$$\text{(b)} = \sum_{r\gamma} (-)^{j_r+j_\gamma-J} (-)^{2j_\gamma} V^{[13]}_{\gamma pr\alpha J} \frac{1}{\epsilon^{[13]}} V^{[13]}_{\beta rq\gamma J}, \tag{140}$$

and we note that the contributions are clearly different. The minus sign in Eq. (138) stems from the standard diagram rules [58]. In our use of the diagram rules below, we will omit the use of the rule for the number of external valence hole lines. In our case then, as can also be deduced from inspection of Fig. 21, diagram (a) has zero closed loops and three hole lines, giving thereby rise to a minus sign. Diagram (b) has an additional closed loop and thereby yielding the plus sign. The energy denominator is in this case

$$\epsilon^{[13]} = t + \varepsilon_\gamma - \varepsilon_r, \tag{141}$$

with

$$t = \varepsilon_q - \varepsilon_\beta = \varepsilon_p - \varepsilon_\alpha. \tag{142}$$

We notice, using the relations discussed in Eqs. (23) and (24), that diagram (a) is simply the exchange diagram of (b). We need however to include both diagrams in order to obtain an antisymmetric equation for the particle–hole channels which exhibits the same properties as the [12] channel shown in Eq. (26). *This is actually crucial in solving the parquet equations. We wish namely that every iteration, with a given approximation to the vertex*
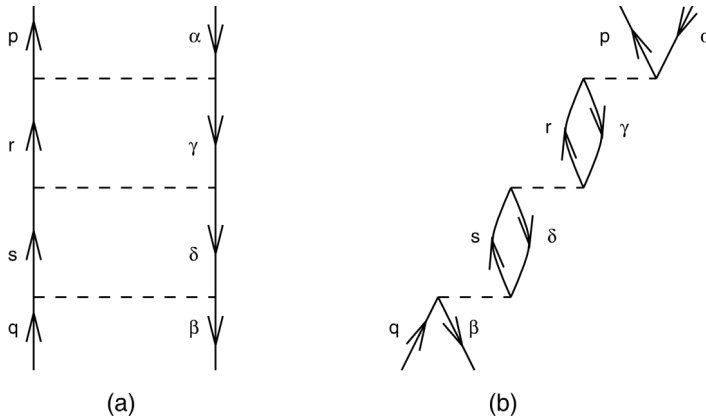
Fig. 22. Corrections beyond second order in the interaction V to the ph interaction vertex. (a) is in the [14] channel and (b) is in the [13] channel.

function V, preserves the antisymmetry property. This point cannot be emphasized enough. Let us now see what happens to third order in the interaction. Third-order corrections to the ph vertices (a) and (b) involving only ph intermediate states are shown in (a) and (b) of Fig. 22, respectively. The analytical expression for the third-order contribution (a) is given by

$$\text{(a)} = \sum_{rs\gamma\delta} f V_{p\gamma r\alpha J}^{[14]} \frac{1}{u + \varepsilon_\gamma - \varepsilon_r} V_{r\delta s\gamma J}^{[14]} \frac{1}{u + \varepsilon_\delta - \varepsilon_s} V_{s\beta q\delta J}^{[14]}, \tag{143}$$

with $f = (-)^{j_r + j_s + j_\gamma + j_\delta - 2J} (-)^{2j_\gamma + 2j_\delta}$. This equation has the general structure

$$V_{\text{ph}}^{[14]} \frac{Q_{\text{ph}}^{[14]}}{\epsilon^{[14]}} V_{\text{ph}}^{[14]} \frac{Q_{\text{ph}}^{[14]}}{\epsilon^{[14]}} V_{\text{ph}}^{[14]}.$$

A similar expression applies to diagram (b), whose expression is

$$\text{(b)} = \sum_{rs\gamma\delta} f V_{\gamma pr\alpha J}^{[13]} \frac{1}{t + \varepsilon_\gamma - \varepsilon_r} V_{\gamma rs\delta J}^{[13]} \frac{1}{t + \varepsilon_\delta - \varepsilon_s} V_{\beta sq\delta J}^{[13]}. \tag{144}$$

It has the general structure

$$V_{\text{ph}}^{[13]} \frac{Q_{\text{ph}}^{[13]}}{\epsilon^{[13]}} V_{\text{ph}}^{[13]} \frac{Q_{\text{ph}}^{[13]}}{\epsilon^{[13]}} V_{\text{ph}}^{[13]}.$$

But these expressions have the same sign! Diagram (a) counts now 4 hole lines, and (b) counts also 4 hole lines and 2 closed loops. However, *there are three interaction terms V*, and taking the exchange term of each of these in diagram (a) leads to the desired results, namely (a) $= -$(b), as it should. Thus, to third order we keep the antisymmetry property of Γ in the [13] and [14] channels. It is easy to see that in the [14] channel we will always have an alternating sign in front of each contribution, since every new order in perturbation theory brings a new hole line and no closed loop, and thus a new minus sign.
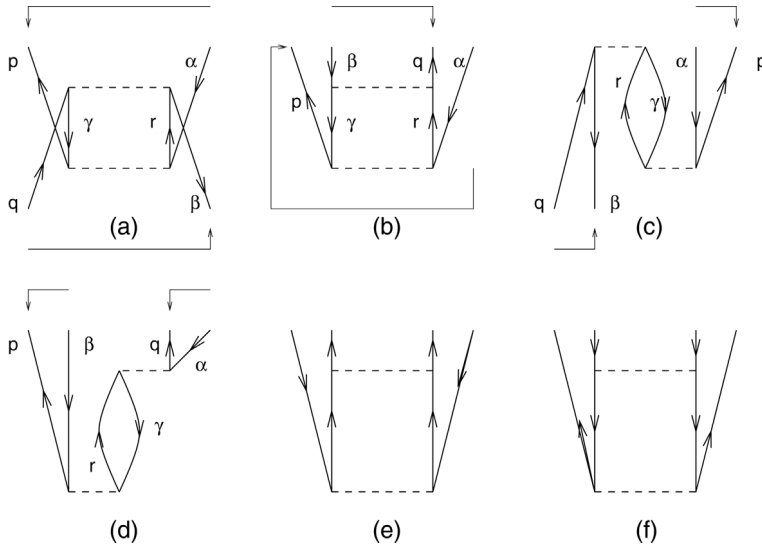
Fig. 23. Corrections to second order in V of the 2p2h vertex.

In the [13] channel we have always one new hole line and one new closed loop for every new vertex. If we consider only the screening of the ph vertex, we can then set up a perturbative expansion in terms of the ph vertex for the vertex functions $\Gamma^{[13]}$ and $\Gamma^{[14]}$. For notational economy we will skip the Pauli operators $Q^{[ij]}_{\mathrm{ph,hp}}$ in the discussions below. It will always be understood that the intermediate states are two-body particle–hole states, $|\mathrm{ph}\rangle$ or $|\mathrm{hp}\rangle$. Consider e.g., $\Gamma^{[14]}$

$$\Gamma^{[14]} = V^{[14]}_{\mathrm{ph}} - V^{[14]}_{\mathrm{ph}} \frac{1}{\epsilon^{[14]}} V^{[14]}_{\mathrm{ph}} + V^{[14]}_{\mathrm{ph}} \frac{1}{\epsilon^{[14]}} V^{[14]}_{\mathrm{ph}} \frac{1}{\epsilon^{[14]}} V^{[14]}_{\mathrm{ph}} - + \cdots, \tag{145}$$

which can be summed up to yield

$$\Gamma^{[14]} = V^{[14]}_{\mathrm{ph}} - V^{[14]}_{\mathrm{ph}} \frac{1}{\epsilon^{[14]} - V^{[14]}_{\mathrm{ph}}} V^{[14]}_{\mathrm{ph}} = V^{[14]}_{\mathrm{ph}} - V^{[14]}_{\mathrm{ph}} \frac{1}{\epsilon^{[14]}} \Gamma^{[14]}, \tag{146}$$

which is the standard TDA expression for the ph term. The corresponding expression in the [13] channel results in

$$\Gamma^{[13]} = V^{[13]}_{\mathrm{ph}} + V^{[13]}_{\mathrm{ph}} \frac{1}{\epsilon^{[13]}} \Gamma^{[13]}. \tag{147}$$

The signs agree with the expressions of Blaizot and Ripka [41], see Chapter 15 and Eq. (15.50). The summations in both channels ensure that the final vertex is antisymmetric and the combination of the latter two equations results in the familiar TDA equations. We next look at the 2p2h matrix element and show the corresponding corrections to second order in perturbation theory in Fig. 23. If we omit diagrams (e) and (f) which contain 2p and 2h intermediate states generated by the solutions in the [12] channel, we have for diagram (a)

$$(a) = -\sum_{r\gamma}(-)^{j_r+j_\gamma-J}(-)^{2j_\gamma}V^{[14]}_{\gamma\beta qrJ}\frac{1}{-u+\varepsilon_\gamma-\varepsilon_r}V^{[14]}_{pr\gamma\alpha J}, \tag{148}$$

with the general structure

$$-V^{[14]}_{2p2h}\frac{1}{\epsilon^{[14]}}V^{[14]}_{2p2h}. \tag{149}$$

Note well the minus sign in front of u. The contribution from the propagator can in this case be retraced to the second term of the propagator of Eq. (135). Diagram (a) follows the coupling order of the [14] channel. It is also easy to see that diagram (b) is given by

$$(b) = -\sum_{r\gamma}(-)^{j_r+j_\gamma-J}(-)^{2j_\gamma}V^{[14]}_{\gamma q\beta rJ}\frac{1}{-u+\varepsilon_\gamma-\varepsilon_r}V^{[14]}_{pr\gamma\alpha J}, \tag{150}$$

and has the structure

$$-V^{[14]}_{\text{ph}}\frac{1}{\epsilon^{[14]}}V^{[14]}_{2p2h}. \tag{151}$$

Similarly, if we now move to the [13] channel we have the following expressions

$$(c) = \sum_{r\gamma}(-)^{j_r+j_\gamma-J}(-)^{2j_\gamma}V^{[13]}_{\beta\gamma qrJ}\frac{1}{-t+\varepsilon_\gamma-\varepsilon_r}V^{[13]}_{qp\gamma\alpha J}, \tag{152}$$

and

$$(d) = \sum_{r\gamma}(-)^{j_r+j_\gamma-J}(-)^{2j_\gamma}V^{[13]}_{\gamma qr\alpha J}\frac{1}{-t+\varepsilon_\gamma-\varepsilon_r}V^{[13]}_{pr\beta\gamma J}, \tag{153}$$

with the general structure

$$V^{[13]}_{2p2h}\frac{1}{\epsilon^{[13]}}V^{[13]}_{2p2h}, \tag{154}$$

and

$$V^{[13]}_{\text{ph}}\frac{1}{\epsilon^{[13]}}V^{[13]}_{2p2h}, \tag{155}$$

respectively. Diagram (c) is just the exchange of (a) and includes two 2p2h vertices, while diagram (d) is the exchange of diagram (b) and includes a ph vertex multiplied with a 2p2h vertex. We note again that the antisymmetry is ensured at a given order in the interaction only if we include the corrections at the same level in both channels.

One can then easily sum up higher-order corrections to the 2p2h diagrams as well in both channels. The inclusion of the backward going particle–hole pair in the propagators of Eqs. (134) and (135) ensures thus that we will also sum to infinite order 2p2h corrections. This leads ultimately to the familiar RPA equations, see e.g., [48].

A closer inspection of Eqs. (150) and (153) shows that if we only include ph vertices, we could resum these corrections to infinite order for the 2p2h vertex by observing that the structure of such diagrams would be of the form (e.g., in the [14] channel)

$$\Gamma_{2p2h}^{[14]} = V_{2p2h}^{[14]} - V_{ph}^{[14]} \frac{1}{\epsilon^{[14]}} V_{2p2h}^{[14]} + V_{ph}^{[14]} \frac{1}{\epsilon^{[14]}} V_{ph}^{[14]} \frac{1}{\epsilon^{[14]}} V_{2p2h}^{[14]} + \cdots, \tag{156}$$

which can be summed up to yield

$$\Gamma_{2p2h}^{[14]} = V_{2p2h}^{[14]} - V_{ph}^{[14]} \frac{1}{\epsilon^{[14]} - V_{ph}^{[14]}} V_{2p2h}^{[14]}, \tag{157}$$

and similarly for the [13] channel, but with a plus sign. The modifications discussed in Eqs. (146) and (157) serve to modify the propagation of a particle–hole pair and have normally been termed for propagator renormalizations, as can easily be seen from Eqs. (146) and (157) where the propagation of a free particle–hole pair is modified by the presence of the interaction V in the energy denominator. Other important processes which can affect e.g., various polarization terms are those represented by so-called vertex renormalizations, a term originally introduced by Kirson and Zamick [121]. These authors studied the renormalizations of the 2p1h and 2h1p vertices as well, see also Kirson [47] and Ellis and Osnes [48] for further discussions. We will therefore end the discussion in this section by looking at such renormalizations.

5.4. Further renormalizations

In the previous subsection we dealt mainly with what has conventionally been labeled for propagator renormalizations. We will therefore extend the standard TDA and RPA scheme by looking at further ways of renormalizing interaction vertices. The approach discussed here follows Kirson [47]. Extensions were made later by Ellis and Goodin [122] and Ellis, Mavromatis and Müther [54]. We will limit the discussion here to the scheme of Kirson. We start therefore with the contributions to second order to the 2p1h vertex.[9] These contributions are shown in Fig. 24. Diagram (a) consists of a 2p1h vertex multiplied with a ph vertex whereas (b) stems from the multiplication of a 2p2h vertex with a 2p1h vertex. They both contain a particle–hole pair as an intermediate state and follow the coupling order of the [14] channel. The exchange diagram of (b) is given by (c), while that of (a) is diagram (d). Diagrams (e) and (f) represent contributions from the [12] channel and are irreducible in both particle–hole channels. Before we sketch the general structure of the renormalization procedure of Kirson, it is instructive to consider again the equations to second order in perturbation theory, as the general expressions can be deduced from inspection of these diagrams. Diagram (a) is

$$(a) = \sum_{r\gamma} (-)^{j_r + j_\gamma - J} (-)^{2j_\gamma} V_{p\gamma r\alpha J}^{[14]} \frac{1}{u + \varepsilon_\gamma - \varepsilon_r} V_{rsq\gamma J}^{[14]}, \tag{158}$$

and the plus sign stems from the diagram rules [58], i.e., we have two hole lines and no closed loop. The propagator is that arising from the first term in Eq. (135). The general structure is

$$V_{ph}^{[14]} \frac{1}{\epsilon^{[14]}} V_{2p1h}^{[14]}. \tag{159}$$

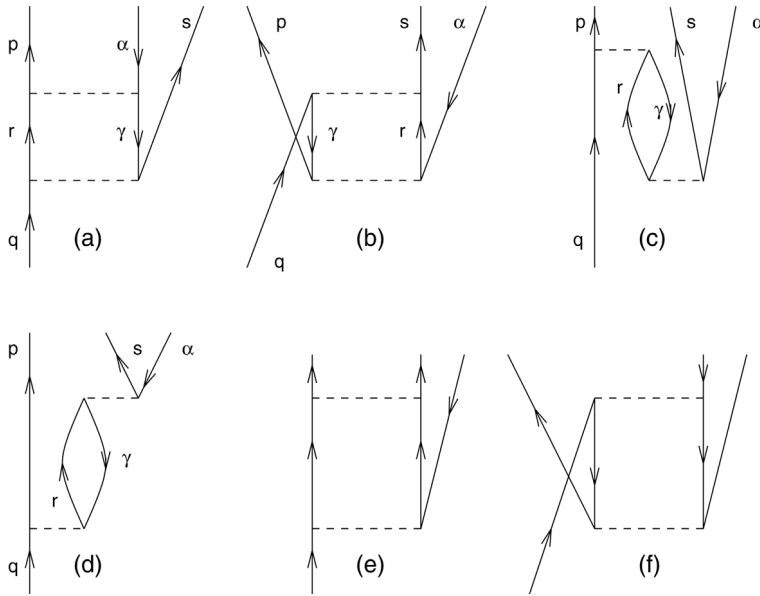[9] The discussion here applies to the other interaction vertices discussed in Fig. 1.

Fig. 24. The corrections to second order in V of the 2p1h vertex.

Diagram (b) reads

$$(b) = \sum_{r\gamma} (-)^{j_r+j_\gamma-J} (-)^{2j_\gamma} V^{[14]}_{pr\gamma\alpha J} \frac{1}{-u+\varepsilon_\gamma-\varepsilon_r} V^{[14]}_{\gamma sqr J}, \tag{160}$$

with the following structure

$$V^{[14]}_{2p1h} \frac{1}{\epsilon^{[14]}} V^{[14]}_{2p2h}. \tag{161}$$

In this case the propagator stems from the second term in Eq. (135). Similar equations arise for e.g., the 2h1p vertices of Fig. 1.

Before we write down the self-consistent equations of Kirson [47], let us assume that we can approximate the 2p1h vertex in the [14] channel by the first-order term and diagrams (a) and (b). This renormalized vertex, which we here label $\tilde{V}_{2p1h}$, is then given by

$$\tilde{V}_{2p1h} \approx V^{[14]}_{2p1h} + V^{[14]}_{ph} \frac{1}{\epsilon^{[14]}} V^{[14]}_{2p1h} + V^{[14]}_{2p1h} \frac{1}{\epsilon^{[14]}} V^{[14]}_{2p2h}. \tag{162}$$

If we now allow for the screening to infinite order of the ph vertex given by Eq. (146) and replace the 2p2h vertex in the above equation with Eq. (157) we obtain the following renormalization of the 2p1h vertex

$$\tilde{V}_{2p1h} = V^{[14]}_{2p1h} + V^{[14]}_{ph} \frac{1}{\epsilon^{[14]} - V^{[14]}_{ph}} V^{[14]}_{2p1h} + V^{[14]}_{2p1h} \frac{1}{\epsilon^{[14]} - V^{[14]}_{ph}} V^{[14]}_{2p2h}. \tag{163}$$
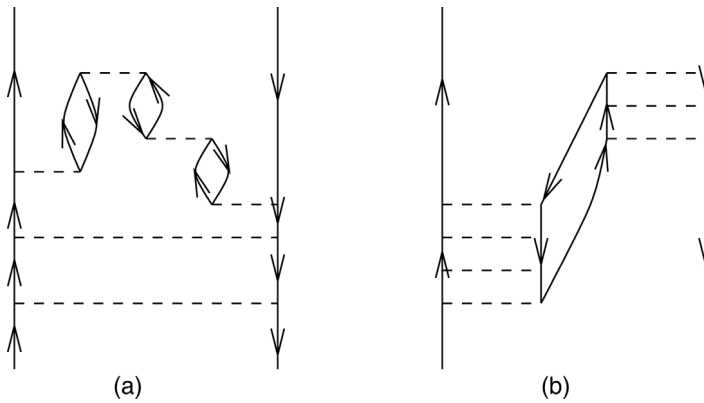
Fig. 25. Examples of diagrams which can arise from Kirson's self-consistent equations.

A similar equation applies to the 2h1p vertex of Fig. 1 and for the [13] channel. Eqs. (146), (157) and (163) form then the starting point for the approach of Kirson [47]. Examples of diagrams which can be obtained through the iterative solution of Eqs. (146), (157) and (163) are given in Fig. 25.

The question now is however how to relate Eqs. (146), (157) and (163) with those from Eqs. (136) and (137). This is rather trivial if we recall that the labels 1234 can, as was also discussed in Section 2, represent whatever single-particle states, either holes or particles. Thus, V_{1234} can represent a 2p1h, 2h1p, 2p2h, 2p, 2h or a ph vertex. This means that, due to the choice of propagators in Eqs. (134) and (135) equations like Eq. (163) are already inherent in Eqs. (136) and (137). If we e.g., approximate Eq. (137) to second order in the interaction V and let the single-particle labels 1234 represent a 2p1h interaction vertex, we immediately reobtain Eq. (162). If we let 1234 represent a 2p2h vertex, we find to second-order diagrams (a)–(d) of Fig. 23.

Till now we have however refrained from discussing the contributions from the [12] channel, examples were only shown in (c) and (d) of Fig. 21, (e) and (f) of Figs. 23 and 24. These diagrams cannot be generated by simply iterating the equations for the [13] and [14] channels, but they could enter as contributions to the irreducible vertex in the [13] and [14] channels from the first iteration in the [12]-channel. We see thus the emerging contour of an iterative scheme. The crucial point is however how to perform the next iteration of say Eqs. (146), (157) and (163) or Eqs. (29), (136) and (137) from the [12] channel. The question is how do we include the results from the first iteration into the next one, i.e., how to modify the bare vertices $V^{[13]}$ and $V^{[14]}$ in e.g., Eqs. (136) and (137) in order to obtain an effective interaction for the shell model. We have also not addressed how to deal with the solution of Dyson's equation for the one-body Green's function. We mention also that Ellis and Goodin [122] included pp correlations, i.e., terms from the [12] channel such as diagram (e) of Fig. 24, as well when they considered the screening of the 2p1h and 2h1p vertices. Furthermore, as already mentioned in the introduction the authors of [54, 55] extended the pp RPA to include the particle–hole (ph) RPA, though screening of the 2p1h and 2h1p vertices was not included. In [55] however, a study with self-consistent

single-particle energies was also performed. These works represent thus a first serious step towards the solution of the parquet equations, i.e., a many-body scheme which solves self-consistently the equations in the [12], [13] and [14] channels, with the addition of the self-consistent evaluation of the self-energy. It ought also to be mentioned that one of the first real applications for nuclear systems was performed in a series of papers by Dickhoff and Müther and co-workers [123] for nuclear matter. These authors actually performed the first iteration of the three channels.

5.5. Parquet diagrams

The equations we discussed in the two previous sections can be generalized in matrix form as

$$\Gamma = \Gamma^{[ij]} + \Gamma^{[ij]} \hat{\mathcal{G}}^{[ij]} \Gamma, \tag{164}$$

where obviously [ij] represents a given channel, $\hat{\mathcal{G}}^{[ij]}$ is the particle–particle, or hole–hole or particle–hole propagator. The propagator is a product of two single-particle propagators g which we do not specify any further here. They are defined by the solution of Dyson's equation in Eq. (31). The irreducible vertices must appear in the solution of the self-energy, and conversely, the self-energy must appear in all single-particle propagators within the expressions for the three channels [12], [13] and [14].

For all of our practical purposes, the irreducible vertex used in all channels is the G-matrix defined by the large model space of Fig. 9.

Let us now define the contribution from the [12], [13] and [14] channels following [40]. Eq. (29) is then rewritten as

$$L = \Gamma^{[12]} - G, \tag{165}$$

where obviously L stands for ladder. The ladder term can then be rewritten as

$$L = G\hat{\mathcal{G}}^{[12]}G + G\hat{\mathcal{G}}^{[12]}L. \tag{166}$$

In a similar way we can define the diagrams beyond first order in the particle–hole channel as

$$R^{[13]} = \Gamma^{[13]} - G, \tag{167}$$

and

$$R^{[14]} = \Gamma^{[14]} - G, \tag{168}$$

where G now is coupled in either the [13] or [14] way. Rewriting $R^{[ij]}$, where R refers to ring diagrams, we obtain

$$R^{[ij]} = G\hat{\mathcal{G}}^{[ij]}G + G\hat{\mathcal{G}}^{[ij]}R^{[ij]}, \tag{169}$$

where ij stands for either [13] or [14]. The equation for the vertex function Γ in Eq. (164) becomes then

$$\Gamma = G + L + R^{[13]} + R^{[14]}. \tag{170}$$

Note here that the vertex Γ can be represented in the coupling order of any of the above channels. Our convention is that of the [12] channel.

If Eqs. (166) and (169) define the first iteration, it should be fairly obvious to see that the next iteration would be

$$L = (G + R^{[13]} + R^{[14]})\hat{\mathcal{G}}^{[12]}(G + R^{[13]} + R^{[14]}) + (G + R^{[13]} + R^{[14]})\hat{\mathcal{G}}^{[12]}L, \tag{171}$$

where the contributions $R^{[13]} + R^{[14]}$ are recoupled according to the coupling order of the 12-channel. These contributions are irreducible in the [12] channel. Similarly, for the rings we have

$$R^{[13]} = (G + L + R^{[14]})\hat{\mathcal{G}}^{[13]}(G + L + R^{[14]}) + (G + L + R^{[14]})\hat{\mathcal{G}}^{[13]}R^{[14]}, \tag{172}$$

and

$$R^{[14]} = (G + L + R^{[13]})\hat{\mathcal{G}}^{[14]}(G + L + R^{[13]}) + (G + L + R^{[13]})\hat{\mathcal{G}}^{[14]}R^{[14]}. \tag{173}$$

Our scheme for calculating Γ will be an iterative one based on Eqs. (170)–(173) and the solution of Dyson's equation for the single-particle propagator. This set of equations will then yield the two-body parquet diagrams. Relating the above equations to the discussions above it is rather easy to see that the G-matrix, TDA, RPA and Kirson's screening scheme are contained in Eqs. (170)–(173). Applications of this method will be presented elsewhere [120]. However, we present here a numerically viable approach to the parquet equations. Here we will limit ourselves to just sketching the structure of the solution, more technical details can be found in [120].

The iterative scheme starts with the solution of Eq. (29). We define then $Q^{[12]} = Q_{\text{pp}} + Q_{\text{hh}}$ which results in

$$\Gamma^{[12]}_{(0)} = G + G \left(\frac{Q^{[12]}}{s - H_0} \right) \Gamma^{[12]}_{(0)}. \tag{174}$$

The subscript (0) means that this is just the first iteration. The single-particle energies are the unperturbed harmonic oscillator energies.

The first step in our calculations is to evaluate G. It is calculated following the discussion of Section 3, employing a large model space. The exclusion operator for this G-matrix was defined in Fig. 9 and is typically defined for 6–10 major oscillator shells, as discussed in connection with Fig. 11. There, 8 major oscillator shells were needed in order to obtain a converged result. Similar results are obtained in the coupled cluster calculations discussed in the next section.

The second step is to solve Eq. (174), which is now a complex equation. The hole states and particle states are then defined according to Fig. 10. These single-particle states define then the projection operator $Q^{[12]} = Q_{\text{pp}} + Q_{\text{hh}}$. This equation is then solved by matrix diagonalization, yielding a Green's function and the pertinent new vertex.

These two steps lead then to the first iteration of the ladders, i.e.,

$$L_{(0)} = \Gamma^{[12]}_{(0)} - G. \tag{175}$$

It contains both hole–hole and particle–particle intermediate states and is a complex matrix. The external single-particle legs can be particles or holes. Only unperturbed single-particle energies enter the definition of the two-body propagators.

The third step is to calculate the first iteration for the rings, namely

$$R_{(0)}^{[13]} = (G + L_{(0)})\hat{\mathcal{G}}^{[13]}(G + L_{(0)}) + (G + L_{(0)})\hat{\mathcal{G}}^{[13]}R_{(0)}^{[13]}, \tag{176}$$

and

$$R_{(0)}^{[14]} = (G + L_{(0)})\hat{\mathcal{G}}^{[14]}(G + L_{(0)}) + (G + L_{(0)})\hat{\mathcal{G}}^{[14]}R_{(0)}^{[14]}. \tag{177}$$

The equations for L and R are all defined within a truncated Hilbert space. They can therefore be recast into matrix equations of finite dimensionality. Recall also that we need to recouple the contribution from the [12] channel into the relevant ones for the [13] and [14] channels. This is done employing Eqs. (17) and (18). With these contributions, we can now obtain the vertex function Γ after the first interaction

$$\Gamma_{(0)} = G + L_{(0)} + R_{(0)}^{[13]} + R_{(0)}^{[14]}. \tag{178}$$

The fourth step is to compute the self-energy and thereby obtain new single-particle energies. In so doing, care has to be exercised in order to avoid double-counting problems. A thorough discussion of this topic can be found in [40]. More details will also be presented in [120]. The new single-particle wave functions are obtained by diagonalizing a matrix of dimension $n_\alpha \times n_\alpha$, n_α the quantum number n of the single-particle state α.

The fifth step is to repeat steps 1–4 with the new single-particle energies till a predetermined self-consistency is obtained. But now the rings have to be included in all equations, i.e., we solve Eqs. (170)–(173).

The final vertex Γ can then be used to define a new effective interaction to be applied in shell-model studies, where many more diagrams are considered than in the present state-of-the-art calculations, see e.g., Fig. 8 of [40] for a list of diagrams to sixth order entering the definition of the irreducible vertex Γ.

The same technique employing a large model space is used in our coupled-cluster calculations discussed in the next section.

6. Non-perturbative resummations: coupled cluster theory

As we have seen from the above discussions, nuclear many-body theory often begins with a G-matrix interaction which is derived from an underlying bare nucleon–nucleon interaction. In this section we limit the discussion to the no-core G-matrix so that all particles are active within our chosen model space. Using a given basis expansion of the many-body wave function we could then solve the nuclear problem by diagonalization as has been pursued by the no-core shell model collaboration [1–3, 74]. In fact, the current and most advanced no-core oscillator expansion techniques have approached ^{12}C, with nearly converged solutions [124].

It should be evident, however, that diagonalization procedures scale almost combinatorially with the number of particles in a given number of single-particle orbitals. Because of this scaling, diagonalization simply becomes untenable at some point.

Table 9
Dimensions of the shell-model problem in four major oscillator shells and 7 major oscillator shells with $M = 0$

System	4 shells	7 shells
^{4}He	4E4	9E6
^{8}B	4E8	5E13
^{12}C	6E11	4E19
^{16}O	3E14	9E24

The efforts to expand diagonalization into p-shell nuclei with all nucleons active, an effort that spans over ten years, illustrates the problem. The computational complexity of the nucleus grows dramatically as the size of the nucleus increases. As a simple example consider oscillator single-particle states, and single-particle spaces consisting of 4 and 7 major oscillator shells, and compare the number of uncoupled many-body basis states there are for 4, 8, 12, and 16 particles. From Table 9 we see an enormous growth of the standard shell-model diagonalization problem within the space. We calculated the number of $M = 0$ states for He and B within the model space consisting of 4 major shells and estimated the number of basis states for C and O. Also indicated are similar estimates for seven major oscillator shells. The important lesson to learn from these numbers is that the model-space expansion becomes astronomical quite quickly.

Yet, because of the advent of radioactive nuclear beam accelerators, such as the proposed rare isotope accelerator (RIA) in the US, we face the daunting task of moving beyond p-shell nuclei in ab initio calculations. We should therefore investigate several ways of approaching the nuclear many-body problem in order to successfully make the move into the RIA era.

One motivation for developing auxiliary field Monte Carlo (see Section 4 above) for the shell model was to overcome the scaling problem. Other many-body methods that resum major classes of many-body diagrams have simply been neglected in nuclear science to this point. In this section we will discuss the coupled-cluster technique which can be used to pursue nuclear many-body calculations to heavier systems beyond the p-shell.

Coupled-cluster theory originated in nuclear physics [19, 20] around 1960. Early studies in the 1970s [31] probed ground-state properties in limited spaces with free nucleon–nucleon interactions available at the time. The subject was revisited only recently by Bishop et al. [32], for further theoretical development, and by Mihaila and Heisenberg [36], for coupled-cluster calculations using realistic two- and three-nucleon bare interactions and expansions in the inverse particle–hole energy spacings. However, much of the impressive development in coupled-cluster theory made in quantum chemistry in the last 15-20 years [22, 125–128] still awaits applications to the nuclear many-body problem.

Many solid theoretical reasons exist that motivate a pursuit of coupled-cluster methods. First of all, the method is fully microscopic and is capable of systematic and hierarchical improvements. Indeed, when one expands the cluster operator in coupled-cluster theory to all A particles in the system, one exactly produces the fully-correlated many-body wave function of the system. The only input that the method requires is the nucleon–nucleon interaction. The method may also be extended to higher-order interactions such as

the three-nucleon interaction. Second, the method is size extensive which means that only linked diagrams appear in the computation of the energy (the expectation value of the Hamiltonian) and amplitude equations. As discussed in [22] all shell-model calculations that use particle–hole truncation schemes actually suffer from the inclusion of unconnected diagrams in computations of the energy. Third, coupled-cluster theory is also size consistent which means that the energy of two non-interacting fragments computed separately is the same as that computed for both fragments simultaneously. In chemistry, where the study of reactions is quite important, this is a crucial property not available in the interacting shell model (named configuration interaction in chemistry). Fourth, while the theory is not variational, the energy behaves as a variational quantity in most instances. Finally, from a computational point of view, the practical implementation of coupled-cluster theory is amenable to parallel computing.

We are in the process of applying quantum chemistry inspired coupled cluster methods [22, 125–132] to finite nuclei [71, 133]. We show one result from our current studies, namely the convergence of ^{16}O as a function of the model space in which we perform the calculations.

The basic idea of coupled-cluster theory is that the correlated many-body wave function $|\Psi\rangle$ may be obtained by application of a correlation operator, T, such that

$$|\Psi\rangle = \exp(-T)|\Phi\rangle, \tag{179}$$

where Φ is a reference Slater determinant chosen as a convenient starting point. For example, we use the filled 0s state as the reference determinant for ^{4}He.

The correlation operator T is given by

$$T = T_1 + T_2 + \cdots + T_A, \tag{180}$$

and represents various n-particle–n-hole (np–nh) excitation amplitudes such as

$$T_1 = \sum_{a\langle\varepsilon_f,i\rangle\varepsilon_f} t_i^a a_a^\dagger a_i, \tag{181}$$

$$T_2 = \tfrac{1}{4} \sum_{i,j\langle\varepsilon_f;ab\rangle\varepsilon_f} t_{ij}^{ab} a_a^\dagger a_b^\dagger a_j a_i, \tag{182}$$

and higher-order terms for T_3 to T_A. We are currently exploring the coupled-cluster method at the T_1 and T_2 level. This is commonly referred to in the literature as coupled-cluster singles and doubles (CCSD).

We compute the expectation of the ground-state energy from

$$E_{\text{g.s.}} = \langle\Psi_0|\exp(-T)H\exp(T)|\Psi_0\rangle. \tag{183}$$

The Baker–Hausdorf relation may be used to rewrite the similarity transformation as

$$\exp(-T)H\exp(T) = H + [H, T_1] + [H, T_2] + \tfrac{1}{2}[[H, T_1], T_1] + \tfrac{1}{2}[[H, T_2], T_2]$$
$$+ [[H, T_1], T_2] + \cdots. \tag{184}$$

The expansion terminates exactly at four-nested commutators when the Hamiltonian contains, at most, two-body terms, and at six-nested commutators when three-body potentials are present. We stress that this termination is exact, thus allowing for a derivation

of exact expressions for the T_1 (1p–1h) and T_2 (2p–2h) amplitudes. The equations for amplitudes are found by left projection of excited Slater determinants so that

$$
\begin{aligned}
0 &= \langle \Phi_i^a | \exp(-T) H \exp(T) | \Phi \rangle, \\
0 &= \langle \Phi_{ij}^{ab} | \exp(-T) H \exp(T) | \Phi \rangle.
\end{aligned}
\tag{185}
$$

The commutators also generate non-linear terms within these expressions. To derive these equations is straightforward, but tedious, work [22]. While the resulting equations for the single and double excitation amplitudes appear quite lengthy, they are solvable through iterative techniques.

The Hamiltonian may be written in a slightly more convenient form by explicitly calculating the expectation of the Hamiltonian in the reference state $|\Phi\rangle$, $E_0 = \langle \Phi | H | \Phi \rangle$. This reference state is a single Slater determinant and represents, in this work, a doubly closed shell system. In this case, the Hamiltonian becomes

$$
H = \sum_{pq} f_{pq} \{a_p^\dagger a_q\} + \tfrac{1}{4} \langle pq | G | rs \rangle \{a_p^\dagger a_q^\dagger a_s a_r\} + E_0,
\tag{186}
$$

where the {} indicates normal ordering relative to the Fermi vacuum. The Fock operator is given by

$$
f_{pq} = \langle p | K | q \rangle + \sum_i \langle pi | G | qi \rangle.
\tag{187}
$$

Using this form, and solving for the amplitudes, the energy of the system may then be calculated. The CCSD energy is

$$
\langle H \rangle = E_{\mathrm{CCSD}} = \sum_{ia} f_{ia} t_i^a + \tfrac{1}{4} \sum_{aibj} \langle ij | G | ab \rangle t_{ij}^{ab} + \tfrac{1}{2} \sum_{aibj} \langle ij | G | ab \rangle t_i^a t_j^b + E_0.
\tag{188}
$$

This equation is not restricted to the CCSD approximation. Since higher-order excitation operators such as T_3 and T_4 cannot produce fully contracted terms with the two-body Hamiltonian, their contribution to the energy equation is zero. Higher-order excitation clusters can contribute indirectly to the energy through the equations used to determine the amplitudes.

Because of the non-linearity of the equations, one must have a good first guess for the np–nh amplitudes. For closed-shell nuclei, we use a Møller–Plesset-like approach to generate the first guess for the iteration:

$$
\begin{aligned}
t_i^a(1) &= \frac{f_{ai}}{D_{ai}}, \\
t_{ij}^{ab}(1) &= \frac{\langle ab | G | ij \rangle}{D_{ijab}},
\end{aligned}
\tag{189}
$$

where $D_{ia} = f_{ii} - f_{aa}$, and $D_{ijab} = f_{ii} + f_{jj} - f_{aa} - f_{bb}$ are single-particle energy denominators. Using this as a first guess, we can iterate the projection equations (185) until we find the converged amplitudes. Finally, we list the expressions for the T_1 and T_2

amplitudes. The T_1 amplitude equations are given by

$$
\begin{aligned}
0 = {} & f_{ai} + \sum_c f_{ac} t_i^c - \sum_k f_{ki} t_k^a + \sum_{kc} \langle ka||ci\rangle t_k^c + \sum_{kc} f_{kc} t_{ik}^{ac} \\
& + \tfrac{1}{2}\sum_{kcd} \langle ka||cd\rangle t_{ki}^{cd} - \tfrac{1}{2}\sum_{klc} \langle kl||ci\rangle t_{kl}^{ca} - \sum_{kc} f_{kc} t_i^c t_k^a - \sum_{klc} \langle kl||ci\rangle t_k^c t_l^a \\
& + \sum_{kcd} \langle ka||cd\rangle t_k^c t_i^d - \sum_{klcd} \langle kl||cd\rangle t_k^c t_i^d t_l^a + \sum_{klcd} \langle kl||cd\rangle t_k^c t_{li}^{da} \\
& - \tfrac{1}{2}\sum_{klcd} \langle kl||cd\rangle t_{ki}^{cd} t_l^a - \tfrac{1}{2}\sum_{klcd} \langle kl||cd\rangle t_{kl}^{ca} t_i^d .
\end{aligned}
\tag{190}
$$

This equation is non-linear in the T_1 amplitudes, and linear in the T_2 amplitudes.

The T_2 amplitude equations are given by

$$
\begin{aligned}
0 = {} & \langle ab||ij\rangle + \sum_c (f_{bc} t_{ij}^{ac} - f_{ac} t_{ij}^{bc}) - \sum_k (f_{kj} t_{ik}^{ab} - f_{ki} t_{jk}^{ab}) \\
& + \tfrac{1}{2}\sum_{kl} \langle kl||ij\rangle t_{kl}^{ab} + \tfrac{1}{2}\sum_{cd} \langle ab||cd\rangle t_{ij}^{ac} + P(ij)P(ab)\sum_{kc} \langle kb||cj\rangle t_{ik}^{ac} \\
& + P(ij)\sum_c \langle ab||cj\rangle t_i^c - P(ab)\sum_k \langle kb||ij\rangle t_k^a \\
& + \tfrac{1}{2} P(ij)P(ab)\sum_{klcd} \langle kl||cd\rangle t_{ik}^{ac} t_{lj}^{db} + \tfrac{1}{4}\sum_{klcd} \langle kl||cd\rangle t_{ij}^{cd} t_{kl}^{ab} \\
& - \tfrac{1}{2} P(ab)\sum_{klcd} \langle kl||cd\rangle t_{ij}^{ac} t_{kl}^{bd} - \tfrac{1}{2} P(ij)\sum_{klcd} \langle kl||cd\rangle t_{ik}^{ab} t_{jl}^{cd} \\
& + \tfrac{1}{2} P(ab)\sum_{kl} \langle kl||ij\rangle t_k^a t_l^b + \tfrac{1}{2} P(ij)\sum_{cd} \langle ab||cd\rangle t_i^c t_j^d \\
& - P(ij)P(ab)\sum_{kc} \langle kb||ic\rangle t_k^a t_j^c + P(ab)\sum_{kc} f_{kc} t_k^a t_{ij}^{ab} + P(ij)\sum_{kc} f_{kc} t_i^c t_{jk}^{ab} \\
& - P(ij)\sum_{klc} \langle kl||ci\rangle t_k^c t_{lj}^{ab} + P(ab)\sum_{kcd} \langle ka||cd\rangle t_k^c t_{ij}^{db} \\
& + P(ij)P(ab)\sum_{kcd} \langle ak||dc\rangle t_i^d t_{jk}^{bc} + P(ij)P(ab)\sum_{klc} \langle kl||ic\rangle t_l^a t_{jk}^{bc} \\
& + \tfrac{1}{2} P(ij)\sum_{klc} \langle kl||cj\rangle t_i^c t_{kl}^{ab} - \tfrac{1}{2} P(ab)\sum_{kcd} \langle kb||cd\rangle t_k^a t_{ij}^{cd} \\
& - \tfrac{1}{2} P(ij)P(ab)\sum_{kcd} \langle kb||cd\rangle t_i^c t_k^a t_j^d + \tfrac{1}{2} P(ij)P(ab)\sum_{klc} \langle kl||cj\rangle t_i^c t_k^a t_l^b \\
& - P(ij)\sum_{klcd} \langle kl||cd\rangle t_k^c t_i^d t_{lj}^{ab} - P(ab)\sum_{klcd} \langle kl||cd\rangle t_k^c t_l^a t_{ij}^{db}
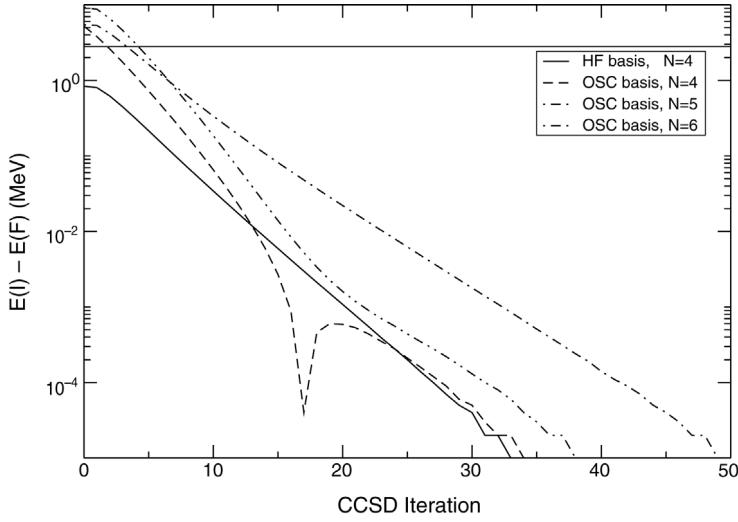\end{aligned}
$$

Fig. 26. The convergence of the ground-state energy as a function of the CCSD iterations in the ^{16}O system for various shell-model spaces.

$$+ \tfrac{1}{4} P(ij) \sum_{klcd} \langle kl||cd \rangle t_i^c t_j^d t_{kl}^{ab} + \tfrac{1}{4} P(ab) \sum_{klcd} \langle kl||cd \rangle t_k^a t_l^b t_{ij}^{cd}$$

$$+ P(ij) P(ab) \sum_{klcd} \langle kl||cd \rangle t_i^c t_l^b t_{kj}^{ad} + \tfrac{1}{4} P(ij) P(ab) \sum_{klcd} \langle kl||cd \rangle t_i^c t_k^a t_j^d t_l^b. \qquad (191)$$

The permutation operator P yields

$$P(ij)f(ij) = f(ij) - f(ji). \qquad (192)$$

The equations of the t_2 amplitudes are non-linear in both T_1 and T_2 terms. While these equations appear quite lengthy, they are solvable through iterative techniques that we will discuss below. We note that the amplitude equations include terms that allow for 4p–4h excitations. Indeed, while we speak of doubles in terms of amplitudes, the class of diagrams involved in the theory include fourth-order terms. This is a very important difference and distinction between the shell model with up to 2p–2h excitations and CCSD. Furthermore, when the energy is computed in CCSD, all terms are linked and connected. For further details, see [71].

Shown in Fig. 26 is the difference between the energy $E(I)$ at a given iteration I and the final energy E_F as a function of iteration number for a calculation of ^{16}O in different oscillator spaces. Here we achieve convergence at the 10^{-5} level by 50 iterations in a model space that includes seven major oscillator shells.

Eq. (189) represent the terms that one uses to compute the energy in second-order perturbation theory of the Møller–Plesset type [23]. Shown in Table 10 are the energies obtained from the 0th $E(0)$ iteration and the final iteration $E(F)$ as functions of increasing oscillator levels in the ^{16}O system. The difference between the converged CCSD energies

Table 10

Comparisons of the 0th order energy $E(0)$ and the converged CCSD results $E(F)$ for ^{16}O as a function of increasing model space. The results are also compared with many-body perturbation theory to second and third order, $E_{\text{MBPT}}^{\text{2nd}}$ and $E_{\text{MBPT}}^{\text{3rd}}$, respectively. All energies are in MeV

$N(\hbar\omega)$	$E(0)$	$E_{\text{MBPT}}^{\text{2nd}}$	$E_{\text{MBPT}}^{\text{3rd}}$	$E(F)$
4 14	−135.12	−132.06	−129.92	−140.47
5 14	−124.79	−124.84	−121.52	−127.79
6 14	−121.36	−121.48	−118.23	−119.73

and the initial 0th order energies increases as the basis space increases. The converged summation of the CCSD equations yields approximately 10 MeV (or 0.6 MeV per particle) in extra binding at the $\hbar\omega$ minima. These findings are corroborated by those from many-body perturbation theory. It is therefore worth comparing these results with those from second-order and third-order many-body perturbation theory as well. These are labeled $E_{\text{MBPT}}^{\text{2nd}}$ and $E_{\text{MBPT}}^{\text{3rd}}$ in the same table. The reader should notice that the 0th iterations of the coupled-cluster schemes already includes corrections to the one-body amplitudes t_1. However, the energy denominators used in the computation of the second-order diagrams of Fig. 2 (diagrams 2 and 3) have hole states determined by

$$\varepsilon_i = \left\langle i \left| \frac{p^2}{2m} \right| i \right\rangle + \sum_{j \leq F} \left\langle ij|G(\omega = \varepsilon_i + \varepsilon_j)|ij \right\rangle, \tag{193}$$

where F stands for the Fermi energy. We do not perform a self-consistent Brueckner–Hartree–Fock calculation however, as done by e.g., Gad and Müther [142]. The agreement with the 0th-order iteration and second-order perturbation theory is very good, especially for five and six major shells, as can be seen from Table 10. However, for third-order perturbation theory one clearly sees fairly large differences compared with the coupled-cluster results. Typically, the relation between first- and second-order in perturbation theory for ^{16}O is given by a factor of ~ 5–6. For e.g., $N = 5$ and $\hbar\omega = 14$ MeV, we have −329.12 MeV from first order and −47.72 from second order. To third order we obtain a repulsive contribution of 3.32 MeV, to be contrasted with the almost 3 MeV of attraction given by higher-order terms in the coupled-cluster expansion. This indicates that many-body perturbation theory to third order is most likely not a converged result. An interesting feature to be noted from many-body perturbation theory calculations is that higher terms lose their importance as the size of the system is increased. For ^{4}He the relation between first-order and second-order perturbation theory is given by a factor of ~ 3–4, depending on the value of $\hbar\omega$. Calculations for ^{40}Ca not reported here indicate a relation of ~ 7–9 between first-order and second-order perturbation theory. This is somewhat expected since the G-matrix is smaller for larger systems, although the energy denominators become smaller.

In the initial coupled-cluster study, we performed calculations of the ^{16}O ground state for up to seven major oscillator shells as a function of $\hbar\omega$. Fig. 27 indicates the level of convergence of the energy per particle for $N = 4, 5, 6, 7$ shells. The experimental value resides at 7.98 MeV per particle. This calculation is practically converged. By seven
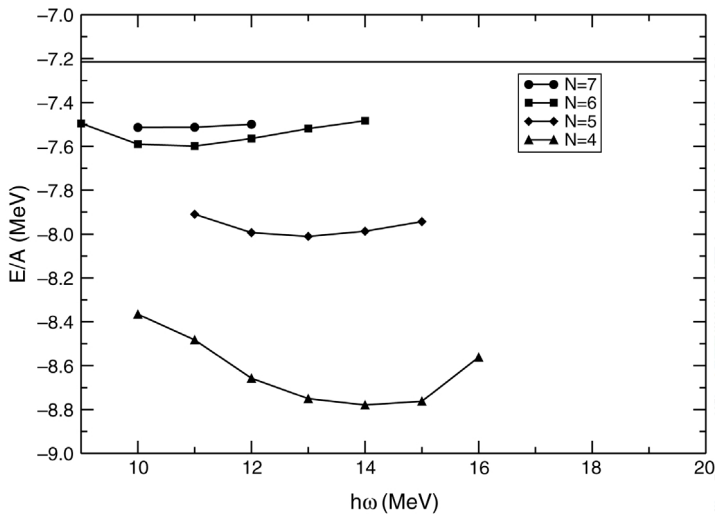
Fig. 27. Dependence of the ground-state energy of ^{16}O on $\hbar\omega$ as a function of increasing model space.

Table 11
The ground-state energy of ^{16}O calculated using various coupled cluster methods and oscillator basis states

Method	Energy
CCSD	-139.310
CR-CCSD(T)	-139.467
SM-SD	-131.887
SM-SDT	-135.489
SM-SDTQ	-138.387

oscillator shells, the $\hbar\omega$ dependence becomes rather minimal and we find a ground-state binding energy of 7.52 MeV per particle in oxygen using the Idaho-A potential. Since the Coulomb interaction should give approximately 0.7 MeV/A of repulsion, and is not included in this calculation, we actually obtain approximately 6.90 MeV of nuclear binding in the 7 major shell calculation which is somewhat above the experimental value. We note that the entire procedure (*G*-matrix plus CCSD) tends to approach from below converged solutions.

We also considered chemistry inspired non-iterative triples corrections to the ground-state energy. We performed this study in the model space consisting of four major oscillator shells. Table 11 shows the total ground-state energy values obtained with the CCSD and one of the triples-correction approaches (labeled CR-CCSD(T) [127, 128, 135, 137] in the table). Slightly differing triples corrections yield similar corrections to the CCSD energy. The coupled-cluster methods recover the bulk of the correlation effects, producing the results of the SM-SDTQ, or better, quality. SM-SDTQ stands for the expensive shell-model (SM) diagonalization in a huge space spanned by the reference and all singly (S), doubly (D), triply (T), and quadruply (Q) excited determinants. To understand

Table 12
The excitation energies of ^{4}He calculated using the oscillator basis states (in MeV)

State	EOMCCSD	CR-CCSD(T)	CISD	Exact
$J = 1$	11.791	12.044	17.515	11.465
$J = 0$	21.203	21.489	24.969	21.569
$J = 2$	22.435	22.650	24.966	22.697

this result, we note that the CCSD T_1 and T_2 amplitudes are similar in order of magnitude. (For an oscillator basis, both T_1 and T_2 contribute to the first-order MBPT wave function.) Thus, the $T_1 T_2$ *disconnected* triples are large, much larger than the T_3 *connected* triples, and the difference between the SM-SDT (SM singles, doubles, and triples) and SM-SD energies is mostly due to $T_1 T_2$. The small T_3 effects, as estimated by CR-CCSD(T), are consistent with the SM diagonalization calculations. If the T_3 corrections were large, we would observe a significant lowering of the CCSD energy, far below the SM-SDTQ result. Moreover, the CCSD and CR-CCSD(T) methods bring the non-negligible higher-than-quadruple excitations, such as $T_1^3 T_2$, $T_1 T_2^2$, and T_2^3, which are not present in SM-SDTQ. It is, therefore, quite likely that the CR-CCSD(T) results are very close to the results of the exact diagonalization, which cannot be performed.

These results indicate that the bulk of the correlation energy within a nucleus can be obtained by solving the CCSD equations. This gives us confidence that we should pursue this method in opened shell systems and to excited states. We have recently [133] performed excited-state calculations on ^{4}He using the EOMCCSD (equation of motion CCSD) method (see Table 12). For the excited states $|\Psi_K\rangle$ and energies $E_K^{\text{(CCSD)}}$ ($K > 0$), we apply the EOMCCSD ("equation of motion CCSD") approximation [131, 132] (equivalent to the response CCSD method [136]), in which

$$|\Psi_K\rangle = R_K^{\text{(CCSD)}} \exp(T^{\text{(CCSD)}})|\Phi\rangle. \tag{194}$$

Here $R_K^{\text{(CCSD)}} = R_0 + R_1 + R_2$ is a sum of the reference (R_0), one-body (R_1), and two-body (R_2) components obtained by diagonalizing $\bar{H}^{\text{(CCSD)}}$ in the same space of singly and doubly-excited determinants $|\Phi_i^a\rangle$ and $|\Phi_{ij}^{ab}\rangle$ as used in the ground-state CCSD calculations. These calculations may also be corrected in a non-iterative fashion using the completely renormalized theory for excited states [127, 128, 134, 135, 137]. The low-lying $J = 1$ state most likely results from the center-of-mass contamination which we have removed only from the ground state. The $J = 0$ and $J = 2$ states calculated using EOMCCSD and CR-CCSD(T) are in excellent agreement with the exact results.

Our experience thus far with the quantum chemistry inspired coupled-cluster approximations to calculate the ground and excited states of the ^{4}He and ^{16}O nuclei indicates that this will be a promising method for nuclear physics. By comparing coupled cluster results with the exact results obtained by diagonalizing the Hamiltonian in the same model space, we demonstrated that relatively inexpensive coupled-cluster approximations recover the bulk of the nucleon correlation effects in ground- and excited-state nuclei. These results are a strong motivation to further develop coupled-cluster methods for the

nuclear many-body problem, so that accurate ab initio calculations for small- and medium-size nuclei become as routine as in molecular electronic structure calculations.

7. Three-body forces in shell-model studies

An important feature of large scale shell-model calculations is that they allow one to probe the underlying many-body physics in a hitherto unprecedented way. As we have seen, the crucial starting point in all such shell-model calculations is the derivation of an effective interaction, be it either an approach based on a microscopic theory starting from the free NN interaction or a more phenomenologically determined interaction. In shell-model studies of e.g., the Sn isotopes, one may have up to 31 valence particles or holes interacting via e.g., an effective two-body interaction. The results of such calculations can therefore yield, when compared with the available body of experimental data, critical inputs to the underlying theory of the effective interaction. Thus, by going to the tin isotopes, in which the major neutron shell between neutron numbers 50 and 82 is being filled beyond the ^{100}Sn closed shell core, we have the opportunity of testing the potential of large-scale shell-model calculations as well as the reliability of realistic effective interactions in systems with many valence particles. It should be noted that in many current shell-model calculations the effective interaction is frequently either parametrized or adjusted in order to optimize the fit to the data. As a matter of principle we shall refrain from making any such adjustments and stick to the interaction obtained by a rigorous calculation consistent with the many-body scheme chosen. Only then may one be able to assess the quality and reliability of the interaction obtained and the possible needs for improvement. It is our firm belief that one of the important aims behind many-body based derivations of effective interactions for the shell model is namely to provide a link between e.g., the free nucleon–nucleon interaction and properties of finite nuclei. Recalling our discussion in Section 1, there are indications that three-body interactions, both real and effective ones, may be of importance. The Green's function Monte Carlo calculations of the Argonne–Urbana group [10–12] and the recent no-core shell-model calculations [74, 138] clearly indicate the need for three-body forces. Similar arguments, based on an analysis of 0p, 1s0d and 1p0f nuclei by Zuker [139] lend support to this picture for heavier nuclei as well. Real three-body forces are necessary in order to reproduce the saturation properties of nuclear matter as well, see for example [46].

Thus, with many valence nucleons present, such large-scale shell-model calculations may tell us how well e.g., an effective interaction which only includes two-body terms does in reproducing properties such as excitation spectra and binding energies.

In general, excitation spectra for the chain of both odd and even isotopes from ^{116}Sn to ^{130}Sn exhibit an excellent agreement with the data, see for example our discussion in Section 4. All these results are based on shell-model calculations starting with a two-body effective interaction determined from the recent charge dependent NN potentials of Machleidt and co-workers [64, 65]. These NN interactions were renormalized for the given nuclear medium, using for example ^{132}Sn as closed shell core, through the introduction of the so-called reaction matrix G, which corresponds to solving the Lippmann–Schwinger equation for a finite nucleus. The G-matrix formed then the basis for a perturbative

Table 13
Binding energies for Sn isotopes

	^{130}Sn	^{129}Sn	^{128}Sn	^{126}Sn	^{124}Sn	^{122}Sn	^{116}Sn
Exp	−2.09	−1.70	−3.64	−4.79	−5.47	−5.64	−2.61
$V^{(2)}$	−2.24	−2.63	−4.60	−6.99	−9.39	−11.77	−18.58
Mod. Shell Model	−2.09	−2.78	−3.72	−4.81	−5.32	−5.22	−1.12
$+V^{(3)}$		+0.009	+0.029	+0.096	+0.213	+0.394	+0.998
Trp. contr.		+0.009	+0.034	+0.170	+0.504	+1.08	+4.760

calculation of more complicated Feynman–Goldstone diagrams. However, if one studies Table 13, one sees that the binding energy relative to ^{131}Sn is clearly askance with the data. The binding energy is defined as

$$\text{BE}[^{132-n}\text{Sn}] = \text{BE}[^{132-n}\text{Sn}] - \text{BE}[^{132}\text{Sn}] - n(\text{BE}[^{131}\text{Sn}] - \text{BE}[^{132}\text{Sn}]). \quad (195)$$

Experiment indicates a minimum around ^{124}Sn–^{122}Sn and consequently a shell closure around ^{116}Sn whereas theoretical binding energies increase linearly all the way down to ^{116}Sn.

The above is just an example of one of the problems which beset the theory of effective interactions for the shell model. In this case, as also pointed out by Zuker and co-workers [139], one is not able to obtain simultaneously a good reproduction of both the excitation spectra and the binding energy. Similar problems have also been discussed in connection with large scale shell-model calculations of 1f0p shell nuclei. To give an example, effective interactions derived from two-body NN interactions which fit nucleon–nucleon scattering data, are not able to reproduce the well-known shell closure in ^{48}Ca or the excitation spectra of ^{47}Ca and ^{49}Ca, see the discussion in [5, 16, 139].

In this work we wish to address the discrepancy between theory and experiment shown in Table 13 by including effective three-body forces in our shell-model calculations. The reason for this follows from the observation that the introduction of a global monopole correction of the form $Wn(n-1)/2$, with n being the number of valence particles and W a quantity which is related to the energy centroids, can, when added to our theoretical binding energy, partly cure the discrepancy seen in Table 13. Three-body forces typically yield repulsive corrections which scale as $n(n-1)$. In Table 13 we adjusted the term W by simply requiring it to equal the difference in binding energy between the calculated and experimental values for ^{130}Sn. This resulted in $W = 0.15$ MeV. Adding such a global correction to even nuclei shown in Table 13 results in the column labeled Mod. shell model. Clearly this improves the theoretical results in the correct direction and such a global modification of the matrix elements has no effect on the excitation spectra.

These observations form thus the starting point for our investigation of three-body effective interactions. More explicitly, we aim at seeing whether three-body interactions may yield a more microscopic understanding of the above problem. The results presented employ effective three-body diagrams to second order in the G-matrix (see Polls et al. [141] for details) and have been shown at various conferences [140]. Examples of three-body diagrams are shown in Fig. 28. Diagram (a) is a third-order contribution not included
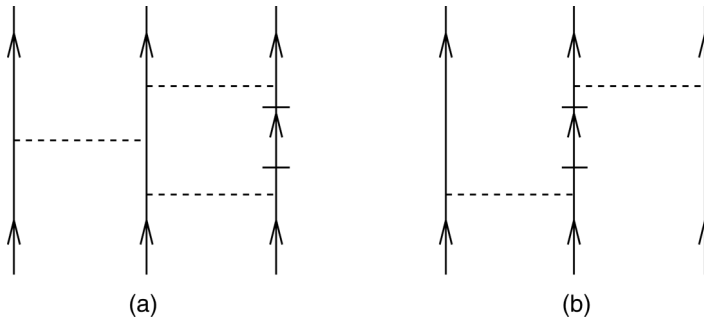
Fig. 28. Examples of unfolded three-body diagrams.

in the $\hat{Q}$-box. Diagram (b) is included. The inclusion of such effective three-body diagrams do add a needed repulsion as seen from the column labeled $V^{(3)}$ in Table 13. However there is still a large discrepancy between theory and experiment for the binding energy and even multiplying the number of triplets

$$\text{number of triplets} = \frac{n!}{3!(n-3)!}$$

with the three-body contribution from ^{129}Sn yields too little attraction. Most likely the lack of repulsion can be ascribed to real three-body forces. Effective three-body forces for identical particles tend to be small due to the absence of the strong tensor channels in the intermediate states. This is also in line with recent works on the energy of pure neutron drops, where three-body clusters are included [9]. The reader should however note that our inclusion of three-body effective diagrams is incomplete. The summation of folded diagrams is based on only a two-body and three-body $\hat{Q}$-box. We have not included a one-body $\hat{Q}$-box. The latter introduces unlinked diagrams which need to be subtracted correctly when summing folded diagrams. To investigate whether the discrepancies seen for the binding energies are due to real three-body forces or not, we plan to include these in future studies, together with a three-body G-matrix and properly determined $\hat{Q}$-box and folded diagrams. One needs thus to carefully distinguish between three-body forces and effective three-body interactions.

8. Perspectives

The study of exotic nuclei opens new challenges to nuclear physics. The challenges and the excitement arise because exotic nuclei will present new and radically different manifestations of nucleonic matter that occur near the bounds of nuclear existence, where the special features of weakly bound, quantal systems come into prominence. Furthermore, many of these nuclei are key to understanding matter production in the universe. Given that present and future nuclear structure research facilities will open significant territory into regions of medium-mass and heavier nuclei, it becomes important to investigate theoretical methods that will allow for a description of medium-mass nuclear systems. Such systems

pose significant challenges to existing nuclear structure models, especially since many of these nuclei will be unstable and short-lived. How to deal with weakly bound systems and coupling to resonant states is an unsettled problem in nuclear spectroscopy.

The aim of this work has been to expose both the weakness and strength of three many-body methods for studying nuclei heavier than ^{16}O. For lighter nuclei, both Green's function Monte Carlo [8, 10–12] and no-core shell-model calculations [1–3, 74, 138] offer true benchmarks for nuclear structure studies. The nuclear shell-model, combined with microscopically or phenomenologically derived effective interactions, has been extremely successful in reproducing properties of nuclei employing $0\hbar\omega$ model spaces such as the 1s0d [5], the 1p0f shell [6, 83] and, as discussed in this work, medium heavy systems in the region of $A = 100$ to $A = 132$. However, if one wishes to study weakly bound systems or resonant states within this framework, the dimensionality of the problem soon exceeds present and most likely future hardware capabilities.

For the heavier systems which are expected to be studied with facilities like RIA, many-body methods like the coupled cluster or parquet diagrams offer possibilities for extending microscopic ab initio calculations to nuclei like ^{40}Ca. Especially the coupled-cluster methods are very promising, since they allow one to study ground- and excited-state properties of nuclei with dimensionalities beyond the capability of present shell-model approaches. As demonstrated in [133] we show for the first time how to calculate excited states for a nucleus using coupled-cluster methods from quantum chemistry. For the weakly bound nuclei to be produced by future low-energy nuclear structure facilities it is almost imperative to increase the degrees of freedom under study in order to reproduce basic properties of these systems. We are presently working on deriving effective interactions for weakly bound systems to be used in coupled-cluster studies of these weakly bound nuclei. An extension of this project is to extract effective two-body interactions for open-shell systems. These will in turn be used in shell calculations.

We have based most of our analysis on effective interactions using two-body nucleon–nucleon interactions only. We feel this is important since techniques like the coupled-cluster methods or parquet diagrams allow one to include a much larger class of many-body terms than done earlier. Eventual discrepancies with experiment such as the missing reproduction of e.g., the first excited 2^+ state in a 1p0f calculation of ^{48}Ca, can then be ascribed to eventual missing three-body forces, as indicated by the studies in [10–12, 46, 74, 138] for light nuclei. The inclusion of real three-body interactions belongs to our future plans both for effective interactions for nuclei with $A \sim 100$ and larger as well as within the coupled-cluster method and parquet diagrams for nuclei like ^{40}Ca.

Acknowledgements

References

[1] P. Navrátil, B.R. Barrett, Phys. Rev. C 57 (1998) 562.
[2] P. Navrátil, J.P. Vary, B.R. Barrett, Phys. Rev. Lett. 84 (2000) 5728.
[3] P. Navrátil, J.P. Vary, B.R. Barrett, Phys. Rev. C 62 (2000) 054311.
[4] D.C. Zheng, B.R. Barrett, L. Jaqua, J.P. Vary, R.J. McCarthy, Phys. Rev. C 48 (1993) 1083.
[5] B.A. Brown, Prog. Part. Nucl. Part. 47 (2001) 517, and references therein.
[6] T. Otsuka, M. Homna, T. Mizusaki, N. Shimizu, Y. Utsuno, Prog. Part. Nucl. Part. 47 (2001) 319, and references therein.
[7] S.E. Koonin, D.J. Dean, K. Langanke, Phys. Rep. 278 (1997) 1.
[8] B.S. Pudliner, V.R. Pandharipande, J. Carlson, S.C. Pieper, R.B. Wiringa, Phys. Rev. C 56 (1997) 1720.
[9] B.S. Pudliner, A. Smerzi, J. Carlson, V.R. Pandharipande, S.C. Pieper, D.G. Ravenhall, Phys. Rev. Lett. 76 (1996) 2416.
[10] S.C. Pieper, V.R. Pandharipande, R.B. Wiringa, J. Carlson, Phys. Rev. C 64 (2001) 014001.
[11] S.C. Pieper, K. Varga, R.B. Wiringa, Phys. Rev. C 66 (2002) 0044310.
[12] R.B. Wiringa, S.C. Pieper, Phys. Rev. Lett. 89 (2002) 182501.
[13] K. Suzuki, R. Okamoto, H. Kumagai, Nuclear Phys. A 580 (1994) 213;
K. Suzuki, R. Okamoto, Progr. Theoret. Phys. 92 (1994) 1045; Progr. Theoret. Phys. 93 (1995) 905.
[14] B.H. Brandow, Rev. Modern Phys. 39 (1967) 771.
[15] T.T.S. Kuo, E. Osnes, Folded-Diagram Theory of the Effective Interaction in Atomic Nuclei, Springer Lecture Notes in Physics, vol. 364, Springer, Berlin, 1990;
T.T.S. Kuo, in: T.T.S. Kuo, S.S.M. Wong (Eds.), Topics in Nuclear Physics, Lecture Notes in Physics, vol. 144, Springer, Berlin, 1981, p. 248.
[16] M. Hjorth-Jensen, T.T.S. Kuo, E. Osnes, Phys. Rep. 261 (1995) 125.
[17] I. Lindgren, J. Morrison, Atomic Many-Body Theory, Springer, Berlin, 1985;
I. Lindgren, J. Phys. B: At. Mol. Opt. Phys. 24 (1991) 1143.
[18] K. Suzuki, Progr. Theoret. Phys. 68 (1982) 1627;
K. Suzuki, R. Okamoto, Progr. Theoret. Phys. 75 (1986) 1388; Progr. Theoret. Phys. 76 (1986) 127.
[19] F. Coester, Nuclear Phys. 7 (1958) 421.
[20] F. Coester, H. Kümmel, Nuclear Phys. 17 (1960) 477.
[21] R.J. Bartlett, Ann. Rev. Phys. Chem. 32 (1981) 359.
[22] T.D. Crawford, H.F. Schaefer III, Rev. Comp. Chem. 14 (2000) 33.
[23] C. Møller, M. Plesset, Phys. Rev. 46 (1934) 618.
[24] F.E. Harris, H.J. Monkhorst, D.L. Freeman, Algebraic and Diagrammatic Methods in Many-Fermion Theory, Oxford, New York, 1992.
[25] P. Piecuch, P.-D. Fan, K. Jedziniak, K. Kowalski, Phys. Rev. Lett. 90 (2003) 113001.
[26] T. Helgaker, P. Jørgensen, J. Olsen, Molecular Electronic Structure Theory. Energy and Wave Functions, Wiley, Chichester, 2000.
[27] J. Arponen, Phys. Rev. A 55 (1997) 2686.
[28] H. Kümmel, K.H. Lührmann, Nuclear Phys. A 191 (1972) 525.
[29] H. Kümmel, K.H. Lührmann, Nuclear Phys. A 194 (1972) 225.
[30] J.G. Zabolitzky, Nuclear Phys. A 228 (1974) 285.
[31] H. Kümmel, K.H. Lührmann, J.G. Zabolitzky, Phys. Rep. 36 (1977) 1.
[32] R.F. Bishop, E. Buendia, M.F. Flynn, R. Guardiola, J. Phys. G: Nucl. Part. Phys. 17 (1991) 857; J. Phys. G: Nucl. Part. Phys. 18 (1992) 1157; J. Phys. G: Nucl. Part. Phys. 19 (1993) 1663;
R. Guardiola, P.I. Moliner, J. Navarro, R.F. Bishop, A. Puente, N.R. Walet, Nuclear Phys. A 609 (1996) 218.
[33] B. Mihaila, J.H. Heisenberg, Phys. Rev. Lett. 84 (2000) 1403.
[34] B. Mihaila, J.H. Heisenberg, Phys. Rev. C 61 (2000) 054309.
[35] B. Mihaila, J.H. Heisenberg, Phys. Rev. C 60 (1999) 054303.

[36] J.H. Heisenberg, B. Mihaila, Phys. Rev. C 59 (1999) 1440.

[37] C. de Dominicis, P.C. Martin, J. Math. Phys. 5 (1964) 14.

[38] B. Roulet, F. Gavoret, P. Nozieres, Phys. Rev. 178 (1969) 1072.

[39] S. Babu, G.E. Brown, Ann. Phys. 78 (1973) 1.

[40] A.D. Jackson, A. Lande, R.A. Smith, Phys. Rep. 86 (1982) 55;
A. Lande, R.A. Smith, Phys. Rev. A 45 (1992) 913, and references therein.

[41] J.P. Blaizot, G. Ripka, Quantum Theory of Finite Systems, MIT Press, Cambridge, USA, 1986 (Chapter 15).

[42] N.E. Bickers, D.J. Scalapino, Ann. Phys. 193 (1989) 206;
N.E. Bickers, S.R. White, Phys. Rev. B 43 (1991) 8044;
N.E. Bickers, D.J. Scalapino, Phys. Rev. B 46 (1992) 8050.

[43] J. Yeo, M.A. Moore, Phys. Rev. B 54 (1996) 4218.

[44] A.T. Zheleznyak, V.M. Yakovenko, I.E. Dzyaloshinskii, Phys. Rev. B 55 (1997) 3200.

[45] A. Fabrocini, F. Arias de Savedra, G. Có, P. Folgarait, Phys. Rev. C 57 (1998) 1668.

[46] A. Akmal, V.R. Pandharipande, D.G. Ravenhall, Phys. Rev. C 58 (1998) 1804.

[47] M.W. Kirson, Ann. Phys. 66 (1971) 624; Ann. Phys. 68 (1971) 556; Ann. Phys. 82 (1974) 345.

[48] P.J. Ellis, E. Osnes, Rev. Modern Phys. 49 (1977) 777.

[49] A. Ramos, Ph.D. Thesis, University of Barcelona, 1988 (unpublished).

[50] A. Ramos, A. Polls, W.H. Dickhoff, Nuclear Phys. A 503 (1989) 1.

[51] S.D. Yang, J. Heyer, T.T.S. Kuo, Nuclear Phys. A 448 (1986) 420.

[52] H.Q. Song, S.D. Yang, T.T.S. Kuo, Nuclear Phys. A 462 (1987) 491.

[53] H.A. Mavromatis, H. Müther, T. Taigel, T.T.S. Kuo, Nuclear Phys. A 470 (1987) 185.

[54] H.A. Mavromatis, P.J. Ellis, H. Müther, Nuclear Phys. A 530 (1991) 251.

[55] E. Heinz, H. Müther, H.A. Mavromatis, Nuclear Phys. A 587 (1995) 77.

[56] W.H. Dickhoff, C. Barbieri, Prog. Part. Nucl. Phys. 52 (2004) 377–496, nucl-th/0402034 (preprint).

[57] H. Müther, A. Polls, Prog. Part. Nucl. Phys. 45 (2000) 243.

[58] T.T.S. Kuo, J. Shurpin, K.C. Tam, E. Osnes, P.J. Ellis, Ann. Phys. 132 (1981) 237.

[59] H.A. Bethe, B.H. Brandow, A.G. Petschek, Phys. Rev. 129 (1963) 225.

[60] E.M. Krenciglowa, C.L. Kung, T.T.S. Kuo, E. Osnes, Ann. Phys. 101 (1976) 154.

[61] S.Y. Lee, K. Suzuki, Phys. Lett. B 91 (1980) 79;
K. Suzuki, S.Y. Lee, Progr. Theoret. Phys. 64 (1980) 2091.

[62] J. Des Cloizeaux, Nuclear Phys. 20 (1960) 321.

[63] T.T.S. Kuo, P.J. Ellis, J. Hao, Z. Li, K. Suzuki, R. Okamoto, H. Kumagai, Nuclear Phys. A 560 (1993);
P. Navrátil, H.B. Geyer, T.T.S. Kuo, Phys. Lett. B 315 (1993) 1.

[64] R. Machleidt, F. Sammarruca, Y. Song, Phys. Rev. C 53 (1996) R1483.

[65] R. Machleidt, Phys. Rev. C 63 (2001) 024001.

[66] D.R. Entem, R. Machleidt, Phys. Lett. B 524 (2002) 93.

[67] R.R. Whitehead, A. Watt, B.J. Cole, I. Morrison, Adv. Nucl. Phys. 9 (1977) 123.

[68] R.D. Lawson, Theory of the Nuclear Shell Model, Clarendon Press, Oxford, 1980.

[69] D.J. Dean, M.T. Ressell, M. Hjorth-Jensen, S.E. Koonin, K. Langanke, A.P. Zuker, Phys. Rev. C 59 (1999) 2474.

[70] T. Papenbrock, A. Juodagalvis, D.J. Dean, Phys. Rev. C 69 (2004) 024312.

[71] D.J. Dean, M. Hjorth-Jensen, Phys. Rev. C 69 (2004) (in press), nucl-th/0308088 (preprint).

[72] D.J. Dean, M. Hjorth-Jensen, in preparation.

[73] J. Olsen, P. Jørgensen, J. Simons, Chem. Phys. Lett. 169 (1990) 463.

[74] P. Navrátil, W.E. Ormand, Phys. Rev. Lett. 88 (2002) 152502.

[75] M. Horoi, J. Kaiser, V. Zelevinsky, Phys. Rev. C 67 (2003) 054309.

[76] M. Horoi, B.A. Brown, V. Zelevinsky, Phys. Rev. C 67 (2003) 034303.

[77] A. Juodagalvis, ORNL parallel shell-model code, 2003 (unpublished).

[78] T. Engeland, Oslo shell-model code, 1990–2004 (unpublished).

[79] P. Navrátil, E. Caurier, Phys. Rev. C 69 (2004) 014311.

[80] E. Caurier, P. Navrátil, W.E. Ormand, J.P. Vary, Phys. Rev. C 66 (2002) 024314.

[81] E. Caurier, P. Navrátil, W.E. Ormand, J.P. Vary, Phys. Rev. C 64 (2001) 051301.

[82] E. Caurier, G. Martinez-Pinedo, F. Nowacki, A. Poves, J. Retamosa, A.P. Zuker, Phys. Rev. C 59 (1999) 2033.

[83] E. Caurier, A.P. Zuker, A. Poves, G. Martinez-Pinedo, Phys. Rev. C 50 (1994) 224.
[84] M. Homna, T. Mizusaki, T. Otsuka, Phys. Rev. Lett. 75 (1995) 1284.
[85] M. Homna, T. Mizusaki, T. Otsuka, Phys. Rev. Lett. 77 (1996) 3315.
[86] I. Talmi, Simple Models of Complex Nuclei, Harwood Academic Publishers, Chur, 1993.
[87] E.R. Davidson, Comput. Phys. Commun. 53 (1989) 49;
     E.R. Davidson, Comput. Phys. 5 (1993) 519.
[88] A. Holt, T. Engeland, M. Hjorth-Jensen, E. Osnes, Phys. Rev. C 61 (2000) 064318.
[89] G. Leander et al., Phys. Rev. C 30 (1984) 416.
[90] J. Duflo, A.P. Zuker, Phys. Rev. C 59 (1999) R2347.
[91] H. Grawe et al., in: Proc. 6th Int. Seminar Highlights of Modern Nuclear Structure, World Scientific, Singapore, 1999, p. 137.
[92] M. Lipoglavšek et al., Phys. Rev. C 65 (2002) 021302.
[93] M. Vencelj, to be published.
[94] D. Alber et al., Z. Phys. A 332 (1989) 129.
[95] C. Fahlander et al., Phys. Rev. C 63 (2001) 021307.
[96] A.R. Poletti et al., Phys. Rev. C 10 (1974) 2312.
[97] N. Bendjaballah et al., Nuclear Phys. A 280 (1977) 228.
[98] A. Holt, T. Engeland, M. Hjorth-Jensen, E. Osnes, Nuclear Phys. A 634 (1998) 41.
[99] H. Gausemel, B. Fogelberg, T. Engeland, P. Hoff, M. Hjorth-Jensen, H. Mach, K.A. Mezilev, J.P. Omtvedt, Phys. Rev. C 69 (2004) (in press).
[100] P. Hoff et al., Phys. Rev. Lett. 77 (1996) 1020.
[101] M. Kartamyshev, T. Engeland, M. Hjorth-Jensen, E. Osnes, unpublished.
[102] I.Y. Lee, Nuclear Phys. A 520 (1990) 641c.
[103] D.G. Sarantites et al., Nucl. Instrum. Methods A381 (1996) 418.
[104] T. Motobayashi et al., Phys. Lett. B 346 (1995) 9.
[105] H. Scheit et al., Phys. Rev. Lett. 77 (1996) 3967.
[106] T. Glasmacher et al., Phys. Lett. B 395 (1997) 163.
[107] T.R. Werner et al., Nuclear Phys. A 597 (1996) 327.
[108] X. Campi, H. Flocard, A.K. Kerman, S.E. Koonin, Nuclear Phys. A 251 (1975) 193.
[109] E.K. Warburton, J.A. Becker, B.A. Brown, Phys. Rev. C 41 (1990) 1147.
[110] A. Poves, J. Retamosa, Nuclear Phys. A 571 (1994) 221.
[111] N. Fukunishi, T. Otsuka, T. Sebe, Phys. Lett. B 296 (1992) 279.
[112] J. Retamosa, E. Caurier, F. Nowacki, A. Poves, Phys. Rev. C 55 (1997) 1266.
[113] E. Caurier, F. Nowacki, A. Poves, J. Retamosa, Phys. Rev. C 58 (1998) 2033.
[114] S.E. Koonin, D.J. Dean, K. Langanke, Ann. Rev. Nucl. Part. Sci. 47 (1997) 463.
[115] G.H. Lang, C.W. Johnson, S.E. Koonin, W.E. Ormand, Phys. Rev. C 48 (1993) 1518.
[116] P.M. Endt, Nuclear Phys. A 521 (1990) 1.
[117] S. Raman et al., At. Data Nucl. Data Tables 36 (1987) 1.
[118] A. Poves, J. Retamosa, Phys. Lett. B 184 (1987) 311.
[119] C. Mahaux, R. Sartor, Phys. Rep. 211 (1992) 53.
[120] M. Hjorth-Jensen, in preparation.
[121] M.W. Kirson, L. Zamick, Ann. Phys. 60 (1970) 188.
[122] F.L. Goodin, P.J. Ellis, Nuclear Phys. A 334 (1980) 229.
[123] W.H. Dickhoff, H. Müther, Nuclear Phys. A 473 (1987) 394, and references therein.
[124] A.C. Hayes, P. Navrátil, J.P. Vary, Phys. Rev. Lett. 91 (2003) 012502.
[125] R.J. Bartlett, in: D.R. Yarkony (Ed.), Modern Electronic Structure Theory, vol. 1, World Scientific, Singapore, 1995, p. 1047.
[126] J. Paldus, X. Li, Adv. Chem. Phys. 110 (1999) 1.
[127] P. Piecuch, K. Kowalski, I.S.O. Pimienta, M.J. McGuire, Int. Rev. Phys. Chem. 21 (2002) 527.
[128] P. Piecuch, K. Kowalski, P.-D. Fan, I.S.O. Pimienta, in: J. Maruani, R. Lefebvre, E. Brändas (Eds.), Topics in Theoretical Chemical Physics, Series Progress in Theoretical Chemistry and Physics, vol. 12, Kluwer, Dordrecht, 2004, p. 119.
[129] J. Čížek, J. Chem. Phys. 45 (1966) 4256.
[130] J. Čížek, Adv. Chem. Phys. 14 (1969) 35.
[131] J.F. Stanton, R.J. Bartlett, J. Chem. Phys. 98 (1993) 7029.

[132] P. Piecuch, R.J. Bartlett, Adv. Quantum Chem. 34 (1999) 295.
[133] K. Kowalski, D.J. Dean, M. Hjorth-Jensen, T. Papenbrock, P. Piecuch, Phys. Rev. Lett. 92 (2004) 132501.
[134] K. Kowalski, P. Piecuch, J. Chem. Phys. 115 (2001) 2966.
[135] K. Kowalski, P. Piecuch, J. Chem. Phys. 120 (2004) 1715.
[136] H. Monkhorst, Int. J. Quantum Chem. Symp. 11 (1977) 421.
[137] K. Kowalski, P. Piecuch, J. Chem. Phys. 113 (2000) 18.
[138] P. Navrátil, W.E. Ormand, Phys. Rev. C 68 (2003) 034305.
[139] A.P. Zuker, Phys. Rev. Lett. 90 (2003) 042502.
[140] T. Engeland, M. Hjorth-Jensen, unpublished.
[141] A. Polls, H. Müther, A. Faessler, T.T.S. Kuo, E. Osnes, Nuclear Phys. A 401 (1983) 124;
    H. Müther, A. Polls, T.T.S. Kuo, Nuclear Phys. A 435 (1985) 548.
[142] Kh. Gad, H. Müther, Phys. Rev. C 66 (2002) 044301.